

# **The photophysical properties of chromophores assembled into metal-organic framework thin-films**

Zur Erlangung des akademischen Grades einer  
DOKTORIN DER NATURWISSENSCHAFTEN

(Dr. rer. nat.)

von der KIT-Fakultät für Chemie und Biowissenschaften  
des Karlsruher Instituts für Technologie (KIT)  
genehmigte

DISSERTATION

von

M.Sc. Zeinab Mohamed Abdelwahab Hassan

aus

Fayoum- Egypt

Dekan: Prof. Dr. Manfred Wilhelm

Referent: Prof. Dr. Christof Wöll

Korreferent: Prof. Dr. Stefan Bräse

Tag der mündlichen Prüfung: 13.04.2021



This document is licensed under a Creative Commons  
Attribution-ShareAlike 4.0 International License (CC BY-SA 4.0):  
<https://creativecommons.org/licenses/by-sa/4.0/deed.en>

I hereby declare, that this thesis is based on my work and was written by me. I have properly referenced all the text and figures that are not my own.

Zeinab Hassan

## Table of Contents

<b>Abstract:</b> .....	1
<b>Zusammenfassung</b> .....	2
<b>1 Introduction</b> .....	4
<b>1.1 Metal-organic frameworks (MOFs)</b> .....	4
<b>1.2 Surface anchored Metal-Organic Frameworks (SURMOFs)</b> .....	11
1.2.1 Fabrication of SURMOFs.....	12
1.2.2 Techniques for the growth of SURMOFs.....	14
<b>1.3 Photophysical properties of photoresposinve MOFs:</b> .....	20
1.3.1 Synthetic strategies for combine Photoresponsive materials within MOFs:.....	21
1.3.2 Types of photoresponse:.....	22
<b>2 Characterization methods</b> .....	32
<b>2.1 X-Ray Diffraction (XRD)</b> .....	32
2.1.1 Theoretical background.....	32
2.1.2 X-Ray diffractometer.....	33
2.1.3 X-Ray-Out-of-plane and X-Ray-in-plane.....	34
<b>2.2 Infrared Spectroscopy (IR)</b> .....	35
2.2.1 Infrared Reflection Absorption Spectroscopy (IRRAS).....	38
2.2.2 Attenuated Total Reflectance (ATR).....	39
<b>2.3 Ultraviolet-Visible (UV-Vis) spectroscopy</b> .....	39
<b>2.4 Scanning Electron Microscopy</b> .....	41
<b>2.5 Near Edge-X-Ray Absorption Fine Structure (NEXAFS)</b> .....	42
<b>3 Materials and experiments</b> .....	45
<b>3.1 Chemicals</b> .....	45
<b>3.2 Substrates</b> .....	45
<b>3.3 Preparation of the substrates.</b> .....	45
<b>3.4 Functionalization of silicon substrates</b> .....	45
<b>3.5 Functionalization of quartz glass substrates</b> .....	46
<b>3.6 Preparation of SAMs</b> .....	46
3.6.1 Preparation of MHDA SAMs on gold substrate.....	46
3.6.2 Preparation of MUD SAMs on gold substrate.....	46
<b>3.7 Synthesis of Zn-bianthryl-based SURMOF using spin coating</b> .....	46
<b>3.8 Preparation of Zn-bianthryl based SURMOF (pristine)spray method.</b> .....	47
<b>3.9 Preparation of irradiated Zn-bianthryl based SURMOF</b> .....	47

3.10	<b>Preparation of Zn-viologen based SURMOF (pristine)</b> .....	47
3.11	<b>Irradiation of the Zn-viologen based SURMOF</b> .....	48
3.12	<b>Electron paramagnetic resonance (EPR) measurements:</b> .....	48
3.13	<b>Quartz crystal microbalance</b> .....	48
3.14	<b>Electrical conductivity</b> .....	49
3.15	<b>Synthesis of the organic linkers</b> .....	50
3.15.1	(dimethyl-4,4'-(anthracene-9,10-diyl) dibenzoate) ADB-COOCH <sub>3</sub> .....	50
3.15.2	4,4'-(anthracene-9,10-diyl) dibenzoic acid (ADB). .....	51
3.15.3	Dimethyl 4,4'-([9,9'-bianthracene]-10,10'-diyl) dibenzoate (bianthrylCOOCH <sub>3</sub> ). .....	52
3.15.4	- 4,4'-([9,9'-bianthracene]-10,10'-diyl) dibenzoic acid (bianthryl). .....	53
3.15.5	- Dimethyl-4,4'-(anthracene-9,10-diylbis(ethyne-2,1-diyl)) dibenzoate (C-C ADB-CH <sub>3</sub> ) .....	54
3.15.6	4,4'-(Anthracene-9,10-diylbis(ethyne-2,1-diyl)) dibenzoic acid (C-C ADB). .....	55
4	<b>Results:</b> .....	56
4.1	<b>Self-Photosensitized Oxidation of a Bianthryl-Based SURMOF</b> .....	56
4.1.1	Introduction.....	56
4.1.2	The structure of the linkers and the SURMOFs.....	56
4.1.3	Synthesis and characterization Zn-bianthryl based SURMOF .....	57
4.1.4	Photophysical characterization of Zn-bianthryl based SURMOF .....	59
4.1.5	Further characterization of the prolong irradiation product .....	61
4.1.6	Conclusion .....	75
4.2	<b>Viologen-based MOFs Thin Films with Highly Orientation and Photochromic Properties.</b> 76	
4.2.1	Introduction.....	76
4.2.2	The structure of the linkers and the SURMOF. ....	76
4.2.3	Synthesis and characterization of Zn-viologen based SURMOF.....	77
4.2.4	Photochromism .....	81
4.2.5	The photoconductivity of the Zn-viologen-based SURMOF.....	90
4.2.6	Conclusion .....	90
5	<b>Conclusion</b> .....	92
6	<b>Abbreviation</b> .....	93
7	<b>References</b> .....	96
8	<b>Publication</b> .....	1

## Abstract:

Metal-organic frameworks (MOFs) are hybrid porous materials consisting of a metal center connected with an organic linker via coordination bonds. Virtually infinite possibilities of metal-linker combination have resulted in a large number of MOF structures (>100,000) to date, with different structural topologies. The properties of MOFs can be tuned by the rational selection of the metal centers and organic linkers to design specific MOFs to be adequate to the in-demand applications. Regarding more advanced applications, the bulk MOFs synthesized *via* conventional solvothermal method are not always suitable. Heterogeneous morphology, weaker adhesion to substrate, and high defect densities present in the powder MOFs greatly influence the structure property correlation. One approach used to fabricate monolithic, crystalline, and well-controlled thickness is the layer-by-layer (LbL) method via the liquid phase epitaxy technique. So, in the present thesis, I used this technique to build a highly crystalline, monolithic, and orientated surface-anchored metal-organic frameworks (SURMOFs) thin films. One type of organic linkers was used here is called a photoactive compound. The spatial arrangement of these photoactive molecules in the SURMOF leads to materials with distinguished photophysical properties. In the present work, I studied bianthryl chromophoric linker, equipped with metal-coordinating groups, to construct a photoluminescent Zn-bianthryl based surface-anchored MOF (SURMOF) thin film. The Zn-bianthryl SURMOF has a 2D-layer stacked structure and shows cyan luminescence upon excitation with ultraviolet (UV) light. In response to the prolonged UV irradiation under ambient conditions, the Zn-bianthryl based SURMOF exhibited a prominent change in the ground and excited-state optical properties, without losing its crystalline structure. A detailed spectroscopic study using UV-Vis, FTIR, Raman, EPR, and NEXAFS indicated the formation of stable oxidation products of bianthryl (endoperoxide bianthryl) in the SURMOF. The present study identifies the key factors of the bianthryl oxidation process which involve a self-sensitized photochemical pathway. Also, redox-active viologen-based metal-organic frameworks (MOFs) have received an increasing interest in recent years, from the perspective of smart optically active materials. In this respect, a dicarboxylate functionalized viologen, 1,1'-bis (4-(carboxylic acid) phenyl)-[4,4'-bipyridine]-1,1'-dium dichloride (Viologen) is used as a linker to construct a surface-anchored metal-organic framework (SURMOF) thin film using a layer-by-layer liquid-phase epitaxy method. This technique produces a highly crystalline, oriented viologen-based SURMOF-2. The oriented, monolithic, crystalline SURMOF exhibits fast reversible photochromism, compared to

the previously reported viologen-based powder MOFs. The photochromism in the SURMOF is investigated by the UV-Vis, EPR and XPS.

## **Zusammenfassung**

Metallorganische Gerüste (MOFs) sind poröse Hybridmaterialien, die aus einem Metallzentrum bestehen, verbunden über Koordinationsbindungen mit einem organischen Linker. Nahezu unendliche Möglichkeiten der Metall-Linker-Kombination haben bisher zu einer großen Anzahl von MOF-Strukturen (>100.000) mit unterschiedlichen Strukturtopologien geführt. Die Eigenschaften von MOFs können durch eine durchdachte Auswahl der Metallzentren und organischen Linker abgestimmt werden, um MOFs spezifisch für bedarfsgerechte Anwendungen zu entwickeln.

Bezugnehmend auf die weit fortgeschrittenen Anwendungen, ist die Herstellung von Festkörper-MOFs mittels der herkömmlichen Solvothermal-Methode nicht immer zielführend. Heterogene Morphologie, schwächere Anbindung an das Substrat und eine hohe Fehlstellendichte, wie in Festkörper-MOFs vorhanden, beeinflussen stark die Struktur-Eigenschafts Korrelation.

Ein Ansatz zur Herstellung monolithischer kristalliner MOFs mit gut kontrollierter Dicke ist das Schicht-für-Schicht (LbL – layer-by-layer) -Verfahren über die Flüssigphasen-Epitaxie-Technik. In dieser Arbeit habe ich diese Technik verwendet, um hochkristalline, monolithische und orientierte SURMOF Strukturen aufzubauen. Eine hier verwendete Art von organischen Linkern nennt sich photoaktive Verbindungen. Die räumliche Anordnung dieser photoaktiven Moleküle in der SURMOF-Plattform lieferte also hervorragende photophysikalische Eigenschaften. In der vorliegenden Arbeit habe ich ein Bianthrylchromophor untersucht, das mit metallkoordinierenden Gruppen ausgestattet ist, um einen photolumineszierenden oberflächenverankerten MOF -Dünnschicht (SURMOF) auf Zn-bianthrylbasis zu konstruieren. Die Zn-bianthryl-SURMOF haben eine gestapelte 2D-Schichtstruktur, die bei Anregung mit ultraviolettem (UV) Licht eine Cyan-Lumineszenz zeigt. In Reaktion auf die verlängerte UV-Bestrahlung in der Umgebungsbedingungen, zeigte der SURMOF auf Zn-bianthrylbasis jedoch eine deutliche Änderung der optischen Eigenschaften des Grund- und des angeregten Zustands, ohne seine Kristallstruktur zu verlieren. Eine detaillierte spektroskopische Untersuchung unter Verwendung von UV-Vis, FTIR, Raman, EPR und NEXAFS zeigte die Bildung der stabilen oxidierten Produkte von Bianthryl (Endoperoxid-Bianthryl) im SURMOF. Die vorliegende Studie identifiziert die

Schlüsselfaktoren des Bianthryloxidationsprozesses, die einen selbstsensibilisierten photochemischen Weg beinhalten. Auch redoxaktive metallorganische Gerüste (MOFs) auf Viologenbasis haben in den letzten Jahren unter dem Gesichtspunkt intelligenter optisch aktiver Materialien großes Interesse gefunden. Hier wird ein Dicarboxylat-funktionalisiertes Viologen, 1,1'-Bis (4- (carbonsäure) phenyl) - [4,4'-bipyridin] -1,1'-diiumdichlorid (viologen), als Linker zum Aufbau von SURMOF-Dünnschichten unter Verwendung eines Schicht-für-Schicht-Flüssigphasen-Epitaxie-Verfahrens hergestellt. Diese Technik erzeugt ein hochkristallines, orientiertes SURMOF-2 auf Viologenbasis. Der orientierte, monolithische, kristalline SURMOF-Dünnschicht zeigt im Vergleich zu den zuvor beschriebenen Pulver-MOFs auf Viologenbasis eine schnell reversible Photochromie. Die Photochromie im SURMOF wird mittels UV-Vis, EPR und XPS untersucht.

# 1 Introduction

## 1.1 Metal-organic frameworks (MOFs)

Metal-organic frameworks (MOFs) are hybrid porous materials consisting of a metal center connected with an organic linker<sup>1</sup>, as shown in **figure 1.1**. MOFs are also referred to as porous coordination polymers (PCPs) or porous coordination networks (PCNs). They are hybrid organic-inorganic materials containing di-or higher topic organic linkers, and inorganic units called vertices, metal nodes, or metal-oxo cluster.<sup>2</sup>

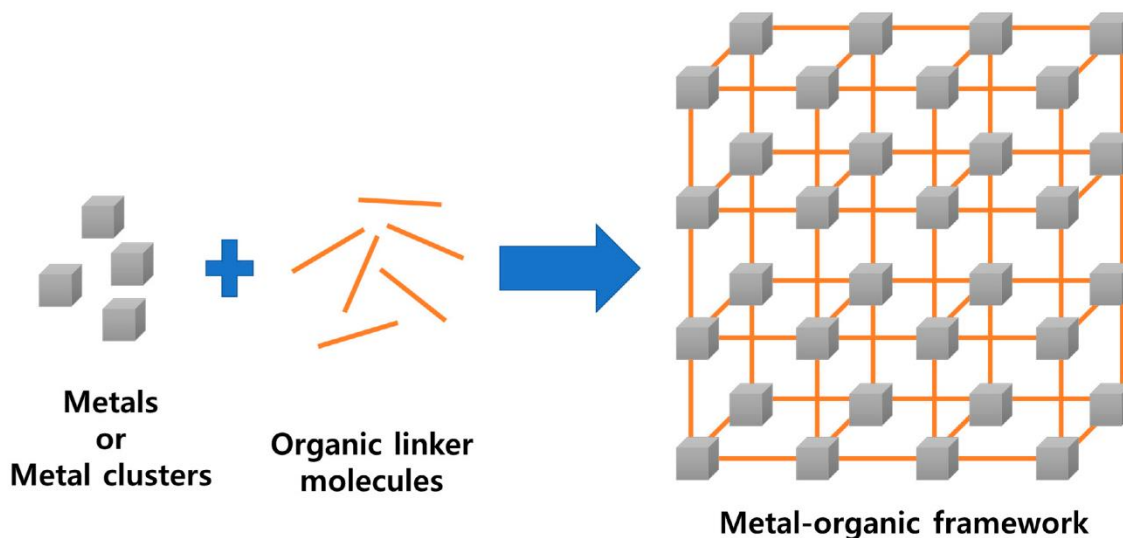


**Figure1-1:** Schematic of the metal-organic framework (MOF) structure, the figure was reproduced from ref.<sup>3</sup>

Because of the large number of combinations between metals and organic linkers, there are more than 100,000 different crystal structures described in literatures.<sup>4</sup> MOFs have large pore sizes with high surface area compared to conventional porous materials including zeolites and carbon area,<sup>5</sup> as shown in **figure 1.2**.

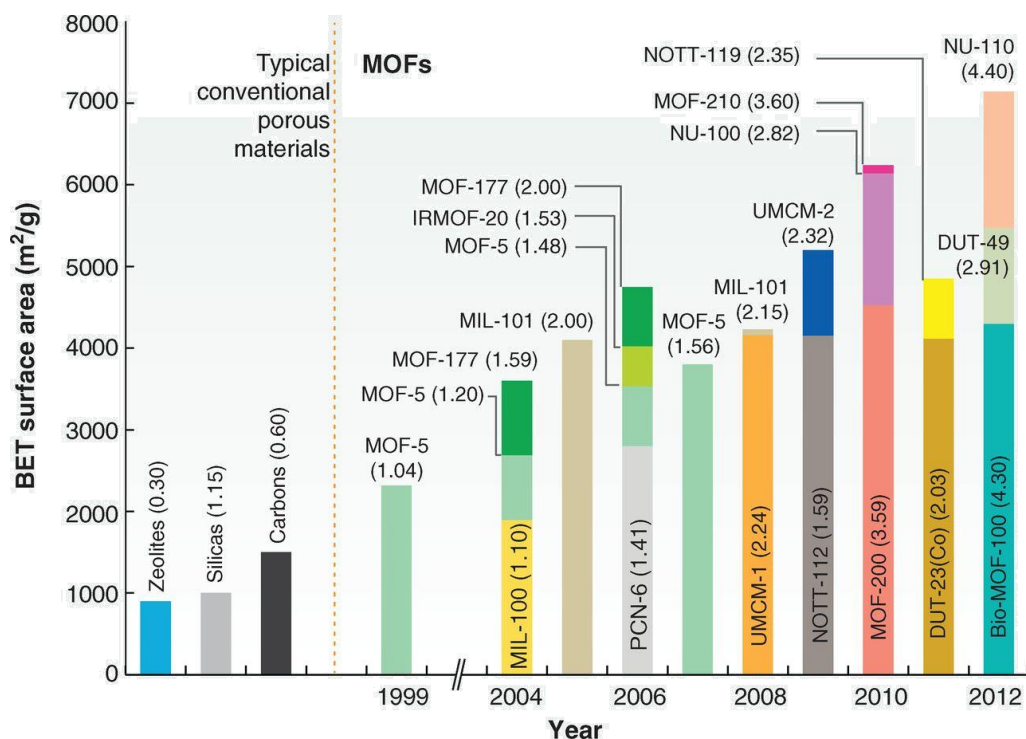


**Figure 1-2:** Evolution of MOFs with ultrahigh BET surface areas compared to conventional porous materials. The values in parentheses stand for the pore volume (cm<sup>3</sup>/g). This picture was reproduced from Ref.<sup>1</sup>

As a result of the unique chemical and physical properties of MOFs, they have been used for several applications including gas storage<sup>6</sup>, separation<sup>7</sup>, adsorption<sup>8</sup>, water harvesting<sup>9</sup>, catalysis<sup>10-12</sup>, energy<sup>13</sup>, sensing<sup>14,15</sup>, diagnosis<sup>16</sup>, therapy<sup>17,18</sup>, and advanced environmental and energy-based technologies<sup>19-22</sup>, as shown in **figure 1.3**. MOFs have high thermal and chemical stability. Thus, MOFs are an attractive topic for scientists from different disciplines to utilize this kind of materials for different applications.

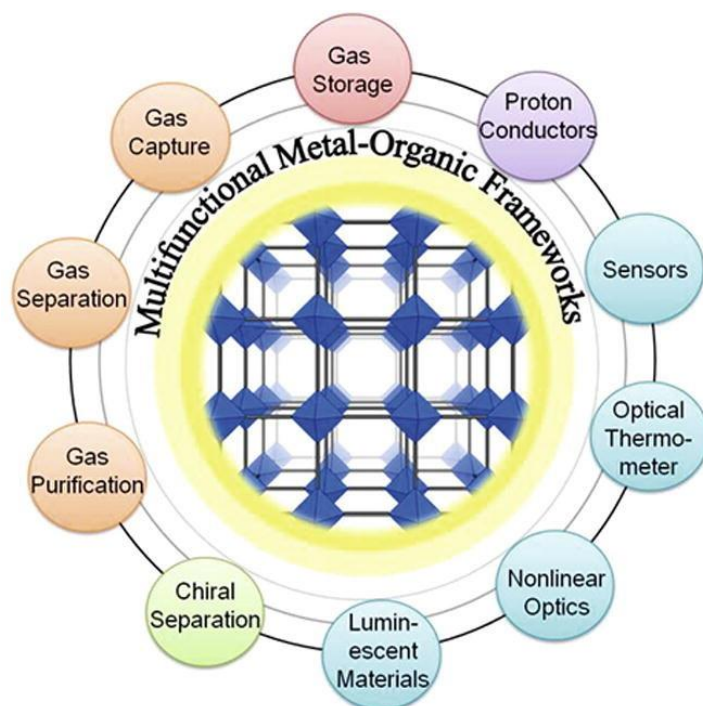


**Figure 1-3** :Applications of MOFs materials. The figure was reprinted with permission from Elsevier, Ref.<sup>23</sup>

As aforementioned, MOFs consist of two important parts, firstly, the secondary building units (SBUs) are molecular complexes and cluster entities that coordinate with multitopic organic linkers to afford the porous coordination networks.<sup>2</sup> The geometric and chemical properties of the organic linkers and the secondary building units determine the topology of these networks. The secondary building units consist of a combination of metal ions that are attached to multidentate functional groups such as carboxylates.<sup>24</sup> Therefore, the metal cluster in the material affects the stability and practical use. For instance, the Cu-acetate paddle wheel with linker such as benzene-1,3,5-tricarboxylic acid (BTC) yields a MOF called Cu-HKUST-1 which is stable after water removal.<sup>25</sup> When the Cu-acetate paddle wheel was changed to the Zn-acetate paddle wheel, it was found that the Zn-HKUST-1 MOF is unstable after water removal.<sup>26,27</sup> The secondary building units can be classified according to the number of points of extensions, points of extension can be defined as the number of possible connections between one metal cluster and other metal clusters through organic linkers, starting from three extension points to 66 points of connection, as shown in **figure 1.4**. The secondary building units (SBU), are connected to the organic linkers via coordination bonds through nitrogen atoms, oxygen, more rarely by fluorine and nonmetal atoms.<sup>28</sup> The coordination with carboxylates was found to yield the strongest coordination bonds. Also, the

points of connections play role in the determination of the geometry of the MOFs, for instance, five points of extension can afford the square pyramid, while four points of the extension can afford a rectangular.

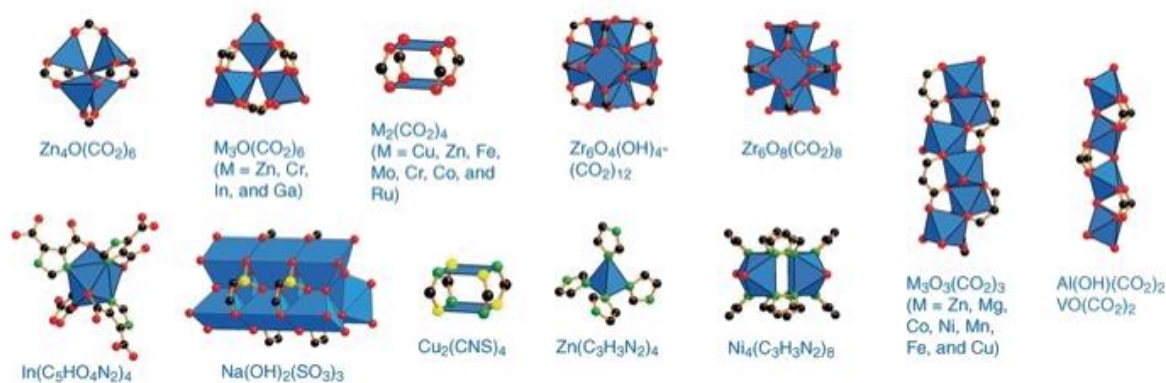


**Figure 1-4:** Metal nodes or clusters from Ref.<sup>1</sup>

Metal centers in the MOFs can be metal nodes or metal clusters. For example, copper in copper-based MOFs is mostly present as paddlewheel.<sup>24</sup> The same metal topology was also observed for metals such as Chromium (III), Rhodium(II), Zinc(II).<sup>29</sup> Zn(II), and Cu(II) paddlewheels form five coordinated bonds, four coordination bonds resulted from the coordination with the oxygen atoms of the carboxylate groups in the linker. The fifth coordination bond results from the coordination of the metal with water molecules or solvents. As a result, these metal paddlewheels are classified as a four-point of extensions, which afford MOFs with square planar geometric. The second important part which plays a crucial role in building MOFs is the multi-topic linker which connects two or more-vertices to afford a solid structure. Linkers show high importance in building MOFs in which pore size and the chemistry can be controlled by changing the functionality and the length of the used linkers.<sup>30</sup> In the design of the bulk MOFs, the linker is not necessary to have strictly linear (ditopic) molecules. It can also be tri to octa-topic complexes.<sup>31,32</sup> **Table 1-1** shows different topologies realized in MOFs.

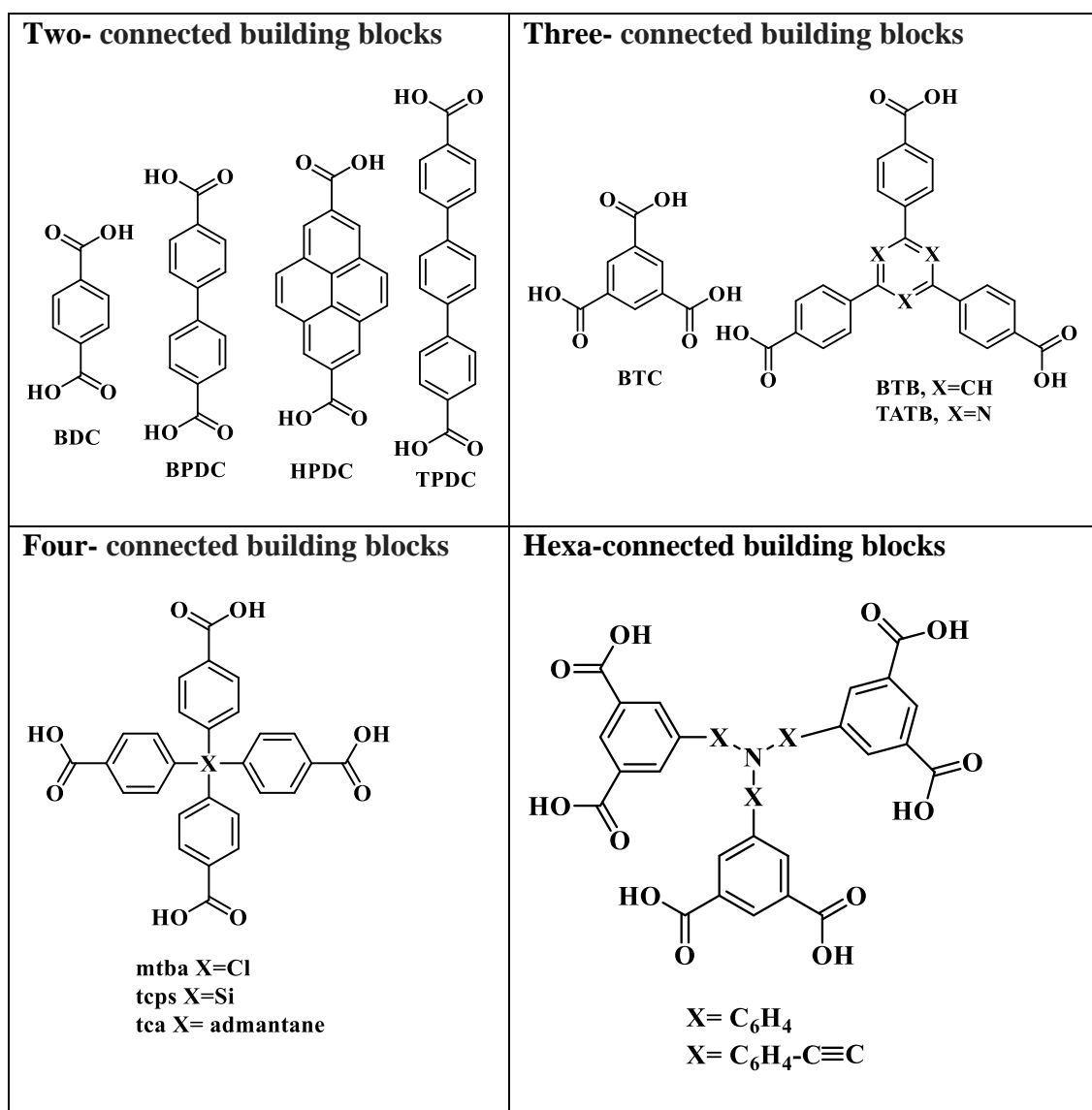


**Table 1-1:** Examples of MOF linkers. They were classified according to the number of topics.<sup>32</sup>

MOFs can be prepared using different methods including conventional methods such as solvothermal synthesis, hydrothermal synthesis and grinding.<sup>31</sup> In addition, modern technologies techniques have been reported in the synthesis of MOFs such as microwaves, ultrasonication, ..etc, as shown in **figure 1.5**. The selection of the method depends on the nature of the reactants and the nature of the desired compounds.

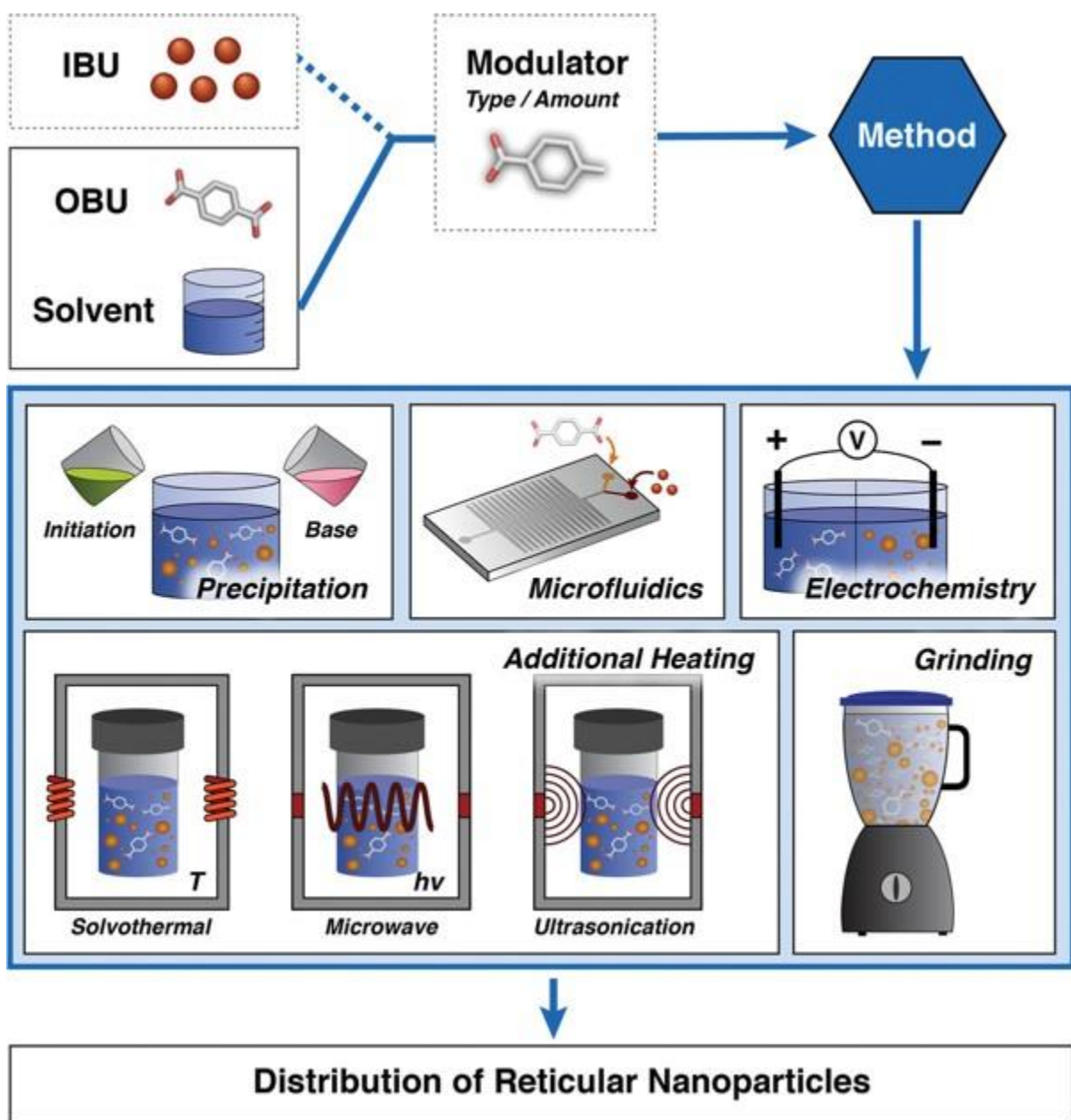


**Figure 1-5:** The synthesis of reticular nanoparticles. This picture was reproduced from ref.<sup>31</sup> (IBU) means inorganic unit and (OBU) means an organic linker or organic building block.

The properties of the MOFs in demand can be controlled via the rational selection of the starting materials, e.g. SBUs and organic ligands, or can be modified after the construction of the MOFs.<sup>33</sup> Consequently, the pore size can be increased without changing the topology of the crystal via increasing the length of the linker that has been used, as shown in **figure 1.6**. It is called the expansion of the metal-organic frameworks, for example, the MOF-5 series which were expanded, in which the linkers were variously functionalized. This increase in the length of the linker

produced an isostructural series with tunable pore size.<sup>34,35</sup> This property opens the door to produce materials with tailored physicochemical properties.<sup>31</sup> However, increasing the length of the linker led to an increase in the pore size of MOFs, but also it produced large pores that tend to have interpenetration. That means small crystals of the MOFs formed inside the crystal of the large pores. In conclusion, increasing the length of linkers afforded inter-penetration instead of affording large pores size, also by increasing the length of the linker, the solubility of the linkers decreases. It is reported that the interpenetrations can be suppressed by changing the concentration of the reactants, temperatures, or other experimental conditions.<sup>30</sup> Another way has been reported called a decoration process that means the vertices can be replaced by a group of vertices. This method led to a structure with open pores and prevented interpenetration.

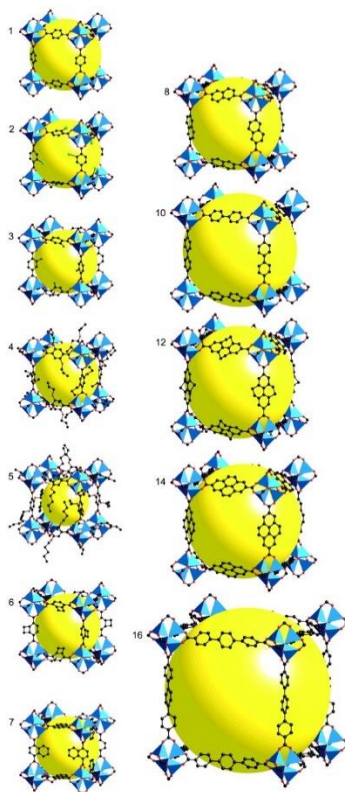


**Figure 1-6:** Expansion of the metal-organic framework, for example, MOF-5 series which is expanded and variously functionalized organic linkers. That picture was reprinted with permission from AAAS, Ref.<sup>30</sup>

MOFs have an ultrahigh porosity, large surface area and provide the option to tune their inner and outer surface areas. Because of the rational selection of linkers or metal vertices, MOFs are used to realize a plethora of various applications. MOFs have been applied for drug delivery<sup>36,37</sup>, gene delivery<sup>38-39</sup>, photodynamic therapy<sup>41</sup>, photothermal therapy<sup>42,43</sup>, heterogeneous catalysis<sup>44,45</sup>, gas

storage<sup>6,46</sup>, adsorption<sup>47-49</sup>, separation<sup>7,50</sup>, water harvesting<sup>9</sup>, catalysis<sup>51</sup>, energy applications<sup>13,52</sup>, solar cells<sup>53</sup>, hydrogen generation<sup>54</sup>, sensing<sup>14,55</sup>, analytical chemistry<sup>56</sup>, diagnosis<sup>16</sup>, and therapy.<sup>17</sup> Besides, MOFs have been used in catalysis<sup>57</sup>, photocatalytic CO<sub>2</sub> reduction using visible light<sup>58</sup>, CO<sub>2</sub> capture, and storage.<sup>59-61</sup> With regard to the applications, bulk powder MOFs are not always suitable. Heterogeneous morphology, weaker adhesion to substrate, and high defect densities present in the powder MOFs greatly influence the structure property correlation. Using a layer-by-layer liquid-phase epitaxy (LPE) method to fabricate surface-anchored MOF (SURMOF) has been found as a potentially useful approach to fabricate monolithic thin films with reduced defect density.<sup>62</sup>

## 1.2 Surface anchored Metal-Organic Frameworks (SURMOFs)

For many applications, integrating MOFs into devices is of paramount importance. Several methods including growing MOFs into thin films were reported.<sup>63</sup> Thin-film technological applications open new opportunities to avoid the limitation of powder MOFs.<sup>4</sup> There is a need to develop new methods suitable to deposit MOFs onto different types of substrates in connection with advanced applications. Several methods have been established to fabricate MOFs thin films, including chemical vapor deposition (CVD)<sup>64</sup>, atomic layer deposition (ALD)<sup>65</sup>, substrate-seeded heteroepitaxy (SSH)<sup>66</sup>, bottom-up modular assembly (BMA)<sup>67</sup>, electro-chemical fabrication (ECF)<sup>68</sup> as well as liquid-phase epitaxy of metal-organic frameworks<sup>62</sup> or surface anchored metal-organic frameworks (SURMOFs). Epitaxy is the process of growing a crystal on another crystalline substrate with a fixed phase relation between the epitaxially grown film and the nucleating surface.<sup>69</sup> This method has many advantages, it allows to control the thickness and crystal orientation, decrease the roughness of the obtained SURMOFs. Furthermore, the layer-by-layer approach is a suitable method to get multilayered films using heteroepitaxy and patterned SURMOFs. The lbl method has been used for many advanced applications such as catalysis, gas adsorption, gas separation<sup>70</sup>, sensor<sup>71</sup>, electronic devices<sup>72</sup>, and photovoltaic.<sup>73</sup> This fabrication technique opens the door for using MOFs in more advanced technological applications such as photonic, electronic, display, laser, memory switching, and supercapacitor devices. Thus, SURMOFs not only become a prime candidate for industrial applications but also to study physical properties of MOFs such as optical, photonic, electronic, photoluminescence, and nonlinear optical properties, as well as the static dielectric and super-capacitance properties. This technology can be used to study SURMOFs using a surface-sensitive technique such as X-ray photoelectron (XPS) and other techniques.

### 1.2.1 Fabrication of SURMOFs

There are several methods to grow MOFs thin films. The most promising method is layer-by-layer deposition using the liquid-phase epitaxy method (LPE).<sup>74,75</sup> SURMOFs offer several advantages compared to powders fabricated using the conventional solvothermal method. The LPE approach for the synthesis of SURMOF thin-films consists of sequential exposures of the functionalized substrates to individual reactant solutions of ethanol metal-oxo-cluster followed by a linker solution, at a temperature ranging from 25°C to 65°C. The individual immersion steps are separated by rinsing with pure ethanol to remove uncoordinated reactants, side products, and to prevent the formation of the large-scale crystals. After optimization of the reaction conditions, the previous steps can be repeated several times until the desired thickness is obtained, as shown in **figure 1.7**. This method has several advantages compared to the other methods. It offers to tune thickness by controlling the number of deposition cycles.<sup>76</sup> In addition, the obtained thin films are compact, high quality, open porosity, highly orientated<sup>77</sup>, homogenous morphology<sup>78</sup>, and with low defects density compared to powder MOFs.<sup>79</sup> In addition, they can be deposited on a large scale for industrial applications.<sup>80</sup> There are several techniques that can be used to grow SURMOF by LPE such as spin coating<sup>81</sup>, dipping robot<sup>82</sup>, and quartz crystal microbalance (QCM)<sup>83</sup>, spray method<sup>80</sup>, pump methods<sup>84</sup>, and flow-based automation methods.<sup>85</sup>

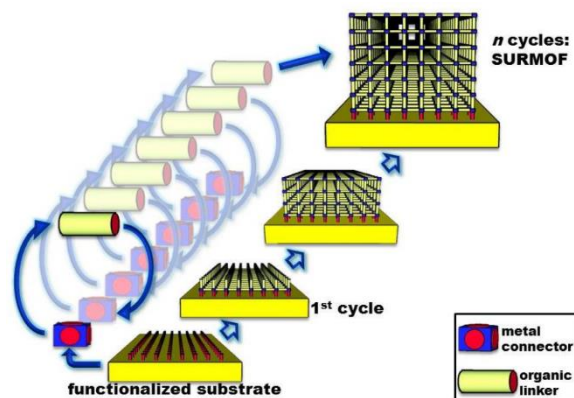


**Figure 1-7:** The scheme of prepared SURMOFs by using LPE layer-by-layer techniques the functionalized substrate is sequential exposed to the metal solution and linker solution with rinsing using pure ethanol in between each step. The figure was reprinted with permission from Elsevier. Copyright (2015) ref.<sup>86</sup>

To grow SURMOF, choice a suitable substrate and suitable surface modifications is a crucial step in the deposition of SURMOFs to produce desired thin films to fulfil the planned-applications.

### 1.2.1.1 Substrates

SURMOFs can be grown on a huge variety of substrates. The selection of a suitable substrate as well as the proper functionalization depends on the desired application. As demonstrated in the literature, great efforts have been devoted to establishing various deposition techniques for SURMOFs.<sup>64,65,77,87-90</sup> These techniques opened the door for deposition MOFs onto different substrates which afforded compact and homogenous MOFs thin-films. A wide variety of substrates have been used for the growth of the SURMOFs including the planar substrate such as TiO<sub>2</sub>, FTO, quartz, SiO<sub>2</sub>, Au, and flexible substrates like aluminium foil, plastic, fibres, metal oxides, or polymers.<sup>91</sup> Moreover, nano and micro-particles were also used to grow core-shell particles, for instance, commercially available magnetic beads were functionalized and used to grow HKUST-1 (Hong Kong University for Science and Technology) on them.<sup>92</sup> The produced magMOF particles were used as a chromatographically active stationary phase to separate solvents from mixtures such as pyridine and toluene.

### 1.2.1.2 Functionalization of the substrate

To grow SURMOFs by the LPE approach, one of the crucial factors that should be thoroughly considered is the functionalization of the substrate. This step is important to get the desired orientation. The LPEs approach has different advantages, such as providing highly oriented thin films, while the other approaches provide polycrystalline films. A convenient way to functionalize gold substrates is to use organothiols. These compounds are organic molecules that have the structure HS-R-X<sup>93</sup>, as shown in **figure 1.8-a**. The SH group is known as an anchoring group and has a high affinity to attach the gold substrate Au-S-R-X, while X is known as a terminate group. Organothiol compounds are distinctive due to the easy growth on the substrate by immersing the substrates into a solution of organothiols, which produces a self-assembled monolayer (SAMs). Accordingly, head groups can be classified into the monodentate and bidentate groups. Organothiol compounds have an affinity to attach with the metal (Au, Ag, Cu) substrate only. As a result, they cannot form a second layer. The terminate group of SAMs used for functionalization gold substrates, can be COOH, OH, NH<sub>3</sub>, pyridine such as 16-mercaptohexadecanoic acid (MHDA), 11-mercapto-1-undecanol (MUD), 4'-carboxy-phenyl-4-methanethiol (TPMTA) and 9-carboxy-10-(mercaptomethyl) triptycene (CMMT), as shown in **figure 1.8b**. Another example is the silicon substrate which can be treated with silane SAMs.<sup>94,95</sup> In addition, other factors are affecting the orientation of MOF thin film growth such as the density of the functional groups on

the surface.<sup>96</sup> **Figure 1.8b** shows the structures of MHDA, TPMTA, and CMMT SAMs attached with Au (111) substrate, respectively.

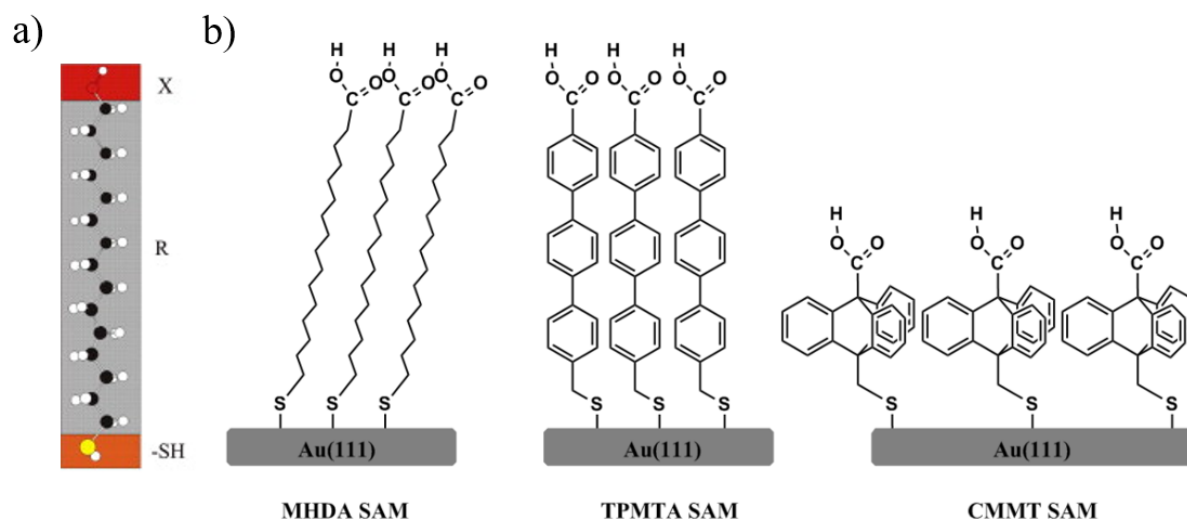


**Figure 1-8:** a) SAMs, SH-R-X, shows structure of an organothiol used in forming SAMs the anchor group (orange box) consisting of the sulfhydryl (SH) unit, a coupling unit R (in this case an alkyl group), and a terminal function X. This picture was reprinted with permission from Elsevier ref.<sup>93</sup> ; b) example of SAMs attached to Au-substrate. This picture was reproduced from ref.<sup>96</sup>

## 1.2.2 Techniques for the growth of SURMOFs

Several LPE techniques have been set up for growing homogenous morphology SURMOF/ MOFs thin-films or minimizing the roughness, control thickness, monolithic, and free pinholes and cracks. The techniques that have been used include hand spray methods<sup>80</sup>, spin coating<sup>81</sup>, dipping method<sup>82</sup>, pump method<sup>84</sup>, and quartz crystal microbalance (QCM) methods.

### 1.2.2.1 Spin coating

This is a method used to grow metal-organic framework (MOFs) thin films either oriented or polycrystalline.<sup>81</sup> The spin coating method has several advantages. First, it provides MOFs thin films with high throughput and allows for the cost-effective construction of thin films. Furthermore, this method requires shorter reaction times for the preparation of MOFs thin film than other methods, such as dipping method and pump methods. It decreases the amount of required chemicals and solvents as compared to other variant of the LPE-process. The thickness of the SURMOFs can be controlled by adjusting the number of deposited cycles. This deposition method can be fully automated using a spin coating machine consisting of four micro-syringes,

which contain metal precursors solution and linker solution. The other two syringes contain pure ethanol to remove the uncoordinated metals precursors and side products, as shown in **figure 1.9**. The metal precursors solution and linker solution drop through these micro-syringes on the substrate in a certain duration of time and spin coating with specific speed rpm in a continuous system respectively. Also, these two steps are separated by rinsing with the pure ethanol. The drops deposited on the substrate are spread homogeneously by centrifugal forces.

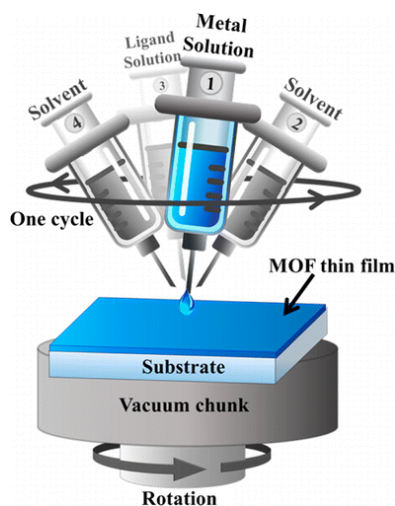


**Figure 1-9:** Schematic representation of spin coater is using for the fabrication of MOFs thin films by LPE approach, syringe number 4, and 2 are pure ethanol 1, and 3 are a metal solution, and the linker solution syringe respectively. This picture was reprinted with permission from ref<sup>81</sup> Copyright © 2016, American Chemical Society.

The spin coating technique was used in the synthesis of HKUST-1, zeolitic imidazolate frameworks (ZIF-8),  $\text{Cu}_2(\text{bdc})_2 \cdot x\text{H}_2\text{O}$ , and  $\text{Zn}_2(\text{bdc})_2 \cdot x\text{H}_2\text{O}$  (bdc, refers to benzene-1,4-dicarboxylic acid). The pre-functionalized substrate is placed on a vacuum chuck; the speed spin coater is optimized to start from slow to high-rotating speed. Ethanol solution of metal precursor (0.05ml) is added and spin coated for 5 seconds at 25°C, followed by a rinsing step with a pure ethanol (0.05ml) to remove uncoordinated metal precursors and the side products. Thereafter, ethanol solution of the linker (0.05ml) is deposited and spin coated for 5 seconds, followed by rinsing step with a pure ethanol (0.05ml) to remove uncoordinated precursors and side products. The different steps described above from one deposition cycle, and by repeating cycle several times until the desired thickness is obtained. Several parameters can be optimized, which have an effect on the thickness e.g., the volume of solvents, the number of cycles, and the speed of rotation of spin coating.

### 1.2.2.2 Spray method

The hand spray method can also be used to grow SURMOFs based on LPE-method.<sup>80</sup> This method allows to decrease the time of preparation of SURMOF by two orders of magnitude compared to other LPE-methods. Besides, it provides high thickness with a deposition cycle in comparison with other LPE methods. This system is built on a nozzles system basis, as shown **figure 1.10**. The pre-functionalized substrate was fixed on the holder and 1 mM of ethanol solution of Cu (CH<sub>3</sub>COO)<sub>2</sub>·H<sub>2</sub>O or ethanol solution of a metal nodes was sprayed for 15 seconds, followed by spraying the ethanol solution of the linker, ethanol solution of BTC in the case of HKUST-1, for 25s in sequence. The spraying of ethanol metal solution and ethanol solution of the linker was separated by an interval of 35s to allow precursors to coordinate with the previous active groups on the substrate. These two periods of spraying were separated by an intermediate rinsing step with pure ethanol for 5s to remove the uncoordinated precursors and the side products. Finally, this process produced one deposition and took a time of 2 mins. The desired thickness can be obtained by repeating the numbers of cycles. Furthermore, some factors have an effect on the produced thickness, such as the pressure of gas carrier for the solution of metal precursors and linkers solution, the distance between nozzles and substrate, and flow rate. The pressure of the gas used in the case of HKUST-1 and SURMOF-2 was 0.2 mbar. In addition, an automated spray setup is available that is working with an automated program. The automated spray technique affords a high roughness thin-film. As a result, manually hand spray is commonly used than automatically spray techniques. The automatic spray setup machine and manual hand spray are shown in **figure 1.10**.

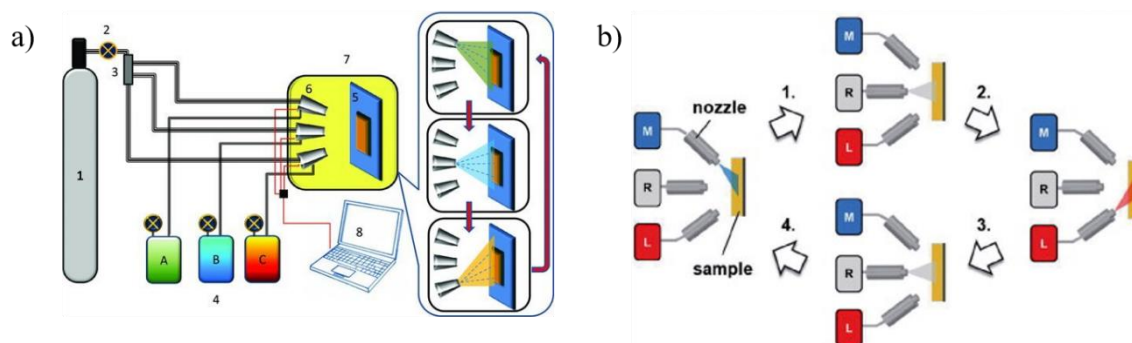


**Figure 1-10:** a) Setup of the automated spray method which used to fabricate SURMOFs with the spray method: (1) Gas supply, (2) gas flow controller (3) three-way gas valve (4) (A, B, C) solutions storage containers (5) sample holder (6) dosing valves, (7) spray chamber, (8) PC. The

picture was reprinted with permission from ref;<sup>80</sup> b) Schematic diagram of the steps of producing one cycle-SURMOF using a manual setup of spray method, M is the metal solution, R is the rinsing liquid, and L is the linker solution. By repeating the previous step, the desired thickness can be obtained. This picture was reproduced from ref.<sup>74</sup>

### 1.2.2.3 Dipping robot

The dipping robot method can be used to get SURMOFs of highly homogenous morphology with low roughness.<sup>82</sup> In addition, it does not consuming a large amount of solutions. It requires a relatively long time in comparison to the spray method and spin coating method. The functionalized substrate is dipped into the metal solution for 10 min container No. (1), followed by dipped into pure ethanol Container No. (2) for 2 mins to remove uncoordinated metal precursors or side products. Thereafter, the substrate is dipped into the ethanol solution of the linker on container No. (3) for 15 mins to allow the metal node to coordinate with linker, followed by dipped into the substrate into container No. (4) which contains ethanol to remove uncoordinated precursors and the side products. A full deposition cycle consists of the steps described above, as shown in **figure 1.11**. The thickness can be controlled by repeating the number of cycles. This method has the advantage of combining the sonication and the heating system. Thus, it yields a highly homogenous morphology of the deposited MOF thin-films. This deposition time was used to prepare HKUST-1.

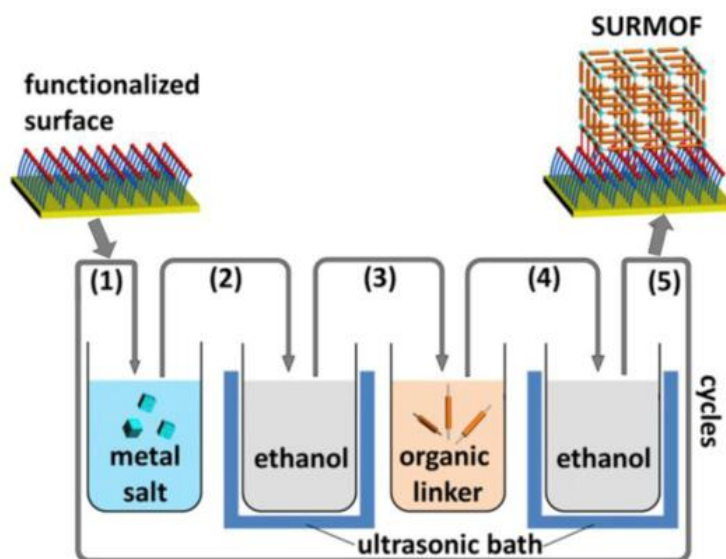


**Figure 1-11:** The dipping robot setup is using to fabricate SURMOF equipped with an ultrasonic bath. The factionalizing substrate is immersed in the ethanol metal-salt solution (1), pure ethanol

(2), ethanolic organic-linker solution (3), and pure ethanol (4) respectively. These four steps form a deposition cycle, which can be repeated many times. The figure was reprinted with permission from Elsevier Copyright (2015) ref.<sup>82</sup>

#### 1.2.2.4 Pump method

The automated pump technique has been built to control the temperature precisely during the synthesis of SURMOFs by using a heating and cooling circulation system ranging from -20°C to 100°C.<sup>84</sup> In this method, the functionalized substrate is placed inside the chamber jacket, sample cell. The system consists of four pumps with three different containers. The fourth pump is used to pump out the solution at the end of every step, as shown in **figure 1.12**. The first pump transfers the metal precursor solution for a specific programmed time. The metal solution covers the substrate for a specific time to allow the metal precursor to coordinate with the functional group exposed by the surface of the substrate. Consequently, the fourth pump starts to pump out the uncoordinated precursor solution and side products at the end of the reaction time. Thereafter, rinsing with pure ethanol is important here to remove the uncoordinated metal precursors and side products. Consequently, the linker solution is transferred by pump (3) to allow the active layer of metal nodes to coordinate with the linker. At the end of the previous step, pump No (4) removes the linker solution from the sample cell, followed by a rinsing step. The previous steps afford one deposition cycle. These previous steps can be repeated several times until the desired thickness can be obtained. For instance, the synthesis of HKUST-1 has been performed by using the pump system, as described in the following steps.

The functionalized substrate was placed inside the sample cell, then:

- 1-The functionalizing substrate was immersed with freshly prepared metal solution of  $\text{Cu}(\text{CH}_3\text{COO})_2 \cdot \text{H}_2\text{O}$  (1 mM) for 30 min.
- 2- The substrate was rinsed with pure ethanol for 2 mins. This step was repeated two times.
- 3- The substrate was immersed with ethanol solution of 1,3,5-benzene tricarboxylic acid (BTC, 0.2 mM), as a linker for 1 hour.
- 4- The substrate was rinsed with pure ethanol for 2 mins, two times to complete one cycle.
- 5- By repeating the previously described, a homogeneous coated thin film of HKUST-1 was obtained.

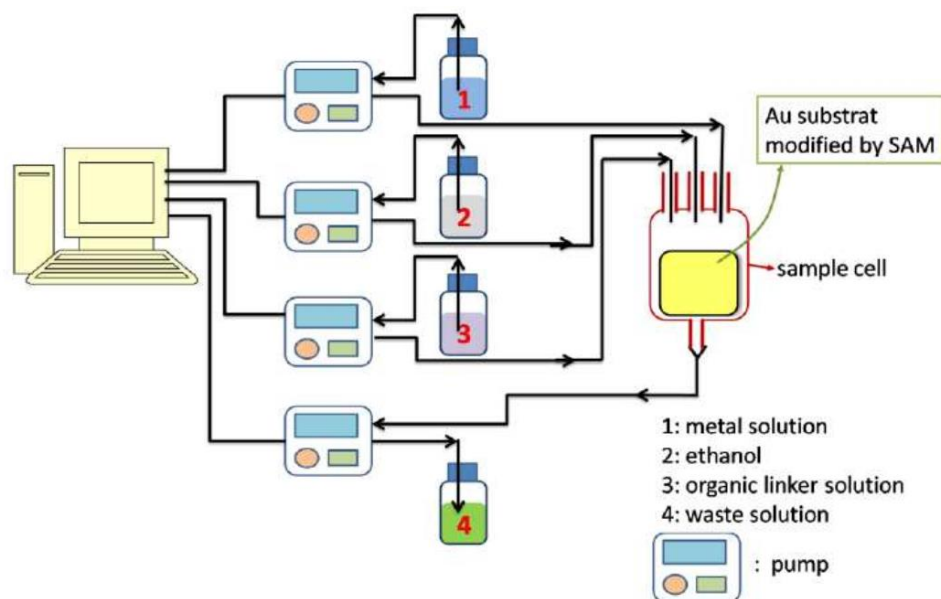


**Figure 1-12:** The schematic diagram for the pump system that is used to grow SURMOFs via layer-by-layer LPE. The figure was reprinted with permission from ref <sup>84</sup> Copyright (2011) American Chemical Society.

#### 1.2.2.5 Quartz crystal microbalance (QCM)

The principle of the QCM is based on the piezoelectric property, when applying alternating electric voltages to the quartz leads to produce mechanical shear oscillations.<sup>83,97</sup> **Figure 1.13** shows the QCM step up. In the field of SURMOFs preparation, QCM is used to monitor the deposition of MOFs on the quartz (thin films), and the oscillation frequency allows to determine the thickness of the produced thin-film. The data can be analyzed using the **Sauerbrey equation 1.1**.

$$\Delta m = \frac{A\sqrt{Q_q G_q}}{-2f_o} \Delta f \quad \text{Equation 1-1}$$

where  $\Delta m$  is the change in mass,  $A$  is the surface area of the resonator,  $Q_q$  and  $G_q$  is the density and shear modulus of quartz,  $f_o$  is the resonance frequency of the unloaded resonator and  $\Delta f$  is the change in resonance frequency.

From the Sauerbrey equation, any change in the mass of substance on the surface leads to changes in the frequency. A QCM setup can also be used to monitor adsorption and absorption of different molecules in SURMOF.<sup>98-101</sup> The temperature degrees can also be controlled using QCM. Some factors have an impact on the growing SURMOF such as adhesion of the film to the surface of the quartz crystal that affects the measurement accuracy when the accumulated stress is present and the quality of the surface of the quartz crystal. In the reported experiments, pure ethanol was

circulated in QCM until the frequency stabilized. Sequential addition of ethanol solution of  $\text{Cu}(\text{CH}_3\text{COO})_2 \cdot \text{H}_2\text{O}$  and ethanol solution of benzene-1,3,5-tricarboxylic acid (BTC) to the functionalized the quartz crystal. These previous steps of deposition were separated by an intermediate rinsing with pure ethanol to remove uncoordinated metal, linkers, and side products. Finally, controlled thickness thin-film was obtained, as shown in the **figure 1.14**.

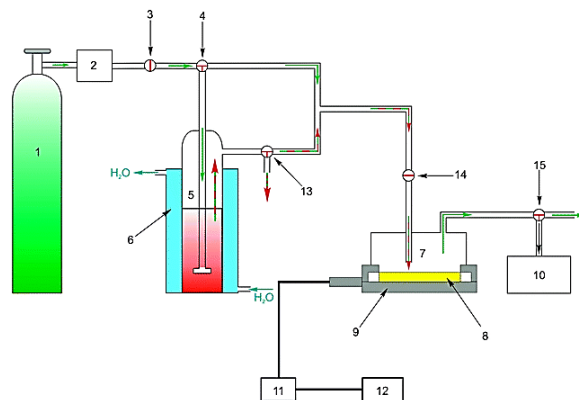


**Figure 1-13:** QCM setup; (1) Inert gas supply, (2) gas controller (FMD PR4000), (3) main valve, (4) three-way valve, (5) storage container with the loading substance, (6) thermostat, (7) glass tube, (8) QCM sensor with gold electrodes, (9) sample holder with electric feed through, (10) membrane pump, (11) impedance analyzer, (12) PC, (13, 15) outlet valves, (14) inlet valve. This picture was reproduced from Ref.<sup>101</sup>

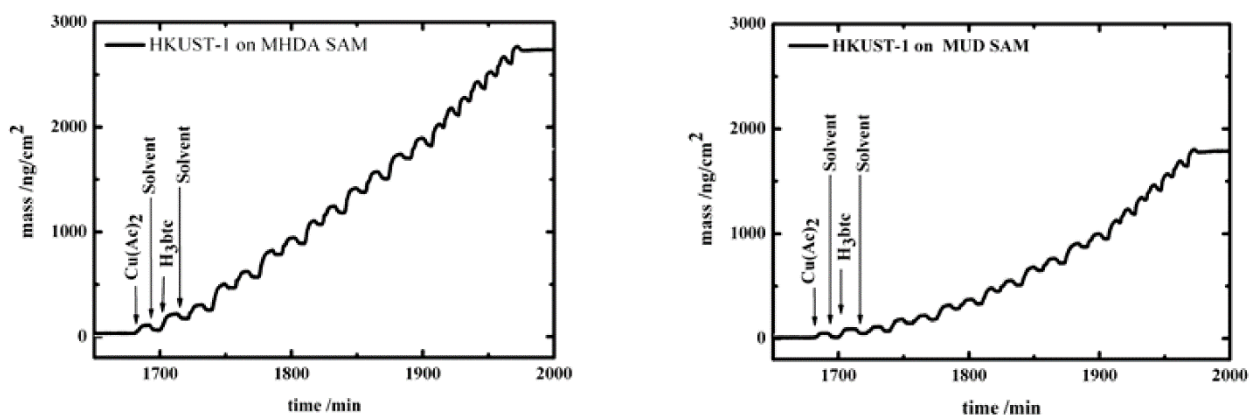


**Figure 1-14:** QCM-D signal as a function of time recorded during the growth of SURMOFs. HKUST-1 was grown in MHDA SAM (left), and MUD SAM (right)-QCM substrates, which were sequentially injected with an ethanol solution of  $\text{Cu}(\text{CH}_3\text{COO})_2 \cdot \text{H}_2\text{O}$ , ethanol solution of  $\text{H}_3\text{btc}$ . These figures were reproduced from Ref.<sup>102</sup>

### 1.3 Photophysical properties of photoresposinve MOFs:

As described above, MOFs are built from the coordination between organic linkers and metal /

metal-oxo nodes, and have accessible pores with large surface area. Since the first report on MOFs in the 1990s by Omar Yaghi<sup>103</sup>, large numbers of MOFs have been reported. These are used mainly for gas separation, adsorption, and storage.<sup>104</sup> The properties of MOFs can be tuned by rational selection of the linkers, or metal nodes with specific properties. On the other hand, the development of new materials, which can alter the physical properties and chemical properties under the effect of external stimuli such as (pressure, heat, light, pH, etc) is attracting a huge interest.

Among these, in particular, photoresponsive materials<sup>105–108</sup> i.e. in response to photoexcitation can undergo a chemical or physical change, are of high importance. Because the physical and chemical properties of the MOFs can be changed by retaining the structural periodicity, these materials have been explored in many applications such as electronic devices, molecular machines, data storage, and sensors.<sup>109–114</sup> The combination of the properties, such as the high surface area and photoresponse<sup>115</sup>, in MOFs can open the doors to the new smart material design, which can be used in the next generation technology sector, such as smart windows, sensors, erasable ink, data storage.<sup>116</sup>

### **1.3.1 Synthetic strategies for combine Photoresponsive materials within MOFs:**

As mentioned before, photoresponsive materials can be assembled into the MOFs. As MOFs are intrinsically porous, encapsulation of photoresponsive guest is also possible.<sup>117</sup> The assembling of photoresponsive materials into MOFs scaffold revealed a variety of photophysical phenomenon, such as photoconductivity<sup>118</sup>, energy transfer<sup>119</sup>, photon upconversion, photoluminescence<sup>120</sup>, and producing singlet oxygen.<sup>121</sup>

#### **1.3.1.1 Followings are the three possible strategies:**

- 1) Linker precursor: Photoluminescent chromophores, like naphthalene<sup>122</sup>, anthracene<sup>123</sup>, pyrene<sup>124</sup>, porphyrin<sup>125</sup>, and photoswitchable chromophores, like azobenzene<sup>126</sup> can be functionalized with suitable functionalities to coordinate to metal center.
- 2) Metal nodes, such as lanthanide metal ions<sup>55</sup>
- 3) Guest: Anthracene<sup>127</sup>, pyrene<sup>128</sup> and azobenzene<sup>126</sup> etc can be encapsulated as guest molecules, as shown in **figure 1-15**.

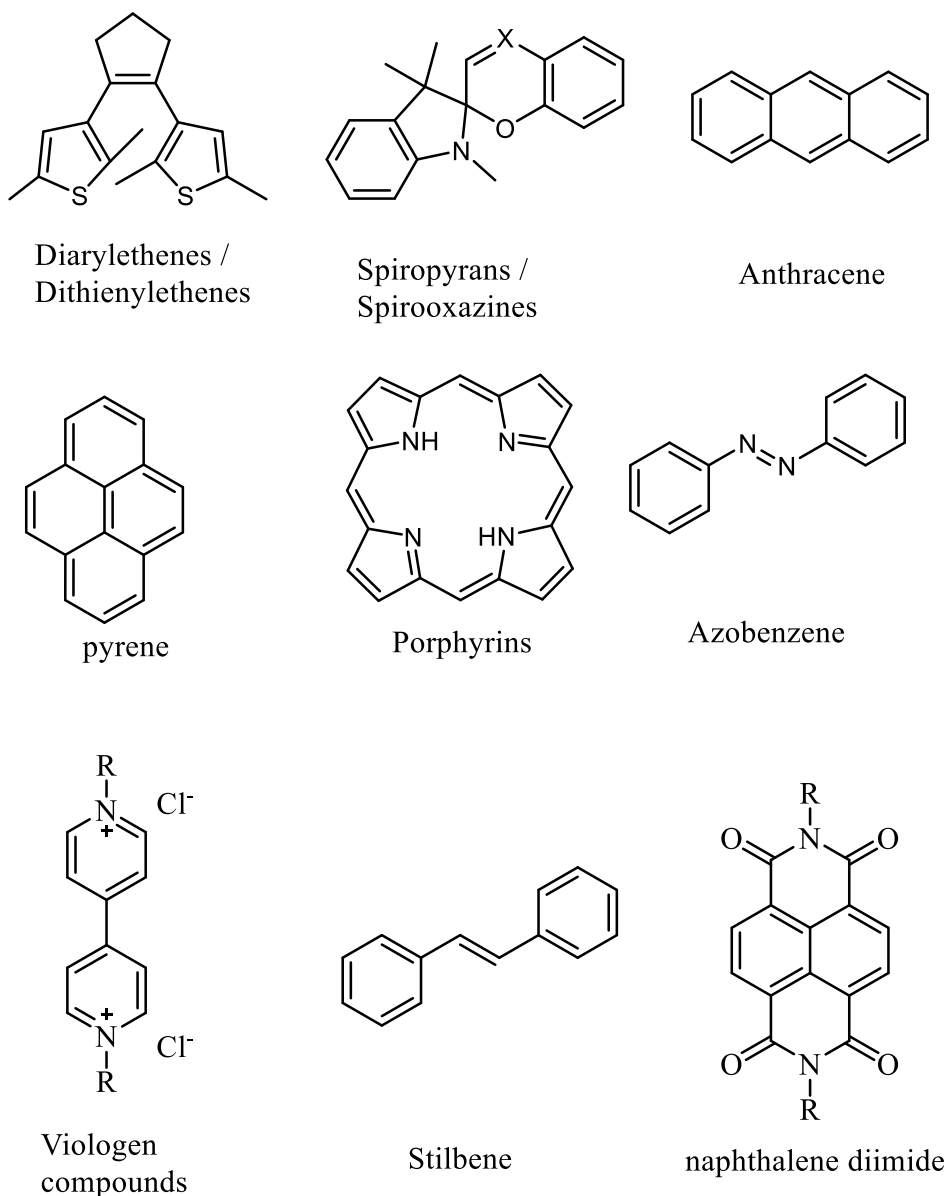


**Figure 1-15:** : Some of the photoactive molecules.<sup>108,22</sup>

### 1.3.2 Types of photoresponse:

As mentioned above the photoresponsive materials are a broad field, but, we will focus of some properties resulted from organic photoresponsive material within MOFs. We can categorize the response upon photoexcitation in the following categories:

### 1.3.2.1 Short-lived photoexcited states decaying to ground state via light emission or Photoluminescence

#### 1.3.2.1.1 Photoluminescence

To exploit MOFs-based photoluminescence<sup>120</sup>, the MOF must release the absorbed energy by radiative pathways. Therefore, the non-radiative pathways in MOFs materials have to be suppressed. The Non-radiative pathways can be resulted due to the presences of torsion, rotation, or low energy vibration to the linker /chromophores. On the other hand, the chromophores that exhibit a high quantum yield emissive in dilute solution, exhibit very low emission or are quenched in the concentrated solution and in the solid-state due to aggregation or self-quenching. For the previous mentioned reasons, the alignment of those chromophoric linkers into the MOFs/SURMOFs platform can control the topological arrangement of linkers that leads to an increase in radiative ways and suppressed the non-radiative ways. In addition, when the chromophores have been aligned into the MOFs platform, they shown emission which is similar to the emission in a dilute solution.<sup>129</sup> For instance, MOFs have been constructed from Zr-2,6-anthracenedicarboxylate exhibited emission as the emission resulted from 2,6-anthracenedicarboxylic acid in N,N-dimethylformamide (DMF).<sup>130</sup> MOFs platform is controlling the chromophore organization and alignment, which reflected on the way of communication between chromophores. Furthermore, the local environment, the alternative orientation of the chromophores embedded within the framework, the spatial orientation, and inter-or intramolecular interaction lead to control the physical properties, and the physicochemical properties. Yet, the most important point is the alignment of the chromophore inside the MOFs with the modulation of the photoluminescence which have a significant effect on photoluminescence.

Photoluminescence based MOFs have been used in many applications e.g. the fabrication of sensors for different amino alcohol, ammonium gas<sup>131</sup>,  $\text{Cr}_2\text{O}_7^{2-}$  and nitroaromatic explosives,<sup>132</sup> also a sensor for detecting  $\text{Fe}^{3+}$  in serum and bioimaging<sup>133</sup> and fabrication white-light-emitting diodes.<sup>134</sup>

#### 1.3.2.1.2 Multi-chromatic emission

MOFs scaffolds provide a good platform where the chromophoric linkers can be aligned. Besides, MOFs scaffold can be built from mixed-chromophoric linkers with a different emission. Different chromophoric linkers can be oriented in two different directions, also the pores of the MOFs can

be infiltrated with different chromophores molecules. This strategy can be used to produce MOFs with different emissions than the emissions of the initial chromophoric linkers. For instance, the reported MOFs  $[Zn_4O(4,4',4''\text{-}(9H\text{-carbazole-3,6,9-triyl)-tribenzoate})_2 \cdot xDMF]_n$ , has blue emission. When it was loaded with two different dyes namely 4-(dicyanomethylene)-2-methyl-6-(*p*-dimethylaminostyryl)-4*H*-pyran (DCM) and coumarin, it exhibited a white emission due to guest@host interaction<sup>134</sup>, as shown in **figure 1-16**. The two different chromophoric molecules have two different emissions red and green emission respectively.

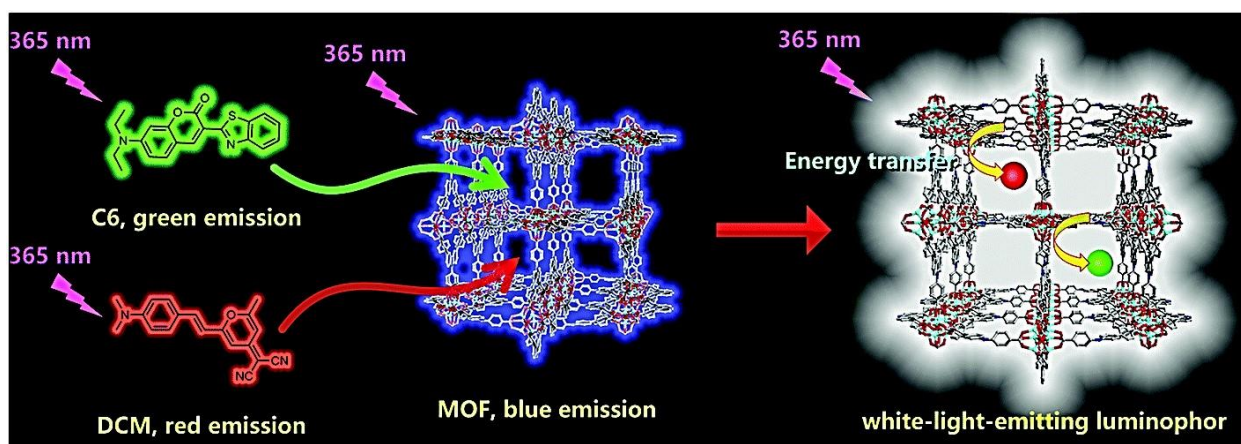


**Figure 1-16:** This figure shows MOF that have blue emission, but after loading with DCM and coumarin (C6), it produced a white-light emitting. This figure was reproduced from ref.<sup>134</sup>

There is a different approach that can be used to fabricate white-light emission by core-shell growth.<sup>135</sup> For instance, rhodamine B dye was encapsulated in the CD-MOF which produced fluorescence rhodamine B dye@CD-MOF. Also, non-emissive MOFs can be encapsulated with different emissive dyes to produce white-light emission such as, encapsulated non-emissive ZIF-8-MOF with different dyes fluorescein, rhodamine B, and 7-amino-4-(trifluoromethyl) coumarin that have different emission via using several methods.<sup>136</sup> This combination was done by three different methods. The first method is that a specific dye was added to the components of ZIF-8 MOFs during preparation, in situ-method, then it was shelled by the pristine ZIF-8 MOF. Therefore, these steps were repeated with others dyes. As a result, the encapsulated dye@ZIF-8 MOF was separated by the pristine ZIF-8 MOF sample to produce a core. Then the three cores were mixed together. Therefore, the mixture of dyes@ZIF-8 afforded white light emission and this method was called as multiphase single-shell, model 1. In the second method, the three dyes were embedded together in the same single crystal of ZIF-8 MOFs. The emission of these dyes was



producing a singlet excited state, as shown in **figure 1-18**. The porphyrin molecule belongs to this category, while using the organic compounds as a photosensitizer have some limitations. As a result, MOF scaffolds provide a system where these chromophores can be aligned to prevent the aggregation, producing materials with large surface area, rigid symmetry, have a high porosity and a good chemical stability. MOF-based photosensitizer solved the issues related to using solvated photosensitizer. In 2013, a first reported photosensitizer-based MOFs (3D-Eu-TPPS) have been fabricated from of porphyrin derivatives.<sup>137</sup> Eu-TPPs produced  $^1\text{O}_2$  via illumination, which have a luminescence at 1270 nm. Due to the limited light penetration within 3D structure, that led to reduce  $^1\text{O}_2$  permeation. Therefore, ultrathin 2D material was prepared to overcome the previous issue related to using porphyrin-based MOF 3D.<sup>138</sup> Lately, more photosensitizer-based MOFs and photosensitizer-based-thin-film MOFs have been reported.<sup>139–141</sup> Photosensitizer-based MOFs have been used in different applications such as digesting a mustard gas to a non-toxic products<sup>142</sup>, oxidizing alcohol to aldehyde<sup>143</sup>, and antibacterial.<sup>141</sup>

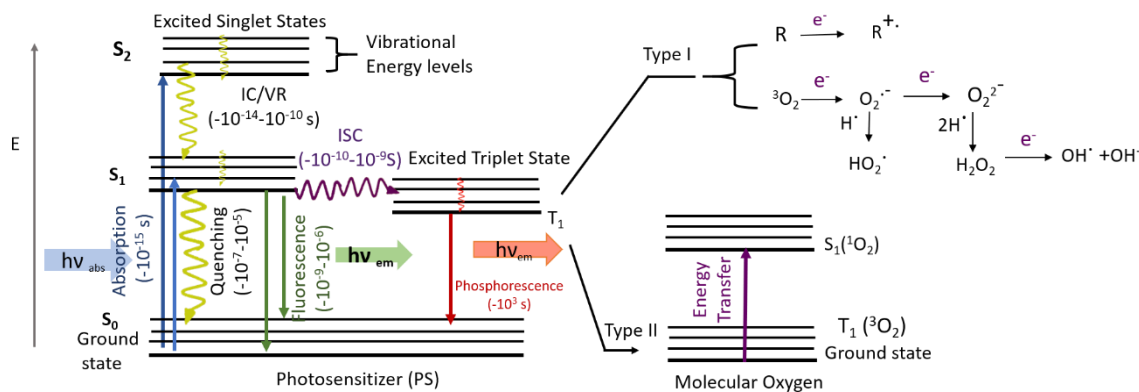
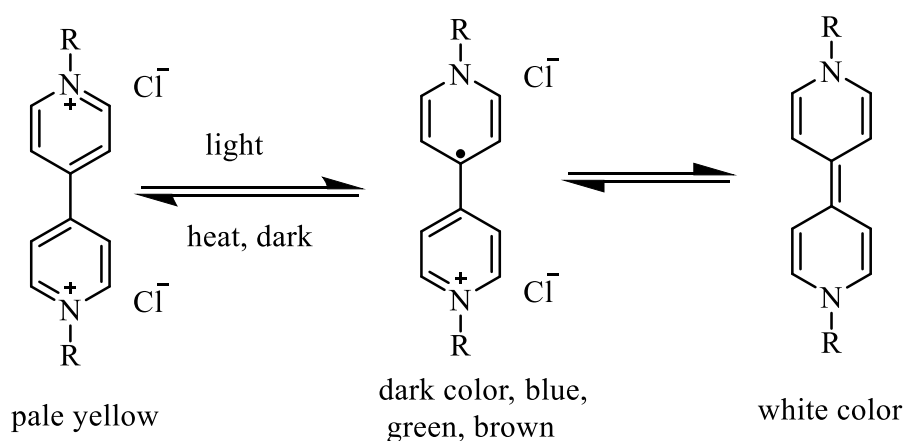


**Figure 1-18** : Jablonski diagram describing the underlying photophysics and photochemistry of photodynamic therapy generation of excited photosensitizer states and reactive dioxygen species. The figure was reproduced with permission from WILEY from ref.<sup>41</sup>

### 1.3.2.3 Stable charge separated state or radical ion state formation

Viologen, and naphthalene diimide, are redox active chromophores. Due to stable oxidation and reduction states, these types of chromophores exhibit persistent, unique color corresponding to the oxidation state. For example, in case of viologen,  $\text{V}^{2+}$  state has a pale-yellow colored, and  $\text{V}^{+}$  which have green, blue, or dark color takes place under external stimuli. The oxidation process can also occur by photoexcitation<sup>144–147</sup>, as shown in the **reaction scheme1**. The change in the structure of viologen compounds under illumination is not a drastic change in the geometry of the linker.

Therefore, viologen compounds are suitable linkers for construction viologen-based MOFs. Upon irradiation the viologen-based MOFs, they are under photoinduced electrons transfer from electron donor i.e. counterion producing viologen radical. This process depends on many factors, one of them is the distance between the pyridinium and an electron donor, such as halide ions, O, N<sub>3</sub>.<sup>148–150</sup> The produced viologen radical-based MOFs are metastable, in which the transition to the initial color happens after exposure to the ambient conditions.<sup>144,149,151,152</sup> This photophysical reaction is very important which makes viologen based MOFs can be used in the data storage, inkless, and erasable ink in printing paper.<sup>153</sup> Furthermore, naphthalene diimide (NDI) in the presences of electron donor, under illumination showed photochromism.<sup>154–157</sup> As a result, MOFs-based (NDI) have been used in coating papers,<sup>158</sup> as sensors to amines, in which the color of NDI based MOFs changed due to electron transfer from amines as a donor to the NDI as an acceptor.<sup>159</sup>

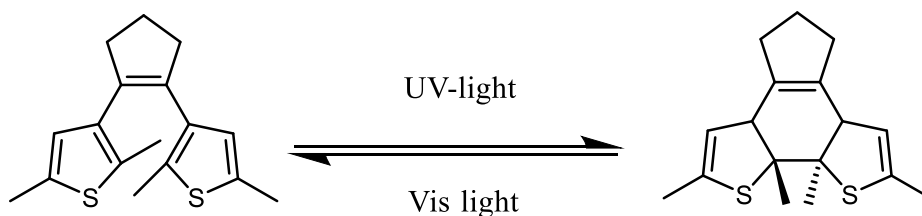


**Reaction scheme 1:** The redox process of viologen.<sup>160</sup>

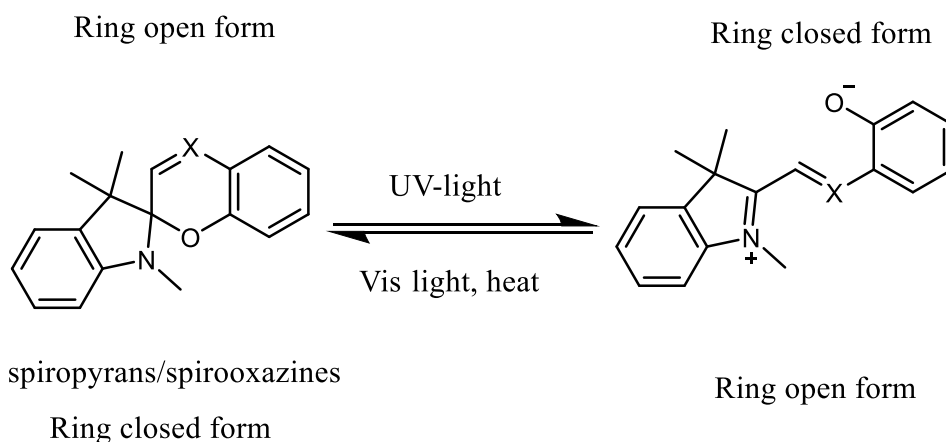
#### 1.3.2.4 chemical bond formation or cleavage

The spiropyran compounds and diarylethene(DTE)<sup>161</sup>, show bond cleavage upon illumination, as shown in the **reaction scheme 2**. Building MOFs using spiropyran, and diarylethene a photo-responsive compounds is not always successful. Due to the dramatic change in the geometry of the structure after illumination as a change from orthogonal to planar structure, while the MOFs scaffold is a rigid platform. As a result, spiropyran compounds have been loaded into MOFs /SURMOFs<sup>162,163</sup>, the compounds are in the close form, spiropyran, under visible light or high temperature. When they are illuminated using UV-light, they isomerize to the open form, merocyanines, which are conjugate compounds. The spiropyran compound has been loaded into

the pores of UiO-67 thin-film.<sup>164</sup> After successfully loading, the UV-light has been used to switch the loaded spiropyran from the closed structure, spiropyran, to open form, merocyanine. The open form, merocyanine, is a conjugated compound, which produced photoconductivity of more than one order of magnitude.



Diarylethenes/Dithienylethenes



**Reaction scheme 2:** Isomerization of diarylethenes and spiropyrans under light.<sup>108</sup>

Combination between different types of chromophoric linkers into MOFs platform afforded interesting properties, such as a remote-control  $^1\text{O}_2$  generation.<sup>165</sup> MOF called So-PCN has been built from two photochromic linkers. 1,2-Bis(2-methyl-5-(pyridin-4-yl)thiophen-3-yl)cyclopent-1-ene (BPDTE) has been used as a photoswitchable linker.<sup>166</sup> It is a very important photo-chromic linker due to its interesting properties, such as thermal stability, fast response to illumination, and fatigue resistance. The second linker has been used is porphyrin derivatives as a photosensitizer. As a result, So-PCN MOF has been obtained from the previous two photo-active linkers. Consequently, the illumination of the SO-PCN made DTE derivatives undergo photoisomerization, which led to open and close form according to the absorbed energy. This differently absorbed energy provided different pathways for the porphyrin to produce singlet oxygen  $^1\text{O}_2$ , as shown in **figure 1-20**.

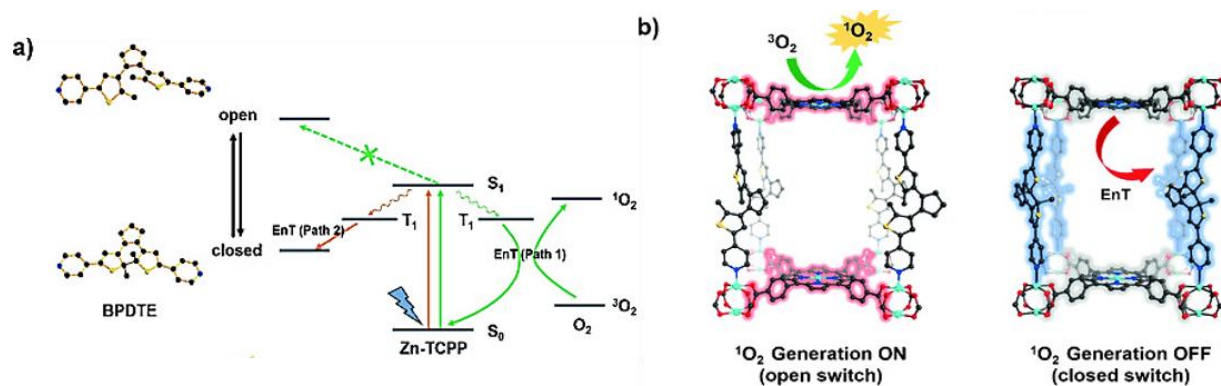
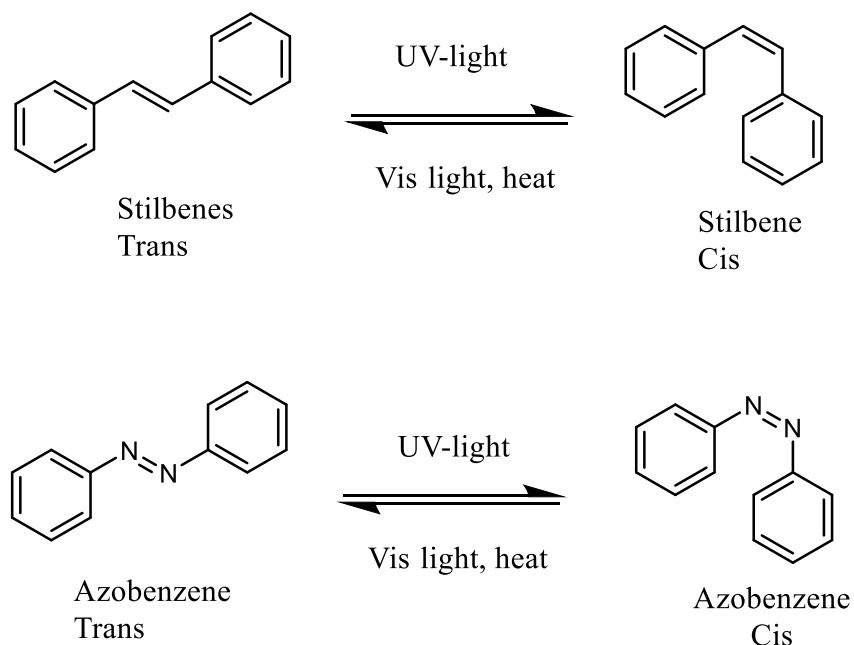


**Figure 1-19:** The proposed mechanism of the controlling single oxygen that was produced by SO-PCN MOFs, the figure was reproduced with permission from John Wiley and Sons.<sup>166</sup>

### 1.3.2.5 Reversible conformational change of the organic linker or encapsulated guest

Azobenzene, and stilbene are photoresponsive materials, which exhibit trans-cis isomerization upon illumination with a light with a suitable wavelength, as shown in **the reaction scheme 3**. Azobenzene compounds have been intensively studied in the MOFs field as a photoactive compound.<sup>167–</sup>

169



### Reaction scheme 3: The effect of light on stilbene and azobenzene

This compound has been encapsulated into bulk MOFs as well as into SURMOFs.<sup>170</sup> In one of

these studies<sup>171</sup>, azobenzene was encapsulated into different MOFs such as MOF-5, MIL-68- (In), MIL-68(Ga), MIL-68(Al) in gas-phase. The obtained azobenzene@MOF-5, azobenzene@MIL-68 (In), azobenzene@MIL-68(Ga), azobenzene@MIL-68(Al) showed trans-cis isomerization. One exception was azobenzene@MIL-68(Al), which did not exhibit isomerization. Since there was not enough free space to allow for the isomerization.

In a further experiment, the azobenzene was introduced into the pores of [Zn<sub>2</sub>(terephthalate)<sub>2</sub>-(triethylenediamine)] via mixing the MOF with molten trans-azobenzene which diffused into the pores of MOFs.<sup>172</sup> The obtained azobenzene@MOF showed trans-cis isomerization upon illumination also it was switched via heating at 120°C. Interestingly, the embedded azobenzene into MOFs showed different N<sub>2</sub> adsorption behavior depending on the isomerization form. For instance, the embedded azobenzene under the cis form showed higher N<sub>2</sub> uptake higher than the trans form. Furthermore, the azobenzene and the *o*-tetrafluoroazobenzene were infiltrated into HKUST-1 thin-film via diffusion process.<sup>170</sup> The obtained azobenzene@HKUST-1 and the *o*-tetrafluoroazobenzene@HKUST-1 were under trans-cis isomerization upon illumination with light at 365nm, and green light at 530 nm respectively. Also, they were under the reverse isomerization from cis-to trans via illumination with blue light 455nm, and violet light 400 nm respectively. Accordingly, the embedded azobenzene and *o*-tetrafluoroazobenzene into HKUST-1 thin-film revealed butanediol uptake by cis-form higher than butanediol uptake by trans-form.

The aforementioned strategies of encapsulating the azobenzene, which is called as an extrinsic method, has drawbacks either in the loading process, which does not proceed effectively, or the used MOFs have small pores size in comparison with the space required for the rotation of the photoactive molecule.<sup>171</sup> As a result, an alternative strategy has been used is called an intrinsic method.

This method showed a solution for the drawbacks of the aforementioned strategy. The intrinsic method was performed via using the photoactive compounds into the backbone of the MOFs /SURMOFs. The photoactive materials have been used as a side chain in the linkers that have been used to build MOFs/SURMOFs.<sup>108,173,174</sup> For instance, azobenzene was used as a side group in the linkers that have been used to build SURMOF/MOFs.<sup>126,173,175-178</sup> Another way was functionalization of the linkers that have been used via post synthetic modification.<sup>126,179</sup> Interestingly, the SURMOFs / MOFs that have been built using linkers have azobenzene as a side group in the backbone showed the same behavior of embedded analogies, for instance it was used as a remote

control for butanediol uptake.<sup>177,180</sup> Building MOFs/SURMOFs with photoactive materials in the backbone produces smart materials that can be used in many applications such as gas uptake remote control, conductance remote control,<sup>164</sup> and used as smart vessels.<sup>175,178,181</sup> Furthermore, a SURMOF that has been made from linker with azobenzene as a side chain attached to the backbone showed a controlled proton conduction. The SURMOF has been loaded with 1,4-butanediol and 1,2,3-triazole, and a switching between trans-cis photoisomerization showed a decrease in the proton conduction.<sup>182</sup> In addition, remote control of magnetism was afforded due to illumination of a Zr-MOF that was embedded with endohedral metallofullerenes  $\text{Sc}_3\text{C}_2@\text{C}_{80}$  and  $\text{DySc}_2\text{N}@\text{C}_{80}$  and has azobenzene as a side chain in the linker.<sup>183</sup>

## 2 Characterization methods

A plethora of techniques are used in the characterization of reticular chemistry MOFs, and also of SURMOFs.<sup>184</sup> The technique that can be applied, depends on the desired characterization.<sup>31</sup> For instance, techniques like electron microscopy (SEM and TEM) are suitable in describing the shape of the MOFs. Whereas, other techniques such as X-ray diffraction (XRD, SAXS) can help to characterize the crystallinity of the materials. In this section, I will describe the relevant methods and instruments that have been used in the characterization of SURMOFs in the present thesis, such as X-ray diffraction (XRD), ultraviolet-visible spectroscopy (UV-Vis), infrared spectroscopy (IR), scanning electron microscopy (SEM), Raman spectroscopy, fluorescence lifetime, and near-edge X-ray absorption fine structure spectroscopy (NEXAFS).

### 2.1 X-Ray Diffraction (XRD)

X-ray diffraction (XRD) is an important tool for answering different scientific questions, such as determining the crystal structure of crystalline materials, quantifying the change in the cell parameters, identifying structure phases via comparing the measured data with data from known structures, the orientation of the crystal, size of the crystal, and other structural parameters. In addition, it is a well-established and non-destructive technique. In general, it does not need special sample preparation. Different conditions can be applied during the measurement of the sample such as temperature, pressure. XRD used in the case of powder samples is called powder X-Ray diffraction (PXRD).

#### 2.1.1 Theoretical background

XRD-diffraction is a kinematic process based on a single scattering of incident X-ray photons by the outer shell electrons of atoms forming a crystalline material, which has a symmetric and periodic arrangement of atoms in three dimensions.<sup>185</sup> The distance between atoms forming layers is  $d$ , as shown in **figure 2.1**. When a monochromatic X-ray beam with a specific wavelength  $\lambda$  is directed on the sample under investigation (crystalline material) with an *angle of incidence*  $\theta$ , it alters its direction due to the scattering by the outer shell electrons of the atoms. Coherently scattered monochromatic X-rays beams from adjacent atomic layers have a difference in the path length, thus interfere constructively or destructively with each other. If their path difference  $AB + BC$  is an integral number  $n$  of the wavelength i.e.  $= n \lambda$ , then constructive interference can occur.

This condition is embraced in the Bragg equation:

Bragg's equation

$$n \lambda = 2 d \sin \theta$$

**Equation 2-1**

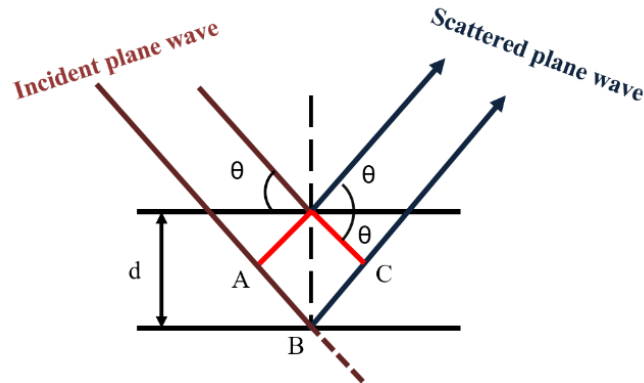


**Figure 2-1:** Schematic illustration of the constructive interference on a periodic lattice plane.

### 2.1.2 X-Ray diffractometer

X-ray diffractometers are used to measure the intensity of the diffraction of X-rays by crystalline materials. Such a device consists of three main parts: X-ray source, detector, and goniometer.<sup>186</sup> The X-ray source consists of an evacuated tube that contains a specific metal target (anode) made out of Cu, Mo, or Ni. In this evacuated tube high-velocity electrons hit the anode, which emits an electron from lower energy levels (K shell) and creates vacancies. These vacancies are filled by an electron from a higher energy level (L shell). The electron transfers from the higher energy level to the lower energy level creates a quantum of energy called X-ray photon with an energy equal to the energy difference between the two energy transition levels. These emitted photons have a wavelength in the range of 0.01-1 nm. The produced X-ray beam is directed to the sample under investigation. The *angle of incidence* ( $\omega$  in **fig. 2.2**) can be changed by the mechanical movement of the goniometer arms, as shown in **figure 2.2**. Scattered X-ray beams by the atoms of crystalline materials are directed forward and collected by the detector under the scattering angle  $2\theta$ . The read-out is used to produce the XRD diffractogram in which the intensity of the scattered beam is plotted over the scattering angle  $2\theta$ .

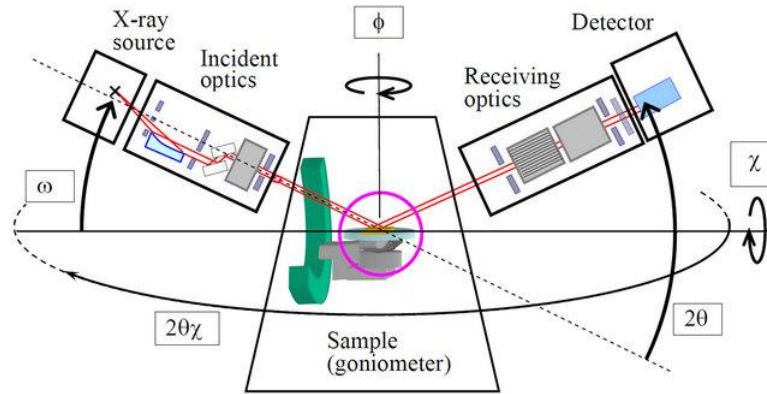


**Figure 2-2:** A schematic illustration of 5-circle goniometer system; this picture was reproduced from ref.<sup>187</sup>

### 2.1.3 X-Ray-Out-of-plane and X-Ray-in-plane

XRD diffraction is a very important tool to characterize the thin-film. The thin-films are 2-dimensional(2D) structures in many cases. In the case of conventional XRD applied to powder samples, the angle of the incident and diffracted beams has the same angle  $\theta$  and in that case, it is called symmetrical reflection measurements. In this case, the scattering vector is perpendicular to the sample surface and the measurement is called out-of-plane XRD.<sup>188</sup> Conversely, when X-ray beams incident parallel to the surface and are used to measure the perpendicular lattice planes of thin films, then the scattering vector is parallel to the surface and it is called as in-plane XRD,<sup>187,189</sup> as shown in **figure 2.3**.

To obtain an informative result from the sample under investigation by in-plane XRD, parameters must be adjusted, such as the height of the sample surface with the center of the incident X-ray beam called as Z-axis. In addition, the correct  $\phi$ -angle and the angle of incidence  $\alpha_i$  should be adjusting.

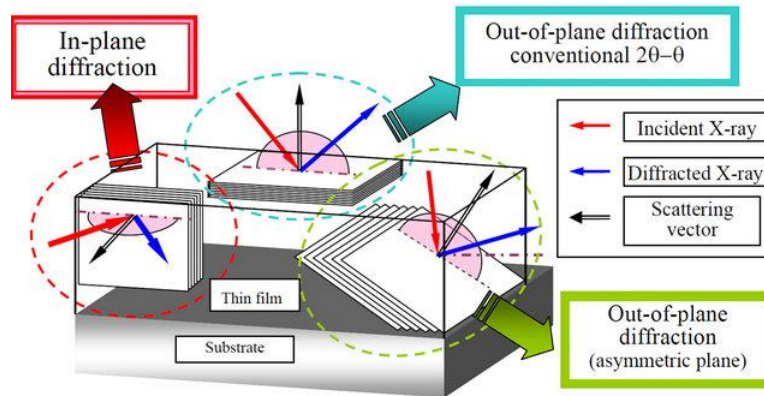


**Figure 2-3:** A schematic diagram of the geometries of thin film X-ray diffraction measurement,

showing relations between the lattice planes of a thin-film sample and different X-ray geometries: red in-plane, dark green out-of-plane, and light green grazing incident. This figure was reproduced from ref.<sup>187</sup>

In this thesis, the XRD out-of-plane measurements were carried out using a Bruker D8-Advance diffractometer equipped with a position-sensitive detector PSD Lynxeye® in Bragg-Brentano-geometry, variable divergence slit and a 2.3° Soller-slit on both sides. Also, XRD in-plane measurements were conducted on a Bruker D8 Discover in  $\theta$ -2 $\theta$  geometry which is equipped with a quarter Eulerian cradle, tilt-stage, 2.3° Soller-slits on both sides, a Göbel-mirror, and a PSD Lynxeye®. The two XRD diffractometers were operated with Cu-anodes producing Cu  $K\alpha_{1,2}$  radiations with wavelength ( $\lambda = 0.15419$  nm).

## 2.2 Infrared Spectroscopy (IR)

Infrared spectroscopy is an easy, inexpensive, and fast characterization method. It can also be used to collect information about the sample's chemically functional groups. Therefore, IR is a technique that is widely used. IR<sup>190</sup> covers a specific wavelength range between the wavelength of microwave and higher than the wavelength of visible light 700 nm– 1mm. IR radiation cannot be seen by the naked eye. IR is classified into three regions depending on the wavenumber: (i) near-infrared (NIR) in the range of 12820  $\text{cm}^{-1}$  - 4000  $\text{cm}^{-1}$ , (ii) mid-infrared (MIR) that lies in the range of 4000  $\text{cm}^{-1}$  – 400  $\text{cm}^{-1}$  and (iii) far-infrared (FIR) 400  $\text{cm}^{-1}$  - 10  $\text{cm}^{-1}$ . When IR radiation incidents on molecules that are IR active, part of IR radiation, particularly MIR and NIR, is absorbed by molecules and causes vibrational and rotational changes.<sup>191</sup>

Linear molecules consisting of  $n$  atoms have  $(2n-5)$  different vibration modes, while nonlinear molecules exhibit  $(2n-6)$  modes. There are two main types of vibration modes. Firstly, stretching vibration, which is a symmetrically or antisymmetrically rhythmical change of the interatomic distance along the bond axis. The second one is the bending vibration mode causing changes in the bonding angles. Some examples of different stretching and bending modes are shown in **figure 2-4**.<sup>192</sup>

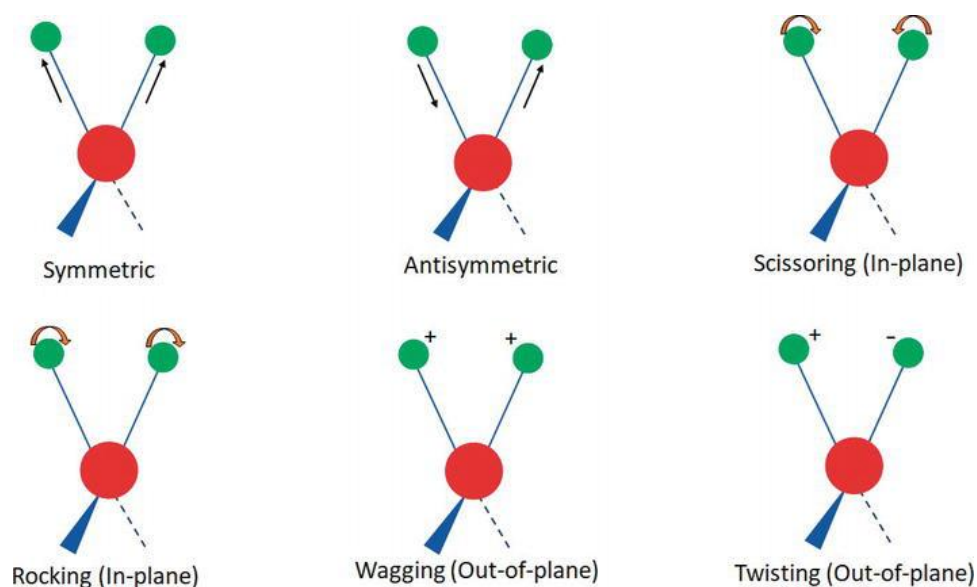


**Figure 2-4:** The vibration modes of molecules after absorption of IR radiation, showing bending modes, and stretching modes. This figure was reproduced from ref.<sup>192</sup>

In addition, there are two different types of bending vibrations: rocking and scissoring; while the out-of-plane has two vibration modes, twisting, and tagging, as shown in **figure 2-4**.

To simplify the IR effect on the bond the vibration modes activated by IR energy can be compared with the physical model of the spring system by using Hooke's law in the case of diatomic and polyatomic. let's supposed, two atoms, with different masses  $m_1$  &  $m_2$ , are connected with each other by spring of force constant  $k$ , as shown in **figure2-5**.<sup>193</sup> This model can be described as a simple harmonic oscillator.

The energy of the harmonic oscillation can be calculated using the following **equation2-2**.

$$E = 1/2. K. \Delta r \quad \text{Equation 2-2}$$

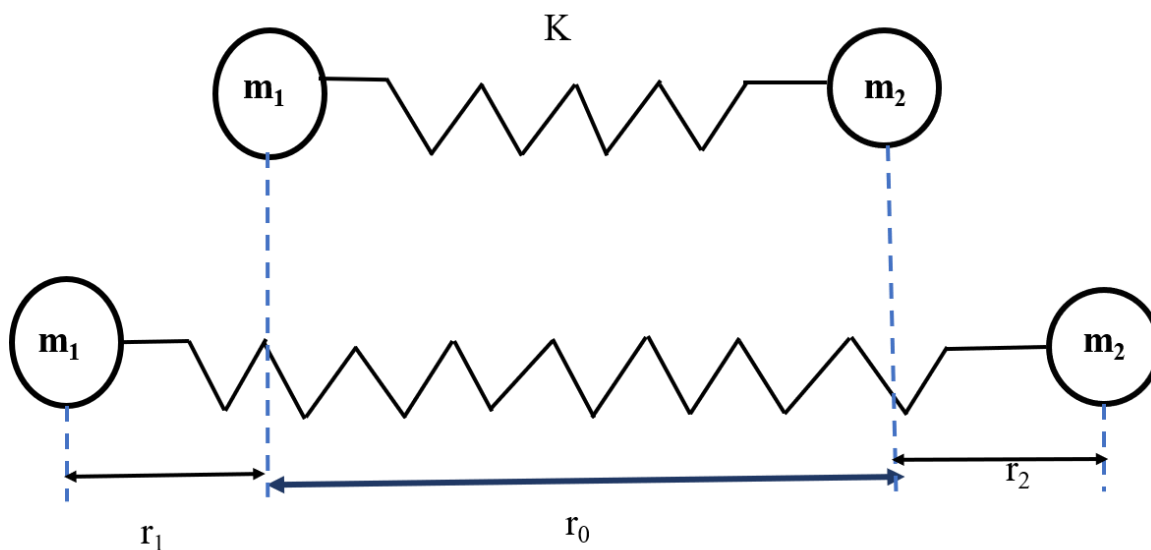


**Figure 2-5:** Schematic representation of a vibration featuring two different masses around the equilibrium distance  $r_0$ .

The frequency of the light that absorbed by the bond can be calculated from the following **equation2-3**.

$$v = 1/2\pi\sqrt{k/\mu} \quad \text{Equation 2-3}$$

Also, it can be formulated as the following **equation2-4**.

$$v' = 1/2\pi c\sqrt{k/\mu} \quad \text{Equation 2-4}$$

$v$  is the frequency of absorption, while  $v'$  is the wavenumber in  $\text{cm}^{-1}$ ;  $k$ , is the force constant of the bond;  $c$  is the light velocity; and  $\mu$  is the reduced mass, which can be calculated from the **equation 2-5**.

$$\mu = \frac{m_1 \cdot m_2}{m_1 + m_2} \quad \text{Equation 2-5}$$

The large force constant ( $k$ ) means that the bond strength increases, and leads to increases in the frequency vibration. Furthermore, a decreasing  $k$  constant represents a decrease in the bond strength, as well as a decreasing vibration frequency. The reduced mass is reverse proportional to the frequency. For instance, “ $k$  for a single bond is  $= 0.5 \cdot 10^3 \text{ N/m}$ ; double bond  $= 1 \cdot 10^3 \text{ N/m}$ , triple bond  $= 1.5 \cdot 10^3 \text{ N/m}$ .”<sup>190</sup> Therefore, the wavenumber of C=C is higher than C-C. When the same bond but with different mass of atoms, the wavenumber of the vibration mode increases with increasing the mass of the atoms e.g. C-C has a wavenumber of the vibration mode higher

than C-H bond.

Classical IR instruments are called dispersive spectrometers, which depended on splitting the light emitted by the IR light source into individual wavelengths. This separation happened by two methods, either by using an infrared prism or a grating. Due to this separation, the time required to measure one sample takes several minutes. State of the art new IR instruments are Fourier transform infrared spectroscopy (FTIR)<sup>194,195</sup>, and it is widely used nowadays. It has many advantages over the dispersive one. The first advantage is using an interferometer<sup>196</sup>, which produces a signal made up of all infrared frequencies. All of the produced IR frequencies are measured simultaneously making FT-IR a very fast method to receive a spectrum. This advantage can be used to measure several spectra successively, and the recorded data can then be processed by a CPU to produce a spectrum with increased signal-to-noise ratio. This advantage is called **Felgett Advantage**.<sup>197</sup> Due to the using of less optical components, such as slits in the monochromator over dispersive IR spectroscopy, FT-IR provide a high throughput, known as **Jacquinot Advantage**.<sup>198</sup> In addition to the mechanical simplicity, it has only movable mirrors. Finally, FTIR has an internal laser for internal wavelength calibration, which known as **Connes Advantage**. All of these advantages made FTIR highly accurate and sensitive even for impurities. It is a very fast technique that can be used to get a high-quality spectrum by repeating scans several times. As a result, IR becomes intensively used many practical applications as quantitative analysis.

### 2.2.1 Infrared Reflection Absorption Spectroscopy (IRRAS)

Infrared reflection-absorption spectroscopy (IRAS, or IRRAS) is used to study thin films. As IRRAS offers low depth information in the sample volume, it can be used to study the absorption of the upper layer including self-assembled monolayers on a reflective substrates by comparing the emitted light before and after its reflection at the surface.<sup>199,200</sup>

The incident infrared beam on the sample surface is resolved into p-polarized, and S-polarized IR light. The electric vector of p-polarized IR light is parallel to the incident plane, then it is reflected. In this thesis, the IRRAS spectra were recorded using a FTIR-infrared spectrometer (Bruker VERTEX 80). The incident angle relative to the normal surface is 80°. The mercury cadmium telluride (MCT) narrow band detector was cooled down using liquid nitrogen in the ambient conditions. Then, the spectra were collected with a resolution of 2 cm<sup>-1</sup>, and perdeuterated hexadecanethiol SAMs on Au substrates were used as background for the SURMOFs.

### 2.2.2 Attenuated Total Reflectance (ATR)

ATR can be used to collect high quality IR spectra for solids materials, liquids, and gas phase. Measuring ATR does not require complex or a long time of sample preparation.<sup>201,202</sup> It is based on the total reflectance of an incident beam through ATR crystal (reflectance between 5 to 10 times) producing evanescent waves, which provides a high sensitivity and improves the signal-to-noise ratio. In addition, the incident beam can penetrate the sample in the depth up to 2  $\mu\text{m}$ . The penetration depths depend on the angle of the incident IR beam, the crystal material and the sample under investigation. The incident beam hits the surface, where the sample under investigation, several times producing an evanescent wave. Finally, the produced wave is collecting with the detector producing an IR spectrum shown in **figure 2-6**.

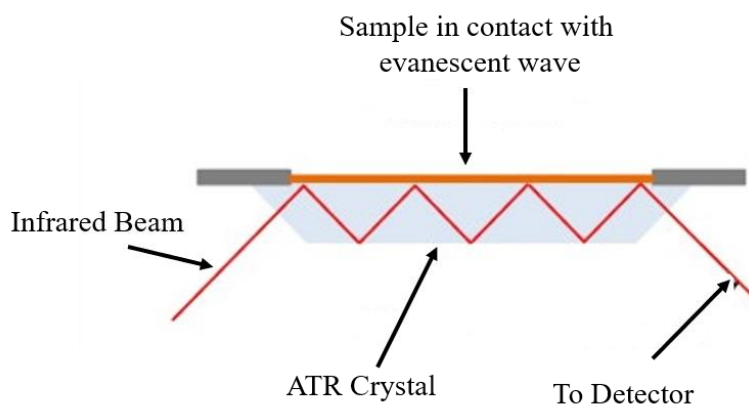


**Figure 2-6** Schematic illustration of the ATR setup.<sup>202</sup>

In this thesis, ATR measurements were conducted by Bruker Optics Tensor 27 spectrometer equipped with platinum® ATR accessory and a deuterated L-Alanine doped triglycine sulfate (LaDTGS) detector. The spectra were collected at room temperature, with a resolution of 4  $\text{cm}^{-1}$ , and air is used to collect the background.

### 2.3 Ultraviolet-Visible (UV-Vis) spectroscopy

Ultraviolet-visible spectroscopy (UV-Vis), is a simple, fast, and suitable tool for a wide range of compounds, which can be measured in transmittance /absorption or reflectance mode.<sup>203</sup> It is composed of two ranges: the ultraviolet light with wavelengths ranging from 200-400 nm and the visible light with wavelengths between 400 and 800 nm. Through using this technique, we can get information about the  $\pi$ -system of the molecules under investigation, including e.g. conjugated unsaturated, aromatic compounds, and conjugated non-bonding electron systems.

The energy of a molecule is the sum of its electronics, vibrational, and rotational energy. When a molecule absorbs UV-Vis radiation, electronic energy of the molecule changes. When the UV-Vis light is absorbed, an electron is excited and lifted energetically usually from a bonding  $\sigma$ - or a  $\pi$ -molecular orbital to the antibonding  $\sigma^*$ - or  $\pi^*$ -orbital, respectively or from a non-bonding n orbital to either a  $\sigma^*$ - or  $\pi^*$ -orbital, as shown in **figure 2.7**.

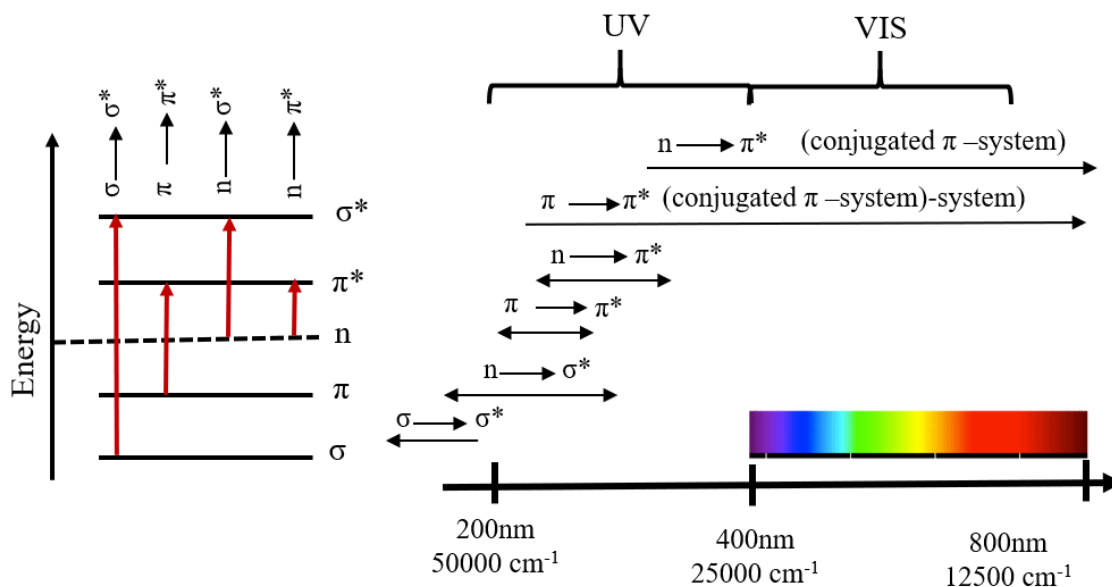


**Figure 2-7:** Electronic transitions between molecular bonding orbitals, anti-bonding orbitals and n orbitals did not involve into the molecular bond (left). Spectral regions (right), in which light is absorbed due to electronic transitions. This picture was reproduced from ref.<sup>204</sup>

The electrons of the aliphatic compound occupy the lowest occupied molecular orbital  $\sigma$ , and the energy which is required to prompt electron from  $\sigma \rightarrow \sigma^*$  is large. Because the energy is inversely proportional with the wavelength, the required wavelength for this promotion lies outside the ultraviolet range. Ultimately, molecules with different functional groups, such as (C=O), can absorb enough energy to prompt the electrons to different unoccupied energy levels. Then, the molecules show different absorption peaks. As a result, the UV-Vis spectroscopy is called electron spectroscopy.

UV-Vis absorption obeys to Beer-Lambert's law, which states that the number of molecules absorbing light of a specific wavelength is directly proportional to the intensity of the absorption spectrum as long as the molecule concentration is low enough, as in **equation 2-6**.

Therefore

$$\log (I_0/I) = \epsilon c L \quad \text{Equation 2-6}$$

$I_0$  = intensity of the incident light,  $I$  = intensity of light transmitted through the sample solution,  $c$  = concentration of the solute in mol/ l<sup>-1</sup>,  $L$  = path length of the sample in cm;  $\epsilon$  = the molar extinction coefficient of the substance is unique for every substance.

$\log(I_0/I) = A$  where  $A$  is the absorbance, the amount of the light absorbed by the solution / substance, the reverse of  $\log (I/I_0)$  is  $-\log (I_0/I) = -A = T$  with  $T$  is the transmittance, the amount of light transmitted through the solution/substance.

Lambert-Beer's law can be written as  $A = \epsilon c L$ . From this law, the amount of light absorbed or transmitted by the solution under investigation is directly proportional to the concentration of the solution and with the path length of the travelling light. Besides,  $\epsilon$  the molar extinction coefficient is constant for every substance.

In the present thesis, UV-Vis absorption spectra were collected using an Agilent Cary 5000 UV-Vis-NIR spectrophotometer, with the wavelength range 200-800 nm. The spectra were collected in transmission mode.

## 2.4 Scanning Electron Microscopy

This technique is used to investigate the morphology, crystal size, and homogeneity of SURMOFs. The eligible substance that can be investigated by SEM is the solid substrate.

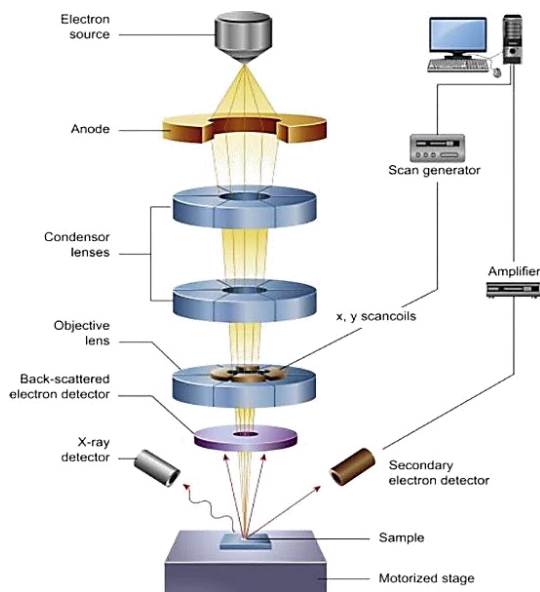


**Figure 2-8:** Schematic of a scanning electron microscope, this picture was reproduced from ref.<sup>205</sup>

SEM has a source of the electrons to produce electron beams at the top of the column called an

electron gun, as described in **figure 2-8**. The column has a combination of electron lenses and apertures to accelerate the passing electron beam. Ultimately, the electron beam hit the sample<sup>206-208</sup>, which is fixed or mounted at a stage inside the sample chamber. Before the beam hits the sample, the column and the chamber have to be evacuated using a combination of pumps. The position where the electron beam hits the sample can be controlled by scan coils.

The incident beam can penetrate the surface to a depth of 1  $\mu\text{m}$ , because the electrons are accelerating with a potential of typically 2-40 keV. This penetration depends on different factors, such as the kinetic energy of incident electrons, the incidence angle, and the atomic mass or the density of the material. The interaction of the incident beam of electrons and the mounted sample produces various radiation emissions from the atoms of the substrate including elastically scattered electrons, inelastically scattered low-energy secondary electrons, or X-rays.

The scanning electron microscopy is based on collecting secondary electrons, which expresses the morphology of the sample under investigation. The quality of SEM data /images depends on different factors, such as electron beam spot size and the interaction volume of the electron beam with the sample.

Regarding the sample preparation, SEM is working on a conductive surface, while the majority of reported MOFs/SURMOFs are insulators. To get high-quality images, the surface of MOFs or SURMOFs have to be coated with a conductive layer, such as Au or carbon layer.

In the present thesis, a Philips XL30 (FEI Co., Eindhoven, NL) SEM for the SURMOFs was used, which has a field emission gun and can be used as an environmental scanning electron microscope (FEG-ESEM). The machine is operated with acceleration potential in the range between 15 keV and 30 keV. The applied pressure is in the range of 0.7 to 1.0 Torr.

## 2.5 Near Edge-X-Ray Absorption Fine Structure (NEXAFS)

This technique is a synchrotron-based variant of photoelectron spectroscopy.<sup>209</sup> It is used to investigate atomic and electronic structures<sup>210-212</sup>, and molecular orientations.<sup>213,214</sup> It works as incident photons, with sufficient energy, hit the sample under investigation. Those photons excite a bound electron e.g., a core electron or from an inner shell in an unoccupied level. This empty core level is unstable and has a short lifetime in the range of femtosecond. Therefore, it is filled with another electron from a higher energy state and is accompanied with release of energy. This energy is released in the form of radiation in a way of the emission of fluorescence or by non-radiative kind as emission of an Auger electron, as described in **figure 2-9**. It shows different core

levels, which have different binding energies. The binding energy is distinct to each element.

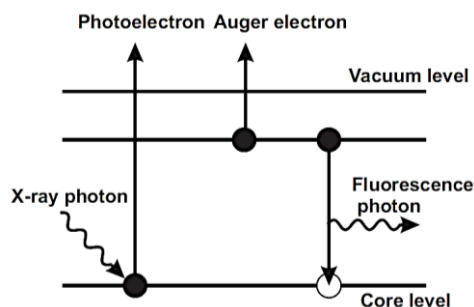


**Figure 2-9:** The photo-absorption process including filling of the core hole by emission of a photon or an Auger electron. This picture was taken from ref.<sup>215</sup>

This technique has some importance when applied to light elements, such as Carbon, Nitrogen, and Oxygen. These elements have intensive absorption in the soft X-ray region (100 –700 eV). As a result, organic compounds are suitable probes to be investigated by this technique.<sup>216</sup> Absorption of the soft X-ray causes transition of electrons from the K-edge, the deepest core shell, into unoccupied molecular orbitals.

NEXAFS has many advantages superior to other characteristics techniques. One of these advantages is the highly sensitivity to chemical nature of intramolecular bonds. This technique is suitable to different between (C-C) and (C=C), which can be detected easily in comparing with using XPS. Because the difference in the binding energy between  $\pi^*$  and  $\sigma^*$  that can be detected using XPS, lies in the range of 0.1eV. While the binding energy difference between them that can be detected using NEXAFS lies in the range of several electron volts.

X-ray beam produced in the NEXAFS device travels through vertical and horizontal slits. To monitor the intensity of the X-ray beam, it must pass through a gold grid, which transmit 85%. The predefined X-ray beam hits the sample under investigation inside the sample chamber, which can be aligned to the specific spot. The alignment of the sample under investigation help to prevent the incident X-ray to illuminate the sample holder.

The X-rays that absorbed by a cross-section of the sample can be measured by two methods. The first method is using an X-ray sensitive detector to measure the beam of X-ray that transmitted by the sample under investigation. Due to the lack of the surface sensitivity, this method is suitable for thin-films that have a thickness between  $\mu\text{m}$ -mm. The second method is measuring the secondary electrons produce from the decay of the core hole that emitted from the sample into the vacuum. Later method is the most commonly used method nowadays. Because it was designed to

overcome the sensitivity of the prior method. **Figure 2-10** shows the scheme of the NEXAFS experimental setup.

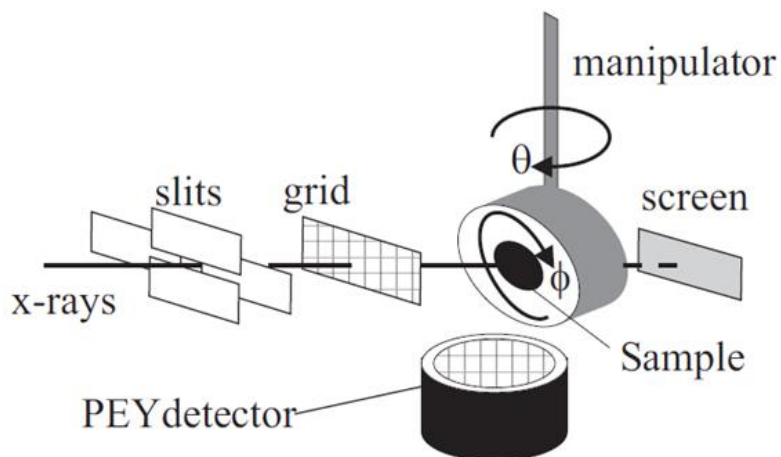


**Figure 2-10:** The scheme of the NEXAFS experimental setup. This picture was reproduced from ref.<sup>215</sup>

In this thesis, The NEXAFS measurements were conducted using the dipole beamline HE-SGM of the synchrotron storage ring BESSY II in Berlin (Germany).<sup>213</sup> NEXAFS measurements were carried out with linearly polarized radiation (polarization factor  $P \approx 82\%$ ) with an energy resolution of better than 350 meV which were recorded at the C K-edge in the partial electron yield mode with a retarding voltage of  $-150$  V at the C K-edge. In the partial electron yield mode, retarding potentials are applied to assure that only near-surface electrons are detected. The NEXAFS raw data were normalized in a multi-step procedure by considering the incident photon flux which was monitored by the photocurrent on the gold grid and using the background signal of the clean Au substrate.

## 3 Materials and experiments

### 3.1 Chemicals

Methyl-4-ethynylbenzoate (sigma Aldrich), dimethylsulfoxide-d6 (99.9 atom, sigma Aldrich), bis-(triphenylphosphine) palladium (II)chloride (sigma Aldrich), 9,10-dibromoanthracene (Alfa Aesar), Tri-(p-tolyl)-phosphine (98%, across organics), tris(dibenzylideneacetone)dipalladium (0) (sigma Aldrich), 4-Methoxycarbonylbenzeneboronic acid (95%) (sigma Aldrich) were used as purchased without further purification. Ethyl acetate, dichloromethane, potassium hydroxide, and potassium tribasic phosphate, zinc acetate dihydrate, copper acetate monohydrate, and n-hexane were purchased from Merck Millipore and they were used without further purification. 16-Mercaptohexadecanoic acid (MHDA, 97%), 11-mercapto-1-undecanol (MUD), and absolute ethanol were purchased from VWR (Germany) and they were used without further purification.

### 3.2 Substrates

Gold substrates were obtained from Georg Albert-Physical Vapor Deposition (Silz, Germany). The silicon substrates were coated with a gold layer on the surface with a thickness of 100nm. Furthermore, 5 nm of titanium layer was deposited between Si and 100 nm gold layers to improve the adhesion. The silicon substrates (Si) with [100] orientation were obtained from Silicon Sense (US). The quartz glass substrates were purchased from GVB Solutions in Glass (Herzogenrath, Germany). These substrates were sonicated in acetone and ethanol for 5min, and 10 min respectively, and finally were dried in a flux of N<sub>2</sub>.

### 3.3 Preparation of the substrates.

As mentioned in **the introduction**, the functionalization of the substrate is a crucial step in the preparation of homogenous, orientated thin-films, reproducible, as well as, afford the desired SURMOFs to fulfill the desired applications.

### 3.4 Functionalization of silicon substrates

The Si-substrates were sonicated in acetone and ethanol for 5 min and 10 mins respectively, followed by rinsing with pure ethanol and drying with N<sub>2</sub> flux. The functionalization of Si-substrates is required to increase the number of reactive –OH groups on the surface and to remove organic residues from the surface. This functionalization can be performed using UV/ozone cleaner or O<sub>2</sub> plasma cleaner. Functionalization using UV/ozone cleaner was done for 30 minutes (UV Ozone Cleaner ProCleaner, BioForce Nanosciences, Salt Lake City, USA; or UV Ozone Cleaner,

Ossila, Sheffield, United Kingdom). The substrates can also be functionalized using an O<sub>2</sub> plasma cleaner (Nano low-pressure plasma system, Diener electronics, Ebhausen, Germany) at an oxygen flow of 50 sccm and vacuum pressure of 0.5 mbar for 30 mins. Thereafter, the substrates were kept in an ethanol solution of the metal sources which used in the synthesis of the SURMOFs. The pre-functionalized substrates were used immediately to avoid the formation of metal rods on the surface. The Si-substrates were coated with Zn-bianthryl to conduct Raman measurement, and SEM. Furthermore, the Si-substrates were coated with Zn-viologen based SURMOF to conduct the XPS measurement.

### **3.5 Functionalization of quartz glass substrates**

Quartz glass substrates were cleaned using the same procedure as described above for the Si-substrates namely sonicating first in acetone, and pure ethanol for 5 mins, and 10 mins respectively. Then, they were rinsed with pure ethanol and dried in a flux of N<sub>2</sub>.

### **3.6 Preparation of SAMs**

#### **3.6.1 Preparation of MHDA SAMs on gold substrate**

After the gold substrates were cleaned with ethanol and acetone and dried with N<sub>2</sub> flux, they were immersed in a 0.02 mM 16-Mercaptohexadecaonic acid (MHDA) solution (5% acetic acid, 95% ethanol).<sup>217</sup> Then, they were kept in dark at room temperature for 72 h. Thereafter, the Au-substrates were removed from the solution, rinsed with pure ethanol and dried with N<sub>2</sub> flux. to get MHDA SAMs. The samples were used immediately to fabricate SURMOFs.

#### **3.6.2 Preparation of MUD SAMs on gold substrate**

The Au-substrates were cleaned with pure ethanol and acetone and dried in an N<sub>2</sub> flux. Then, they were immersed in a 1 mM ethanolic solution of 11-Mercapto-1-undecanol (MUD). After that, they were kept in the dark at room temperature for 24 h. Then, the samples were removed and cleaned with pure ethanol, and gently dried in an N<sub>2</sub> flux to get MUD SAMs. They were used immediately to grow SURMOF. The Au-substrates that were treated with the SAMs, MUD and MHDA, were freshly prepared prior to SURMOF deposition to prevent decomposition of SAM.

### **3.7 Synthesis of Zn-bianthryl-based SURMOF using spin coating**

Zn-bianthryl based SURMOF was prepared by layer-by-layer liquid phase epitaxy (LPE) using the so-called spin coating approach.<sup>81</sup> The functionalized substrates (pre-cleaned quartz, Si/SiO<sub>2</sub>, and

MUD functionalized Au) were placed on the vacuum chuck and subjected to spin coating. The ethanol solution of zinc acetate dihydrate; metal nodes (1 mM, 0.5 ml), was deposited for 10 s at a speed 1000 rpm, followed by deposition ethanol solution of the bianthryl; linker (0.05 mM, 0.5 ml). The deposition of the ethanol solution of the zinc acetate dihydrate and ethanol solution of bianthryl were separated by rinsing step with pure ethanol (0.7 ml) to remove uncoordinated metal nodes or linkers, and the side products. This deposition cycle was repeated for 50, 75, 100, 200 times to get the desired thickness. Finally, the grown films were thoroughly rinsed with ethanol and dried under aN<sub>2</sub> flow. All the Zn-bianthryl based SURMOF samples were kept in the dark until the desired measurement was conducted.

### **3.8 Preparation of Zn-bianthryl based SURMOF (pristine)spray method.**

Zn-bianthryl based SURMOFs were also prepared by using the spray method as described in **chapter 1.2.2.2.**<sup>80</sup> The functionalized substrates (precleaned quartz glass substrates, Si/SiO<sub>2</sub>, or MUD-Au) were fixed on the sample holder. Then, ethanol solution of zinc acetate dihydrate 1 mM, was sprayed for 15 s, followed by spraying with 0.05 mM of an ethanolic solution of bianthryl for 25 s. The previous depositions of the metal solution and linker solution were separated by an intermediate rinsing step using pure ethanol to remove the unreacted precursors and the side products. For spraying N<sub>2</sub> gas were used at a pressure of 0.2 mbar). This deposition cycles were repeated until the desired thickness was obtained. Finally, the grown films were thoroughly rinsed with ethanol and dried under N<sub>2</sub> flow. All the Zn-bianthryl based SURMOF were kept in dark after direct preparation until the desired measurement was conducted.

### **3.9 Preparation of irradiated Zn-bianthryl based SURMOF**

Zn-bianthryl based SURMOFs were irradiated with an UV-lamp emitting light with a wavelength of 365 nm in an ambient condition for 6 h. For comparison, the sample was irradiated in an inert atmosphere (N<sub>2</sub>), which was kept inside the round bottom flask connected with the *Schlenk line*. Then, it was evacuated under pressure and flashed with N<sub>2</sub>. This process was repeated several times to get rid of any traces of O<sub>2</sub>. The sample was irradiated with the UV-lamp for the same duration of time. These samples were used for further characterization such as Raman, UV-Vis, IRRAS, and NEXAFS measurements.

### **3.10 Preparation of Zn-viologen based SURMOF (pristine)**

Zn-viologen-based SURMOFs were prepared by using the spray method, as described in **chapter**

**1.2.2.2.**<sup>80</sup> The functionalized substrates (precleaned quartz glass substrate, Si/SiO<sub>2</sub>, or MUD-Au) were fixed on the sample holder. Then, ethanol solution of zinc acetate dihydrate 1 mM, was sprayed for 15 s, followed by spraying 0.05 mM of ethanol solution of viologen for 25 s. The previous deposition was separated with an intermediate rinsing step for 5s with pure ethanol to remove the uncoordinated precursors and the side products. The pressure (0.2 mbar) and N<sub>2</sub> were used. With repeating the previous steps for 30, 45, and 60 times, the desired thickness was obtained. The growth films were rinsed thoroughly with pure ethanol and dried under N<sub>2</sub> flow. All Zn-viologen-based SURMOF samples were prepared and kept in the dark until the desired measurement was conducted.

### **3.11 Irradiation of the Zn-viologen based SURMOF.**

Zn-viologen based SURMOFs were irradiated under ambient conditions with an UV-lamp emitting light with a wavelength of 365 nm. To study the effect of the ambient conditions, Zn-viologen based SURMOF samples were put in a round bottom flask that connected with the *Schlenk line*, then was evacuated. Thereafter, Ar gas was flashed the round bottom flask and evacuated again. The previous steps were repeated several times to get rid of O<sub>2</sub> traces. Finally, the sample was irradiated for 1.5 h by light with UV-lamp emitting light with a wavelength of 365 nm under flowing of Ar gas.

### **3.12 Electron paramagnetic resonance (EPR) measurements:**

Zn-viologen-based SURMOF samples grown on Au-substrates were placed inside the EPR tube. The EPR signal was collected for the pristine sample in the dark. Then, the sample was illuminated under ambient conditions with a light of a wavelength 600 nm, (in situ illumination). For comparison, the data was also collected under Ar, an inert condition), in which the sample was inserted in the EPR tube, evacuated and sealed inside the glovebox. Then, the EPR signal was collected for the pristine sample in the dark. Followed by illuminating the sample in situ and EPR signals were collected within the time.

### **3.13 Quartz crystal microbalance**

A Q-Sense E4 Auto4 device was used in connection with a Q-Sense QCM sensor, diameter 14 mm, thickness 0.3 mm, AT cut, and a fundamental frequency 4.95 MHz. The Zn-viologen-based SURMOF was grown on the Au coated QCM sensor and prepared using the lbl-spray method as described in **chapter 1.2.2.2.**<sup>80</sup> The samples were activated in a N<sub>2</sub> gas flow at 30 °C overnight.

The temperature and the N<sub>2</sub> flow rate were kept constant during the experiment at 30 °C and at 100 ml min<sup>-1</sup> using a mass flow controller, respectively. For the aniline adsorption, the N<sub>2</sub> gas flow was enriched with aniline by bubbling through a bottle filled with 10 ml aniline. The aniline-enriched gas flow streamed through the QCM cell with the SURMOF sample. For desorption, the gas flow was switched back to pure N<sub>2</sub> gas.

### 3.14 Electrical conductivity

For the measurements of the electronic conductivity and the photoconductivity, the SURMOF films are synthesized on glass substrates with pre-deposited interdigitated gold electrodes (IDE). The IDE-glass substrates were obtained from DropSens. The gap width is 10 μm, as shown in **figure 3.1**. The total length of the gap between the gold electrodes amounted to 1.69 m (= 2 times 125 gaps of 6.76 mm length). Prior to SURMOF synthesis, substrate functionalization was carried out by UV-ozone treatment for 30 min to remove impurities as well as to increase the number of surface-OH functional groups. Before the measurements, the sample was activated at 50°C for 30 min, to remove residual water. The electrical conductivity of the sample in a pure nitrogen atmosphere was measured with a Keithley 2635B source meter. The DC voltage was kept constant at 1 V. The light irradiation was performed with LEDs from PrizMatix with emission maxima at 365 nm and 455 nm, and power densities of approximately 140 mW cm<sup>-2</sup>, and 127 mW cm<sup>-2</sup>, respectively. More details for the setup can be found in ref. <sup>164</sup>

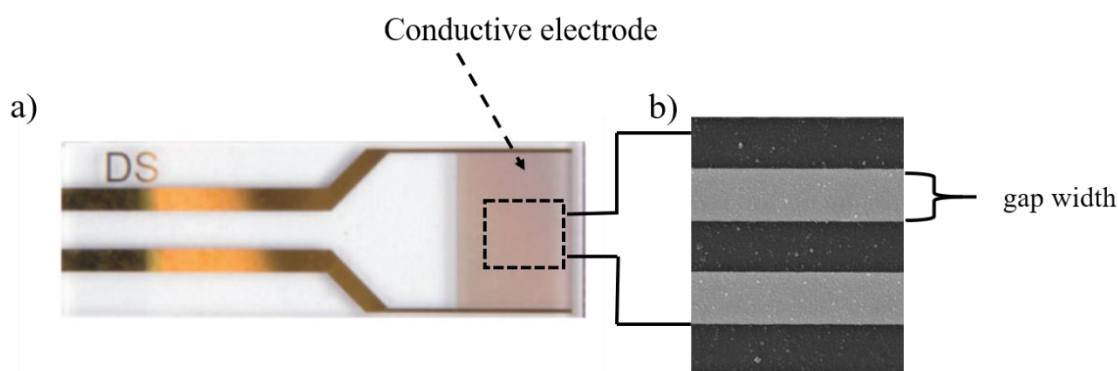
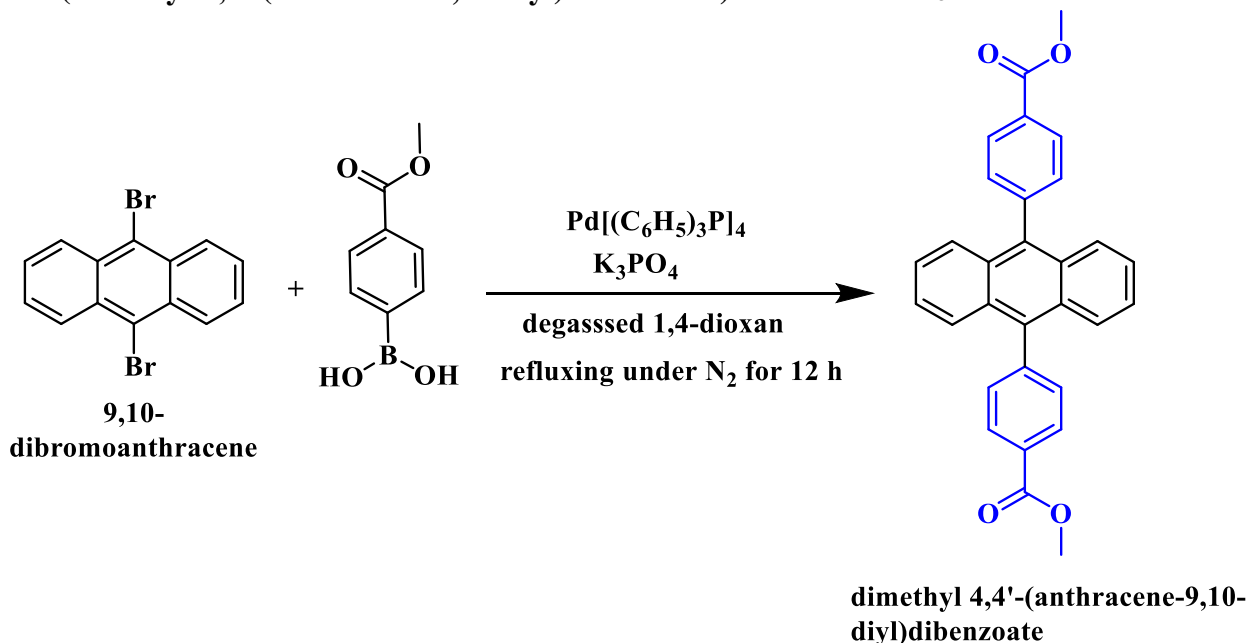


**Figure 3-1:** a) The IDE-glass substrates; b) The gap width is 10 μm of the electrode used. This picture was reproduced with modification from ref. <sup>218</sup>

### 3.15 Synthesis of the organic linkers

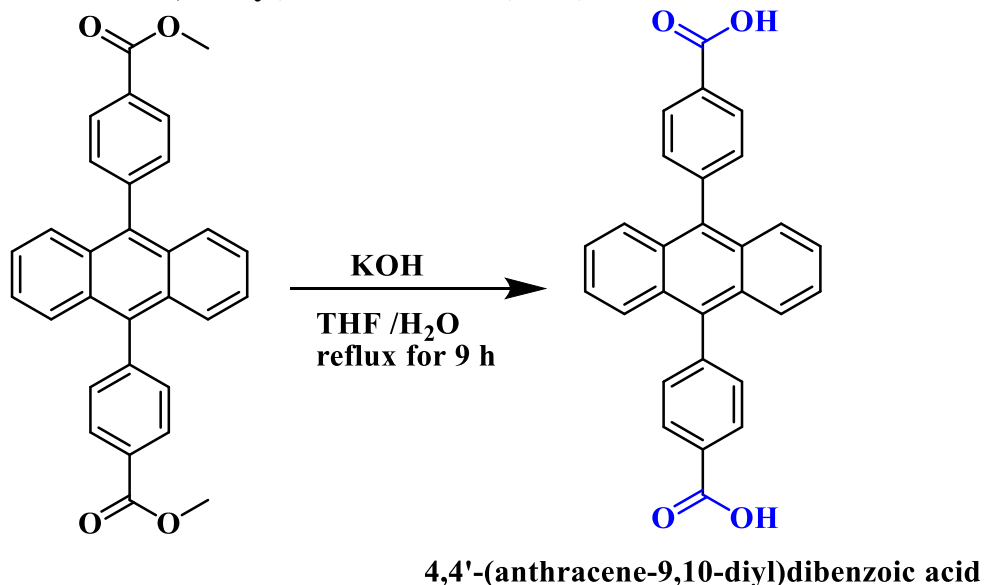
#### 3.15.1 (dimethyl-4,4'-(anthracene-9,10-diyl) dibenzoate) ADB-COOCH<sub>3</sub>



#### Reaction scheme 3-1: Synthesis of ADB-COOCH<sub>3</sub>

The compound was prepared according to ref.<sup>219</sup> In 50 ml a round bottom flask, 9,10-dibromoanthracene (2.0 g, 8.47 mmol), 4-(methoxycarbonyl) phenylboronic acid (3.24 g, 18 mmol), tetrakis(triphenylphosphine) palladium (0) (0.49 g, 0.42 mmol), and potassium tribasic phosphate (5.39 g, 25.41 mmol) were mixed and dissolved in 200 ml of degassed 1,4-dioxane. The reaction mixture was heated to reflux under N<sub>2</sub> for 12 h. The reaction was followed by TLC. Then, the reaction mixture was cooled down and the solvents were removed under rotary evaporator. The mixture was washed with water and extracted with ethyl acetate. The separated organic layers were concentrated by removing the solvents and applied to column chromatography using hexane: ethyl acetate (9:2) as eluting. The target compound was obtained as a faint yellow powder with a yield of 85%. <sup>1</sup>H NMR (400 MHz, CDCl<sub>3</sub>) δ 8.23 (d, *J* = 8.3 Hz, 2H), 7.57 – 7.53 (m, 2H), 7.51 (d, *J* = 8.2 Hz, 2H), 7.30 – 7.26 (m, 2H), 6.54 – 6.41 (m, 2H), 6.40 (dd, *J* = 132.2, 66.8, 29.9 Hz, 2H), 3.95 (s, 3H) ppm.

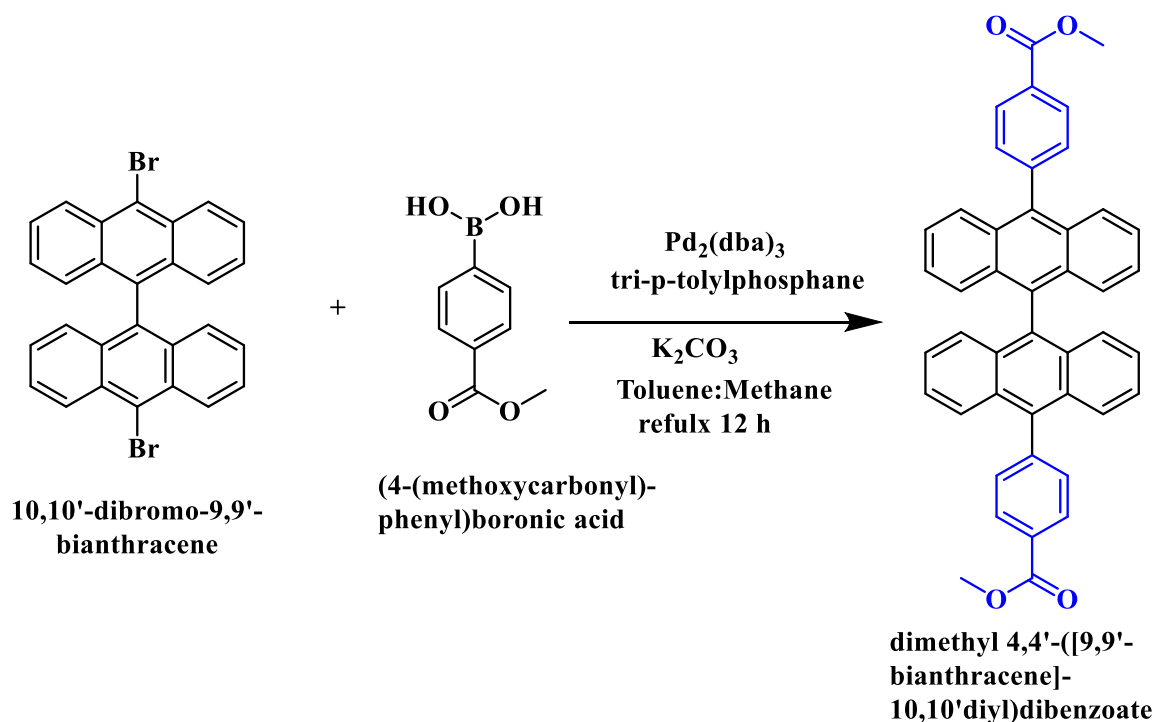
### 3.15.2 4,4'-(anthracene-9,10-diyl) dibenzoic acid (ADB).



#### Reaction scheme 3-2: Synthesis of ADB linker

In 250ml a round bottom flask, dimethyl-4,4'-(anthracene-9,10-diyl) dibenzoate (2 g, 4.5 mmol) was dissolved in 15 ml of tetrahydrofuran, and 3 ml of water dissolved KOH (0.6 gm, 11 mmol) was added. Then, the reaction was refluxed with stirring for 9 h. The reaction mixture was concentrated by rotary evaporator, followed by dissolving the product in water and neutralizing with hydrochloride acid (4 ml, 0.1 N). The precipitate was filtered off and extracted from ethyl acetate three times. It dried under vacuum to obtain a faint yellow powder with a yield of 95%. <sup>1</sup>HNMR, (400MHz, DMSO-d<sub>6</sub>) δ 13.15 (s, 1H), 8.23 (d, *J* = 8.1 Hz, 2H), 8.23 (d, *J* = 8.1 Hz, 2H), 7.62 (d, *J* = 8.1 Hz, 2H), 7.56 (dd, *J* = 6.8, 3.3 Hz, 2H), 7.46 (dd, *J* = 6.9, 3.3 Hz, 2H); and <sup>13</sup>CNMR, (400 MHz, DMSO-d<sub>6</sub>) δ 167.69, 143.33, 136.46, 131.77, 130.81, 130.11, 129.34, 126.67, 126.39 ppm.

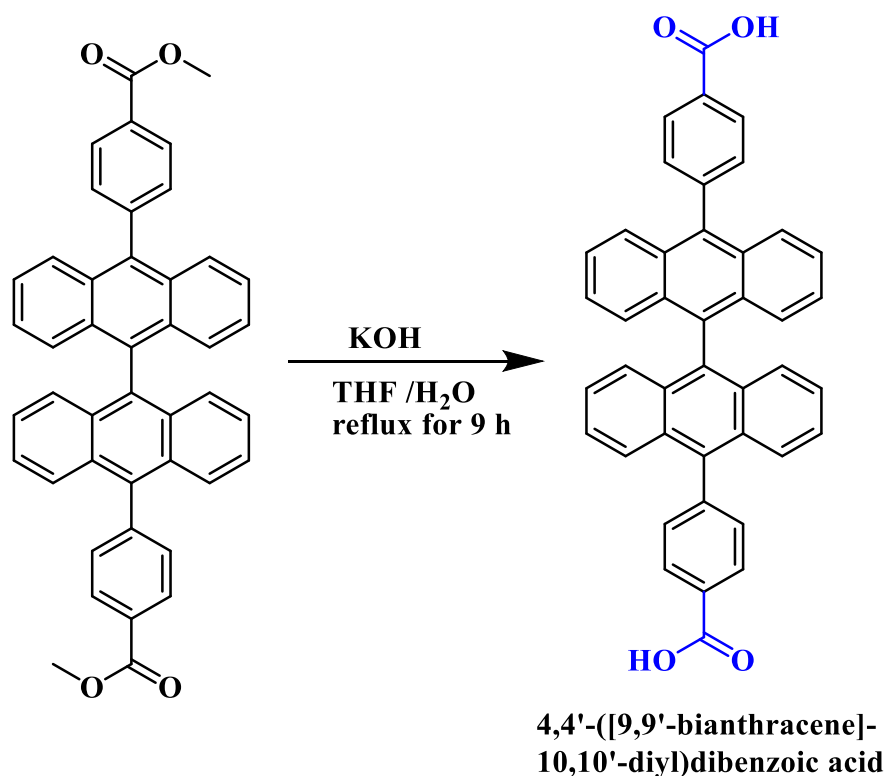
### 3.15.3 Dimethyl 4,4'-([9,9'-bianthracene]-10,10'-diyl) dibenzoate (bianthrylCOOCH<sub>3</sub>).



#### Reaction scheme 3-3: Synthesis of bianthryl -COOCH<sub>3</sub>

The compound was prepared according to ref. <sup>220</sup> In 50 ml a round bottom flask, 9,10-dibromoanthracene A (0.3 g, 5.85 mmol), (4-(1-methoxyvinyl) phenyl) boronic acid (0.26 g, 1.45 mmol), tetrakis(triphenylphosphine) palladium (0) (0.034g, 0.029 mmol), anhydrous potassium carbonate (0.37 g, 2.6 mmol), and *p*-tolylphosphine (0.036g, 0.12 mmol) were mixed up. The solids were evacuated under vacuum pressure to get rid of any O<sub>2</sub> traces. Then, 200 ml of degassed toluene and methane (6:4) were injected into the reaction mixture. Thereafter, the reaction mixture was heated to reflux under N<sub>2</sub> for 12 h. The reaction was followed by TLC. The reaction mixture was cooled down and the solvents were removed under rotary evaporator. The mixture was washed with water and extracted with dichloromethane. The compound was applied to column chromatography using hexane: ethyl acetate (9:2) as eluent solvents. The desired compound was obtained as faint yellow powder with a yield of 0.33gm, 90% and was confirmed by <sup>1</sup>HNMR, (400 MHz, DMSO-d<sub>6</sub>)  $\delta$  4.00 (s, 3H), 7.10 (d,  $J = 8.8$  Hz, 2H), 7.30 (t,  $J = 7.6$  Hz, 2H), 7.62 – 7.43 (m, 2H), 7.69 (d,  $J = 8.8$  Hz, 2H), 7.84 (d,  $J = 7.1$  Hz, 2H), 8.33 (d,  $J = 7.0$  Hz, 2H), and <sup>13</sup>CNMR, (400MHz, CDCl<sub>3</sub>), 52.31, 125.68 (d,  $J = 9.2$  Hz), 126.80, 127.13, 129.77 (d,  $J = 6.3$  Hz), 131.28, 131.67, 133.84, 136.47, 144.23, 167.13 ppm.

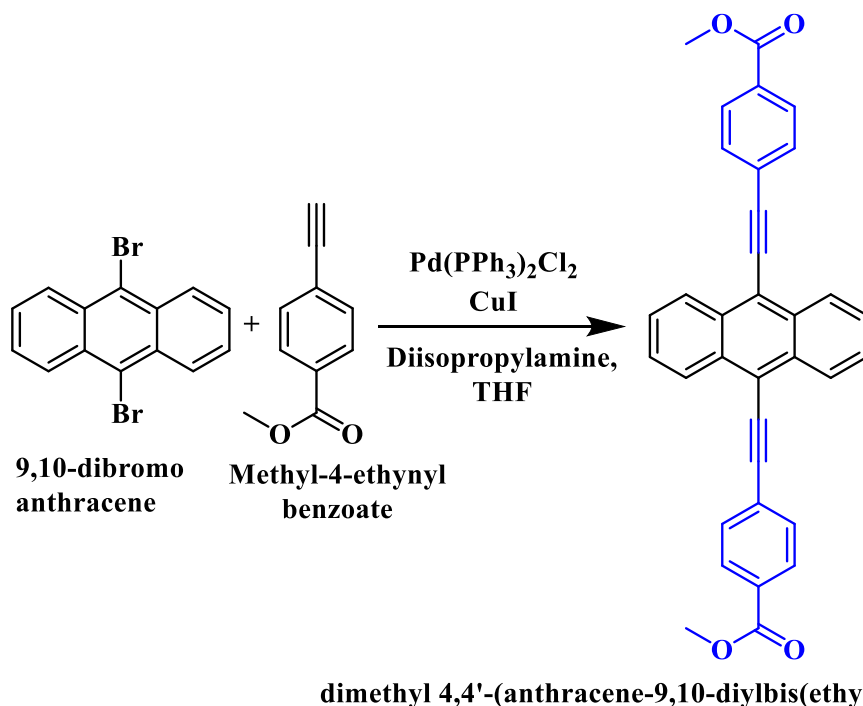
### 3.15.4 - 4,4'-([9,9'-bianthracene]-10,10'-diyl) dibenzoic acid (bianthryl).



#### Reaction scheme 3-4: Synthesis of bianthryl

In 250 ml a round bottom flask, the (bianthrylCOOCH<sub>3</sub>) compound (0.3 g, 0.48 mmol) was dissolved in tetrahydrofuran, and KOH (0.056 g, 1 mmol) in 3 ml of water added to the mixture. The reaction was refluxed for 36 h under N<sub>2</sub> gas. After completion, the solvent was removed by rotary evaporator, followed by dissolving the product in water and neutralizing with hydrochloride acid (4 ml, 0.1 N). Then the product was precipitated and washed several times with water to obtain highly pure compound with a yield of 98% as faint yellow color. The product was confirmed using <sup>1</sup>HNMR, (400 MHz, DMSO-d<sub>6</sub>) δ 13.17 (s, 2H), 8.30 (d, *J* = 7.8 Hz, 4H), 7.79 (d, *J* = 7.7 Hz, 4H), 7.69 (d, *J* = 8.8 Hz, 4H), 7.45 (d, *J* = 14.9 Hz, 4H), 7.29 (d, *J* = 14.9 Hz, 4H), 7.09 (d, *J* = 8.7 Hz, 4H); and <sup>13</sup>CNMR, (400, DMSO-D<sub>6</sub>) 126.51 (s), 127.78 – 126.68 (m), 129.66(s), 130.15 (s), 131.25 – 131.20 (m), 131.25 – 131.20 (m), 131.97 (s), 133.39 (s), 137.10 (s), 143.46 (s), 167.99 – 167.79 (m)ppm.

### 3.15.5 - Dimethyl-4,4'-(anthracene-9,10-diylbis(ethyne-2,1-diyl)) dibenzoate (C-C ADB-CH<sub>3</sub>)

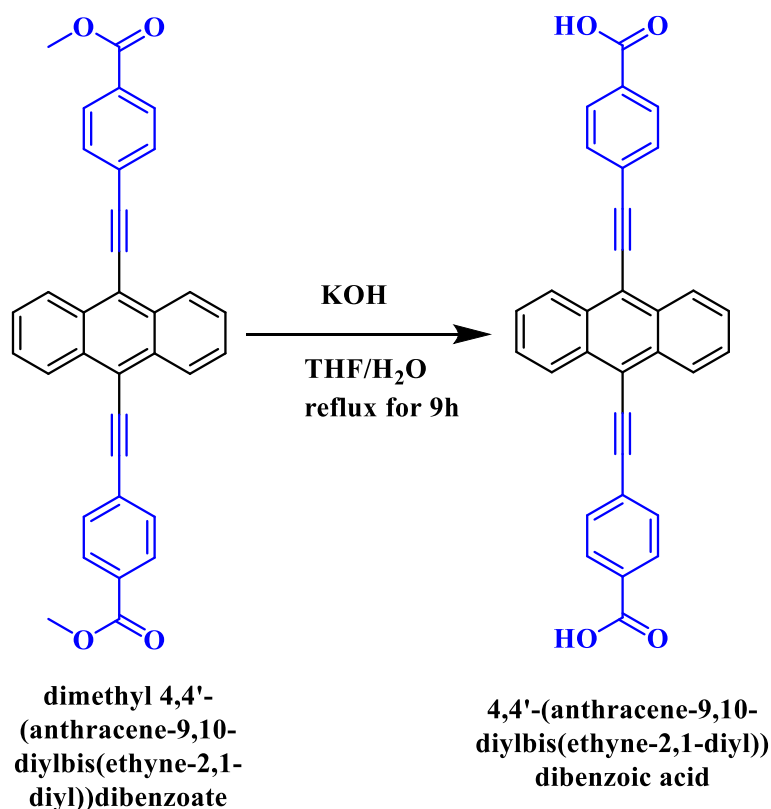


dimethyl 4,4'-(anthracene-9,10-diylbis(ethyne-2,1-diyl))dibenzoate

#### Reaction scheme 3-5: Synthesis of CCADBCOOCH<sub>3</sub>

The compound was prepared according to ref <sup>221</sup> using Sonogashira coupling reaction, In 50 ml a round bottom flask, 9,10-dibromoanthracene (0.524 g, 1.56 mmol), Pd(PPh<sub>3</sub>)<sub>2</sub>Cl<sub>2</sub> (0.0328g, 0.045 mmol, 3%), and CuI (0.01485 g, 4%, 0.08 mmol ). The solid mixture was evacuated under vacuum for 3 h, followed by injection the degassed tetrahydrofuran to the solid mixture. Methyl 4-ethynylbenzoate (0.50 g, 3.12 mmol) was dissolved in THF and added dropwise in range one hour and 0.5ml of diisopropylamine was added. The reaction was left for stirring at RT for half hour followed by refluxing at 80°C overnight. The reaction was followed by TLC. Then, the reaction mixture was concentrated by removing the solvents using rotary evaporator. The reaction mixture was dissolved in ethyl acetate and water. Then, the organic layer was separated by a separation funnel. The precipitated was applied to column chromatography using hexane: ethyl acetate (10:1) as eluent solvents. The desired compound was obtained as red-orange powder with a yield of 60%. <sup>1</sup>H NMR (400 MHz, CDCl<sub>3</sub>) δ 8.62 (dd, *J* = 6.6, 3.2 Hz, 2H), 8.07 (d, *J* = 8.1 Hz, 2H), 7.77 (d, *J* = 8.1 Hz, 2H), 7.62 (dd, *J* = 6.6, 3.2 Hz, 2H), 3.91 (s, 3H); and <sup>13</sup>C NMR (101 MHz, CDCl<sub>3</sub>) δ 132.58, 132.11, 131.60 (s), 129.76 (t, *J* = 16.5 Hz), 127.19 (s, 3H), 127.94, 118.40, 101.84, 89.32, 52.32 (s, CH<sub>3</sub>) ppm.

### 3.15.6 4,4'-(Anthracene-9,10-diylbis(ethyne-2,1-diyl)) dibenzoic acid (C-C ADB).



#### Reaction scheme 3-6: Synthesis of CCADB

In 250ml a round bottom flask, the previous compound (0.40 g, 0.80 mmol) was dissolved in tetrahydrofuran and water. KOH (0.12 g, 2 mmol) in 3 ml of water was added. The reaction was refluxed for 9 h at 110 °C under N<sub>2</sub> gas flow. The reaction mixture was concentrated by removing the solvent. The product was dissolved in water and neutralized with hydrochloride (0.1N, 4 ml). The precipitated was filtrated off and washed with ethyl acetate and water. The product was dried under vacuum to orange powder with a yield of 90% and was confirmed using, <sup>1</sup>H NMR (400 MHz, DMSO) δ 13.26 (s, 1H), 8.73 (dd, *J* = 6.6, 3.2 Hz, 2H), 8.09 (d, *J* = 8.2 Hz, 2H), 8.03 (d, *J* = 8.1 Hz, 2H), 7.84 (dd, *J* = 6.6, 3.1 Hz, 2H); and <sup>13</sup>C NMR (101 MHz, DMSO) δ 167.19, 132.35, 131.91, 131.51, 130.18, 128.55, 127.28, 126.86, 118.04, 102.65, 88.75 ppm.

## 4 Results:

### 4.1 Self-Photosensitized Oxidation of a Bianthryl-Based SURMOF

#### 4.1.1 Introduction

In the present work, the SURMOF approach has been used to assemble the organic chromophore bianthryl as a linker to produce well-defined 2D-layered Zn-bianthryl-based SURMOF-2. The bianthryl-linker is arranged in a closely-packed geometry, as shown in **figure 4.1**. Photophysical characterizations of the Zn-bianthryl based SURMOFs thin-film revealed the presence of inter-bianthryl electronic interactions and a photochemical reaction after prolonged UV-light irradiation in the presence of oxygen. In-depth structural and spectroscopic characterizations (UV-Vis, infrared, Raman, EPR and NEXAFS spectroscopy) revealed an oxidation process involving one of the anthracene cores of bianthryl and the formation of singlet oxygen ( $^1\text{O}_2$ ). In the following, we show the sensitization process of  $^1\text{O}_2$  by the Zn-bianthryl based SURMOF and the consequent photochemical reaction with the second anthracene moiety yielding a stable peroxide-functionalized SURMOFs.

#### 4.1.2 The structure of the linkers and the SURMOFs.

The chemical structures of 10,10-diphenyl-9,9'-dianthracene (bianthryl) and Zn-bianthryl based SURMOF-2 shown in **figure 4-1. a**, and **4-1.b** respectively.

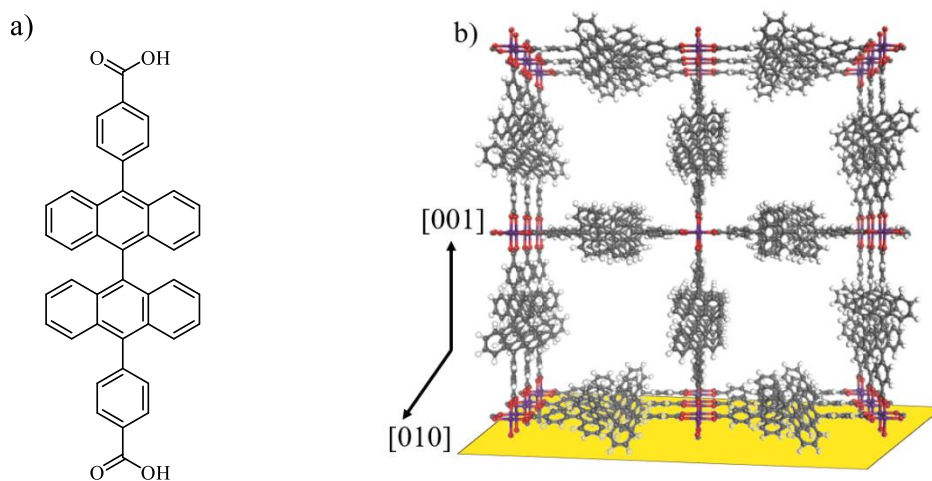


**Figure 4-1:** a) The structure of the bianthryl linker; b) the simulated structure of the Zn-bianthryl based SURMOF-2.

### 4.1.3 Synthesis and characterization Zn-bianthryl based SURMOF

The Zn-bianthryl based SURMOFs were prepared by using layer-by-layer spin coating (LbL), and layer-by-layer spray as described in chapter 3.7&3.8. Zn-bianthryl-based SURMOF was confirmed by using out-of plane XRD diffraction scans and in-plane XRD. The out-of-plane XRD pattern showed that it is highly crystalline and oriented with the [001] direction perpendicular to the substrate.<sup>84</sup> The out-of-plane XRD data exhibited reflexes corresponding to (001), (002), (003), (004), and (005) planes at  $2\theta = 3.26, 6.5, 9.78, 13.08,$  and  $16.38^\circ$ , respectively. The in-plane XRD pattern showed reflexes corresponding to (100), (200), (300), (400) and (010), planes at  $2\theta = 3.28, 6.63, 9.8, 13.03,$  and  $13.29^\circ$ , respectively. Due to the P4 symmetry of the SURMOF-2 structure<sup>222</sup>, the position of the orientation [001], and [100] are similar. The diffraction peak corresponding to the (010) plane suggested an inter-2D sheet distance of  $\sim 6.5 \text{ \AA}$  ( $c$ -axis). For this orientation of SURMOF-2, the 1D pores characteristic for the SURMOF structure run parallel to the substrate plane ( $c$ -axis). These XRD data confirmed the presence of a square grid-like 2D structure of the Zn-bianthryl-based SURMOF. Also, the simulated XRD agree with the XRD patterns, as shown in figure 4-2.

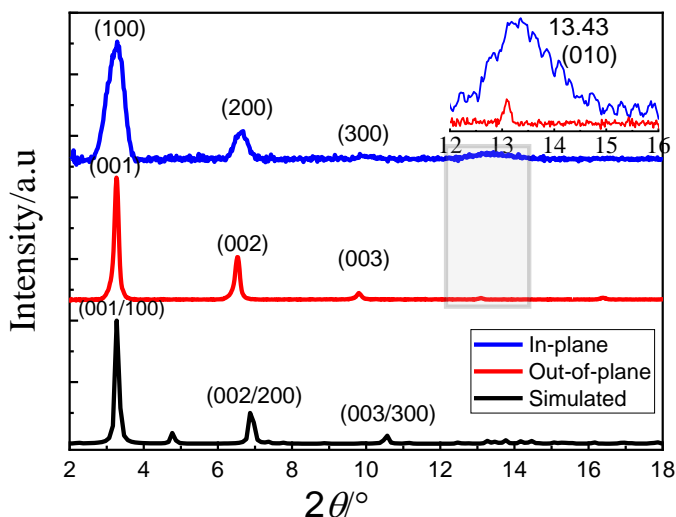


**Figure 4-2:** XRD pattern of the calculated Zn-bianthryl-based SURMOF (black), XRD -out-of-plane (red), and XRD in-plane (blue).

IRRAS data recorded for Zn-bianthryl-based SURMOF which was grown on MUD SAMS/Au and bianthryl (linker), as organic compounds are shown in figure 4-3. IR data revealed two-bands at  $1592 \text{ cm}^{-1}$  and  $1410 \text{ cm}^{-1}$ , which are attributed to asymmetric and symmetric stretching of the  $\text{COO}^-$

group, respectively. The IR spectrum recorded for the bianthryl linker showed two bands at 1685  $\text{cm}^{-1}$  and 1607  $\text{cm}^{-1}$ , which can be assigned to the asymmetric and symmetric bands of the COOH group. From these results, we can notice that the difference between the coordinating carboxylate and carboxylic acid is around ( $\Delta\nu\text{COO}^-$ )  $\sim 197 \text{ cm}^{-1}$ , which is an indication for the coordination between the metal center, Zn, and the carboxylic acid.<sup>223</sup>

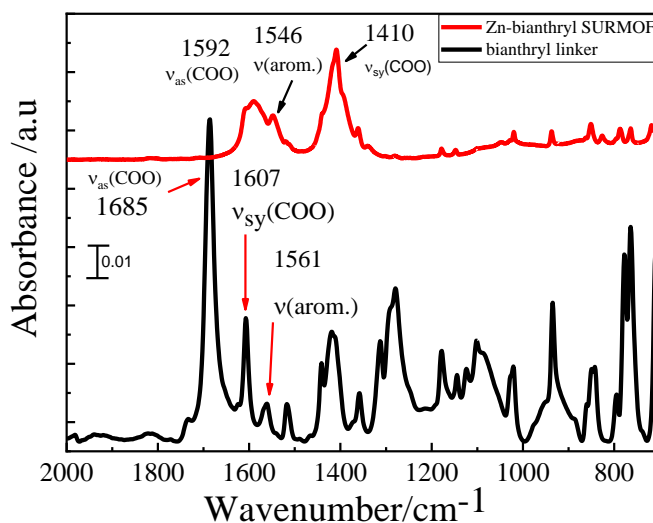


**Figure 4-3:** IR spectrum of the bianthryl linker (black color), and IRRAS spectrum of the Zn-bianthryl based SURMOF-2 grown on MUD SAMS/Au (red color).

The Zn-bianthryl-based SURMOF was grown on a quartz substrate, as described in **chapter 3.7**, and subsequently characterized by UV-Vis spectroscopy. The UV-Vis spectrum of the ground state of Zn-bianthryl based SURMOF showed an absorption band located at 273 nm. The UV-Vis spectrum of the solvated bianthryl showed an absorption band at 257 nm. In addition, for both systems additional weaker absorption bands were absorbed at 342, 361, 382, and 405 nm, which were attributed to  $\pi$ - $\pi^*$ , and  $n$ - $\pi^*$  transition of bianthryl. From this data, we concluded that the Zn-bianthryl SURMOF showed a red shift around 16 nm, as shown in **figure 4-4**. This indicates that the anthracene units of the bianthryl linker interact along the stacking direction, i.e. [010] axis, as expected from the short distance between the 2D layers.

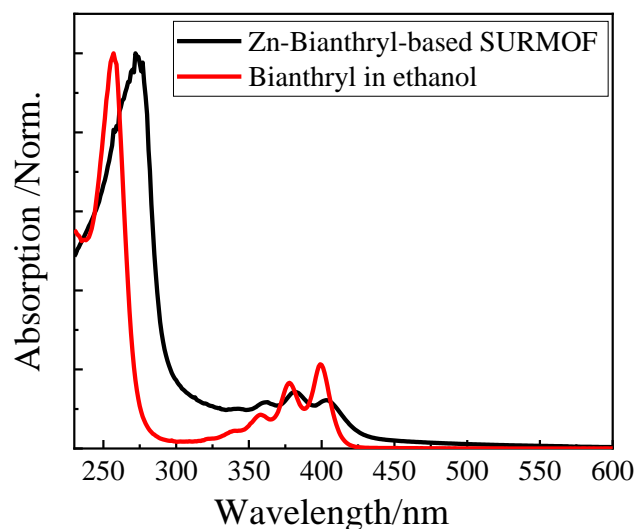


**Figure 4-4:** UV-Vis spectrum of Zn-bianthryl based SURMOF (black color), and the UV-Vis of the ethanol solution of the bianthryl (in red color). The data were recorded in transmission.

#### 4.1.4 Photophysical characterization of Zn-bianthryl based SURMOF

Zn-bianthryl SURMOF-2 samples showed cyan color when illuminated with an UV-lamp with wavelength (365 nm). After prolonged continuous irradiation of Zn bianthryl-based SURMOF for 6 h with UV-lamp under ambient conditions, the luminescence of the sample disappeared and the color of the sample switched to reddish-yellow color, as shown in **figure 4-5**.

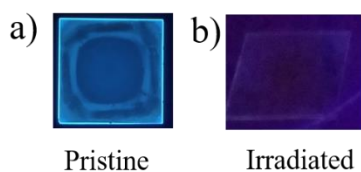


**Figure 4-5:** a) Zn-bianthryl-based SURMOF under UV-lamp immediately; b) Zn-bianthryl-based-SURMOF after continues irradiation for 6h under ambient conditions.

After prolonged illumination of the sample under ambient conditions, UV-Vis spectra were collected. The corresponding spectrum showed two new bands around 315 nm, which has been reported in the literature<sup>224</sup>, and 440 nm, as shown in **figure 4-6a**. For comparison, UV-Vis spectra were recorded for samples that were irradiated in an inert atmosphere for the same time, such spectra did not show any new bands, as shown in **figure 4-6b**. The recorded UV-Vis spectrum for the sample which was illuminated under ambient conditions revealed that a reaction happened between the excited Zn-bianthryl-based SURMOF and O<sub>2</sub>.

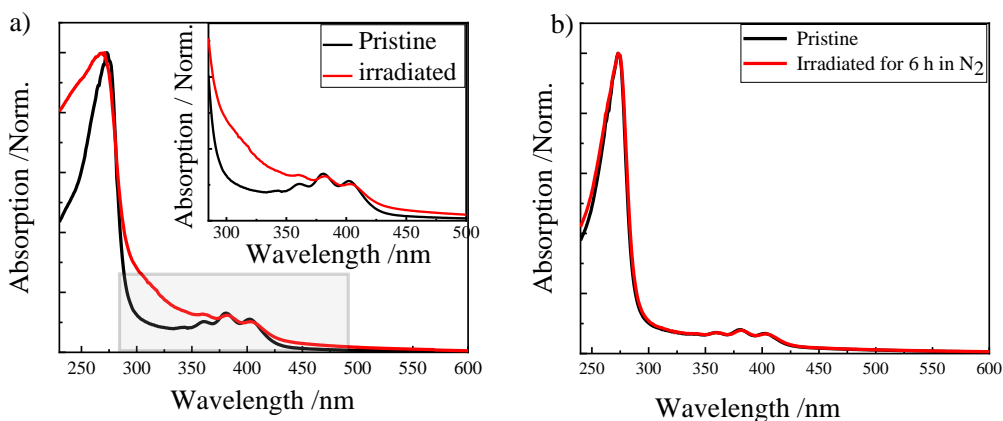


**Figure 4-6:** a) UV-Vis spectra of Zn-bianthryl based SURMOF as a pristine (black), after irradiation under ambient conditions for 6h (red); b) Zn-bianthryl based SURMOF as a pristine sample (black), and after irradiation under an inert conditions for 12 h (Red).

For comparison, Zn-anthracene based (ADB) SURMOF samples were synthesized and characterized as described in ref.<sup>225</sup> UV-Vis spectra were collected for the pristine Zn-ADB based SURMOF sample, and after prolonged irradiation of the sample under ambient conditions with a UV-lamp for 6h. The corresponding UV-Vis spectra of the irradiated samples did not show any additional bands after prolonged irradiation under ambient conditions, as shown in **figure 4-7**. From these results, we concluded that a photochemical reaction took place under irradiation of Zn-bianthryl-based SURMOF in ambient conditions. The same reaction conditions did not show the same effect on the Zn-ADB-based SURMOF.

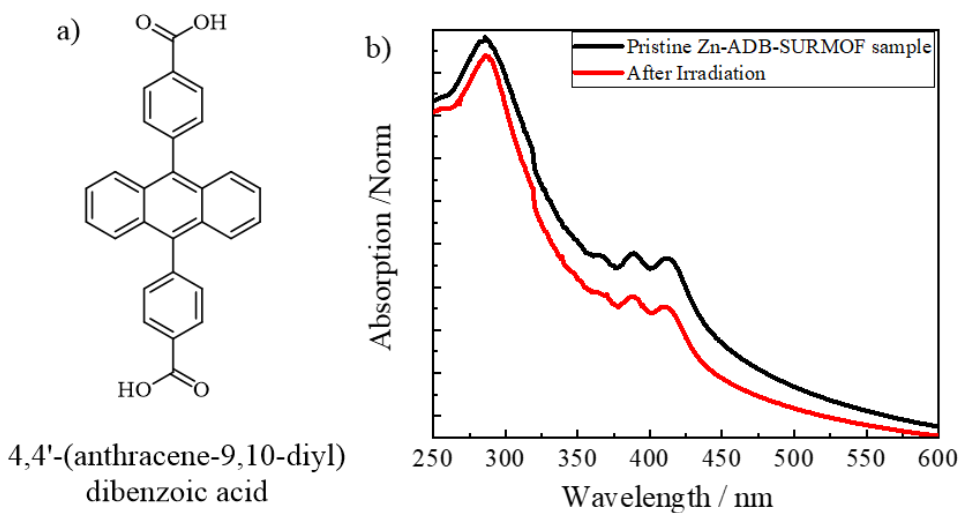


**Figure 4-7:** a) The structure of the linker (ADB); b) UV-Vis spectra of the pristine Zn-ADB based SURMOF sample (black color); Zn-ADB based SURMOF after irradiated for 6h under ambient

conditions (red color).

#### 4.1.5 Further characterization of the prolong irradiation product

Further characterizations have been done to characterize the product of prolonged irradiated Zn-bianthryl-based SURMOF under ambient conditions, such as in situ in-plane, out-of-plane XRD, IR, Raman spectroscopy, and NEXAFS.

In situ in-plane and out-of-plane XRD were measured for the Zn-bianthryl based SURMOF, during continuous irradiation for 6 h under ambient conditions. The XRD patterns for the Zn-bianthryl-based SURMOF did not show any degradation, or any new substantial peaks appear. However, the third order peaks corresponding to the (003) and (300) peaks showed a slight lattice contraction for the irradiated Zn-bianthryl SURMOF. In the case of the out-of-plane XRD pattern, the (003) peak was contracted by 0.2%, while in the in-plane XRD pattern the (300) peak around 1.1%. From this data, we proposed that this contraction is due to water loss from the structure of the SURMOF caused by irradiation, as shown in **figure 4-8**.

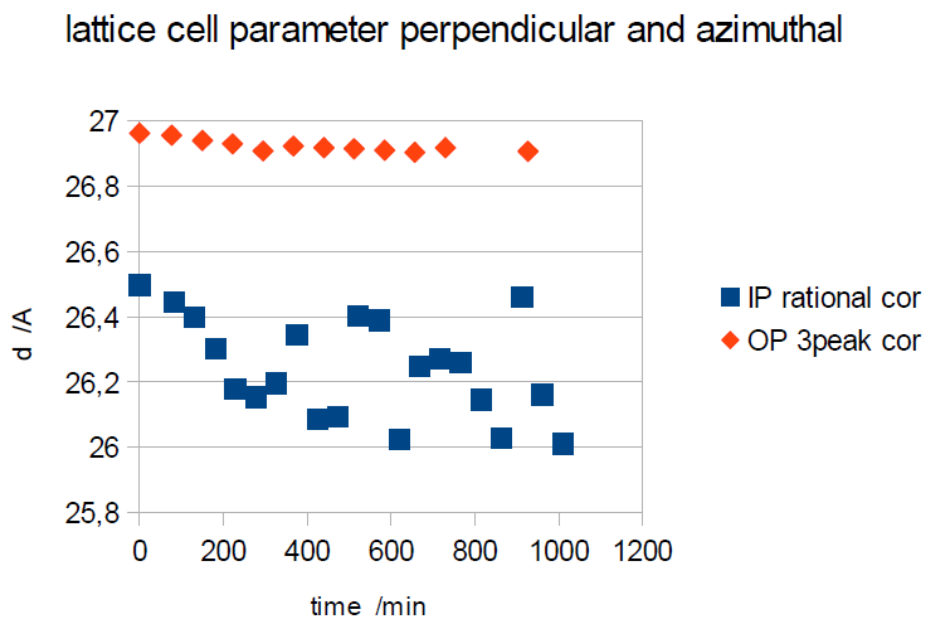


**Figure 4-8:** The  $d / \text{\AA}$  corresponding to (003/300) peaks as function of time of irradiation for both out-of-plane, and in-plane XRD as, a pristine sample and during irradiation.

To understand the effect of prolonged irradiation under the ambient conditions, IRRAS data was collected for the pristine sample, and the sample after irradiation under ambient conditions for 2h,

and 6h. IRRAS data were recorded for the aforementioned samples are shown in **figure 4-9**. From these spectra, we concluded that the Zn-paddlewheel ( $\text{Zn-COO}^-$ ) was not affected by prolonged irradiation under ambient conditions. This result suggested that the Zn-bianthryl based SURMOF was stable under prolonged irradiation. However, IRRAS spectra showed the effect of the prolonged irradiation under ambient conditions in the aromatic structure of the linker. After irradiation a clear change on absorption intensity of C=C was observed. In addition, a change was detected for the aromatic C-H vibration bands. The intensity of the absorbance of C=C aromatic bending appears around  $830\text{-}810\text{cm}^{-1}$  and decreased gradually after long irradiation. This decrease in absorbance intensity of C=C aromatic stretching around  $3100\text{ cm}^{-1}$  took place gradually with increasing the irradiation time. After 6 h of irradiation, the two peaks of C=C aromatic merged into one broad peak. Therefore, IRRAS data showed that a photochemical reaction took place in the bianthryl, linker, after the prolonged irradiation under ambient condition.

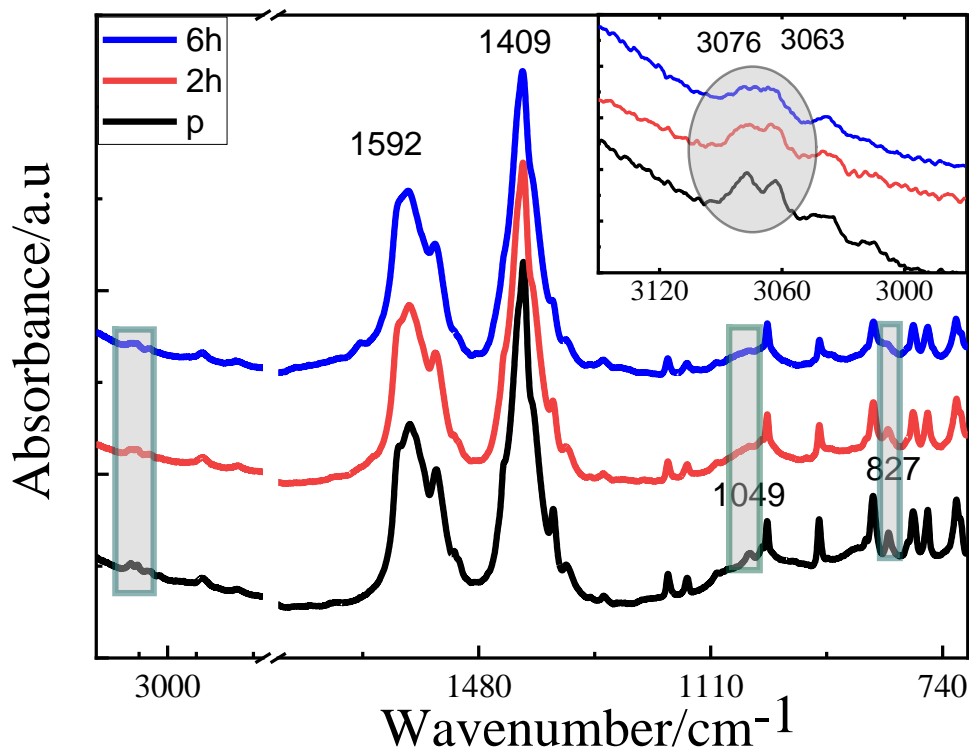


**Figure 4-9:** IRRAS spectra for Zn-bianthryl SURMOF, the pristine sample (black), the sample that was irradiated under ambient conditions for 2h (green), 6h (red).

The functional group, wavenumber /cm <sup>-1</sup>	Pristine	Irradiated 2 h	Irradiated 6 h
<b>Two neighboring C-H aromatic</b> , 830-840 cm <sup>-1</sup>	strong	The intensity decreased, but did not vanish	The intensity is decreased too much
<b>Aromatic C-H in plane bending</b> , 1049 cm <sup>-1</sup> peak	medium	decreased	Vanished
<b>Carboxylate COO<sup>-</sup></b> Two peaks at 1410, 1592 cm <sup>-1</sup>	strong	strong	strong
<b>C-H aromatic stretching</b> , at 3050-3100 cm <sup>-1</sup>	medium	broadened	broad peak.

**Table 4-1:** Vibrational frequencies of Zn-bianthryl based SURMOF as a pristine sample, after irradiation under ambient conditions for 2h and 6h.

UV-Vis spectra, emission spectra, in-plane and out-of-plane XRD patterns, IR data, and the naked eyes-pictures under UV light for prolonged irradiated sample under ambient conditions revealed that a photochemical reaction took place affecting the linker. Furthermore, the product of the reaction that formed in Zn-bianthryl-based SURMOF was stable.

To understand the photochemical reaction that took place on the Zn-bianthryl SURMOF upon prolonged irradiation under ambient conditions, an indirect method was applied to detect potentially sensitized <sup>1</sup>O<sub>2</sub>.<sup>226</sup> 50 μL of the compound 2,2,6,6-tetramethyl-piperidine (TEMP) were dissolved in 5 ml of methanol and 10 ml of chloroform. The solution was flashed with O<sub>2</sub> for 5 min. Subsequently, the pristine Zn-bianthryl-based SURMOF sample was added to the solution and the electromagnetic resonances signal (EPR) was recorded for the mixture in dark. The UV-lamp was switched on and the EPR signals were collected after 1 min, 3 min, 6 min, 9 min, and 2 h. EPR signal for the mixture in the dark was silent, while EPR spectra for the mixture under illumination in the ambient condition showed signals. EPR data recorded after 1 min of illumination under ambient conditions showed the highest signal intensity, see **figure 4-10a**. On the basis of this data we concluded that the illumination of the sample Zn-bianthryl SURMOF first converted <sup>3</sup>O<sub>2</sub> to <sup>1</sup>O<sub>2</sub>. Then, the produced <sup>1</sup>O<sub>2</sub> reacted with TEMP and afforded TEMPO, which is EPR active. Irradiation for more than 1 min produced more <sup>1</sup>O<sub>2</sub>, which reacted with one of the anthracene moiety of the bi-anthracene to produced endoperoxide, as shown in **figure 4-10b**. As a result, the EPR signal intensity decreased with further irradiation.

Generally, <sup>1</sup>O<sub>2</sub> that is produced upon irradiation of the photosensitizer reacts with 1,3-dienes to

afford endoperoxide.<sup>227–231</sup> When the electron density of aromatic hydrocarbon increases<sup>232</sup>, the reactivity toward  $^1\text{O}_2$  also increases due to the electrophilic nature of  $^1\text{O}_2$ .<sup>233</sup> Also, increasing the numbers of fused phenyl rings of the aromatic hydrocarbons increases the reactivity toward singlet oxygen by two orders of magnitude for each supplementary fused ring.<sup>232</sup> Herein, two reactions took place at the same time. The first reaction, the reaction between TEMP and the produced  $^1\text{O}_2$  afforded 2,2,6,6-tetramethyl-1-piperidinyloxy (TEMPO), as shown in **reaction scheme 4-1**. In addition, the reaction of the produced  $^1\text{O}_2$  with one anthracene moiety produced an endoperoxide. The reaction rate of the anthracene moiety of bianthryl (linker) with  $^1\text{O}_2$  in the excited state was higher than the reaction rate of TEMP with  $^1\text{O}_2$ , as shown in **reaction scheme 4-2**. Therefore, the EPR signal of the formed TEMPO decreased clearly after 1 min of irradiation due to the self-photooxidation reaction that happened on one anthracene moiety in bi-anthracene molecule (bianthryl).

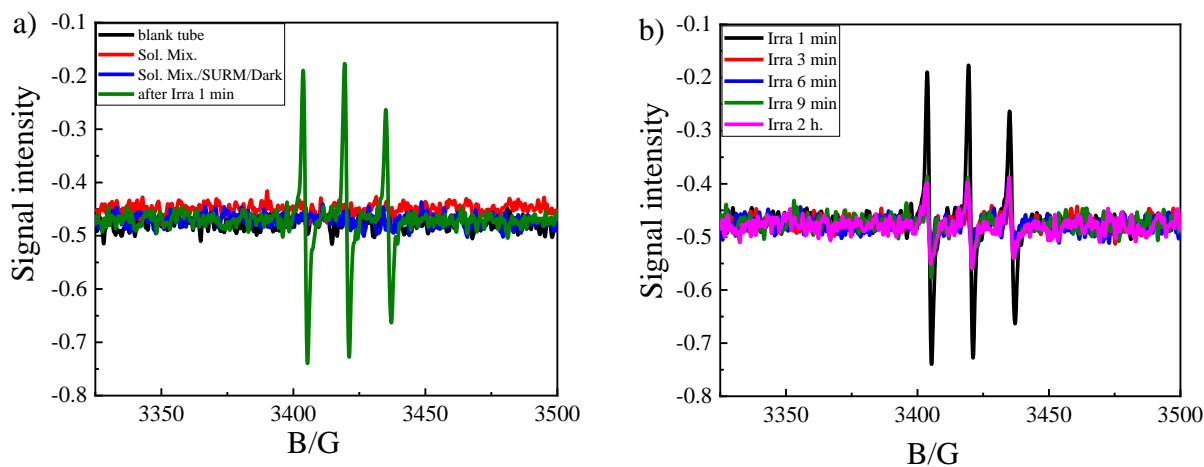


**Figure 4-10:** EPR signal recorded for the product TEMPO, which was produced from the reaction between  $^1\text{O}_2$  and TEMP during irradiation of Zn-bianthryl-based SURMOF sample (a) sol. Mix; MeOH/ $\text{CHCl}_3$ /TEMP /SURMOF. This mixture was measured in dark and after irradiation for 1min(b) the solvent mixture,  $\text{CHCl}_3$ , MeOH/SURM, TEMP, after irradiation for 1 min, 3 min, 6 min, 9min and 2 hours.



over time, as shown in **figure 4-11**. The EPR spectra did not show a signal for the mixture in the dark nor after irradiation. This result revealed that the reaction did not take place via superoxide mechanism. The proposed reaction is shown in the reaction **scheme 4-3**.

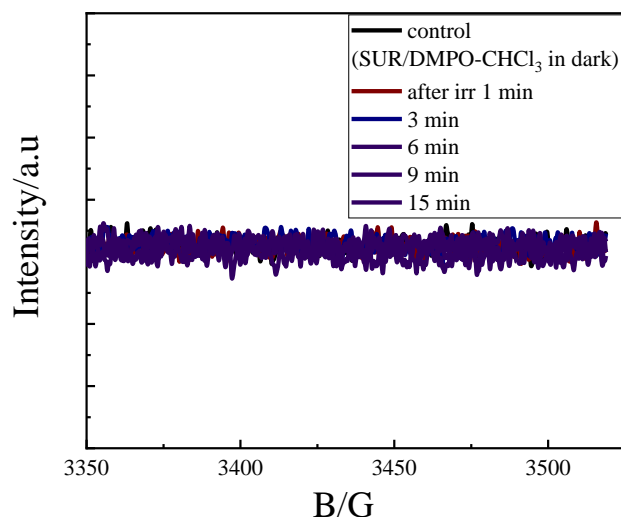
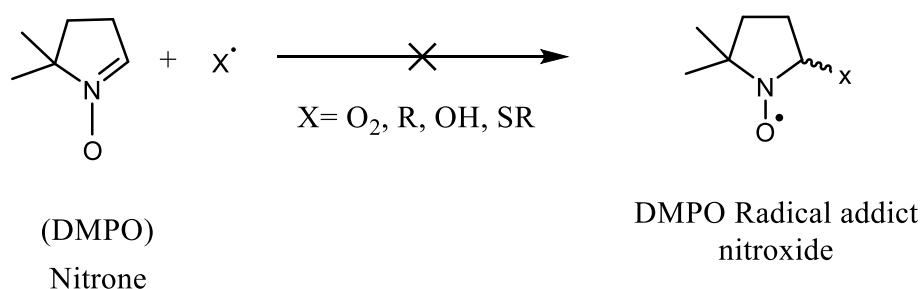


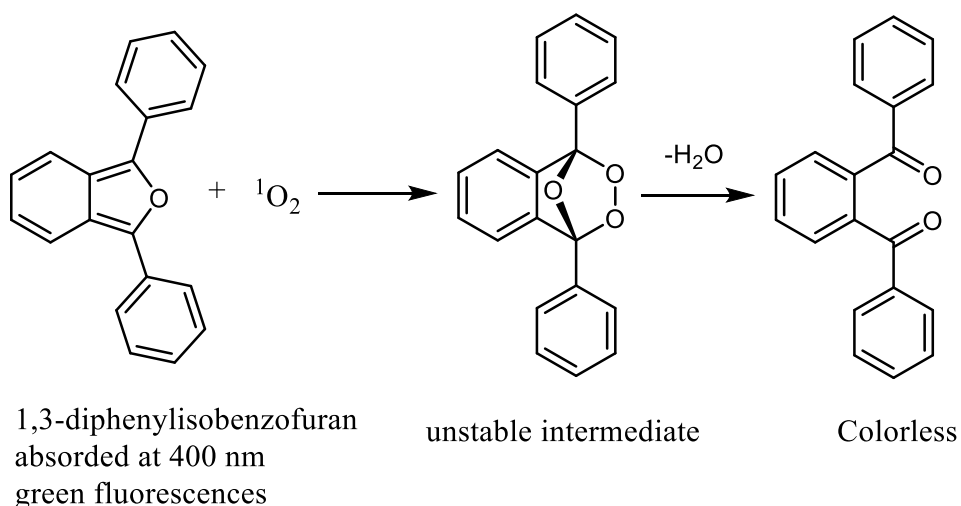
**Figure 4-11:** EPR signal recorded for the reaction of DMPO with the produced singlet oxygen produced with irradiation of Zn-bianthryl based SURMOF.



**Reaction scheme 4-3:** The reaction between DMPO and the expected radical to produce superoxide.

Furthermore, 1,3-diphenylisobenzofuran (DPBF) was used as a detector for <sup>1</sup>O<sub>2</sub> because it is undergoing a 2,4-cycloaddition reaction with <sup>1</sup>O<sub>2</sub> to afford endoperoxide. DPBF is a conjugated system and shows an absorption band at 412 nm.<sup>235</sup> The reaction between DPBF and <sup>1</sup>O<sub>2</sub> is shown in the **reaction scheme 4-4**. The DPBF endoperoxide compound is unstable and irreversibly transforms to 1,2-dibenzoylbenzene with lost π-system. Consequently, the absorption of DPBF at 412 nm is lost. As a result, the photobleaching of DPBF is expected under the irradiation of a photosensitizer.<sup>236</sup> On the other hand, the lifetime of the <sup>1</sup>O<sub>2</sub> depends on the solvents. Therefore, two different types of solvent have been used: ethanol (a protic solvent), where the lifetime of

singlet oxygen is very short, and acetonitrile (an aprotic solvent like DMF, DMSO, acetonitrile, acetone, THF) where the lifetime of the singlet oxygen is longer than in protic solvents<sup>237</sup>, as shown in **figures 4-12**. Three different solutions of DPBF (0.05mM, 10ml) have been used; a solvated bianthryl linker in ethanol (0.05mM,2ml) was added to the first solution. A pristine Zn-bianthryl-based SURMOF sample was added to the second solution, and the last DPBF solution was used as a control to monitor the effect of UV lamp. Afterwards UV-Vis spectra were collected during irradiation every 10 min until photobleaching of DPBF was observed. As shown in **figure 4-12**, the effect of the irradiation on the ethanol solution of DPBF and solvated bianthryl with an ethanol solution of DPBF did not show photobleaching. While the lifetime of the <sup>1</sup>O<sub>2</sub> in ethanol is very short, the irradiation the Zn-Bianthryl based SURMOF showed an effect of the photobleaching of DPBF solution, as shown in **figure 4-12b**.



**Reaction scheme 4-4:**The reaction between DPBF with singlet Oxygen.

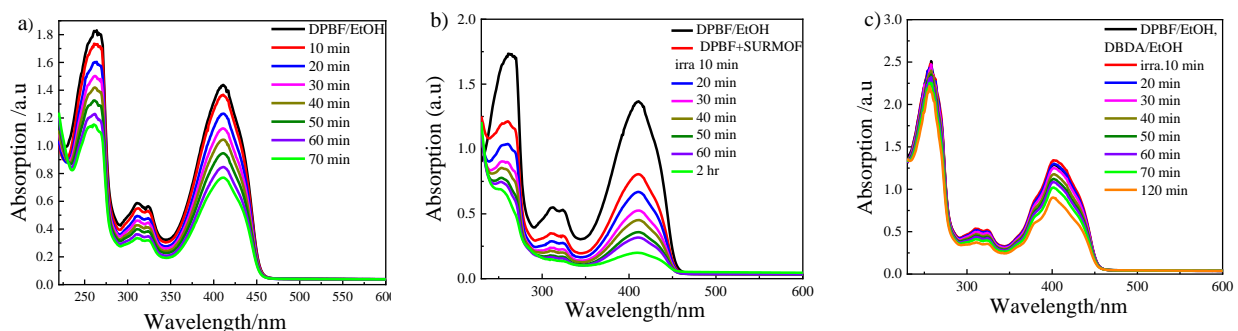


**Figure 4-12:** UV-Vis spectra for photobleaching of DPBF a) solvated DPBF / ethanol (control); b) Zn-bianthryl based SURMOF; c) the effect of ethanol solution of the bianthryl linker DPBF/ Et OH.

In contrast to the protic solvents, the aprotic solvent such as acetonitrile is a suitable medium for singlet oxygen due to the long-lifetime of  $^1\text{O}_2$ , which has lifetime of 81.8  $\mu\text{s}$  at room temperature.<sup>238</sup> A 0.02 mM solution of bianthryl in acetonitrile (2 ml) was added to a 0.05 mM solution of DPBF in acetonitrile (10 ml). In addition, Zn-bianthryl based SURMOF was added to another container that has DPBF/acetonitrile (10 ml, 0.05 mM). The previous two different containers were irradiated using an UV-lamp with a wavelength of 366 nm under ambient conditions, as shown in **figure 4-13 a,b**. Consequently, UV-Vis spectra were recorded for both of them in dark and after every 10 minutes of irradiation. The data revealed that Zn-bianthryl based SURMOF produced  $^1\text{O}_2$  immediately, while the solvated bianthryl required longer time to produce  $^1\text{O}_2$ . Also, the solvated bianthryl and Zn-bianthryl based SURMOF worked in the aprotic solvent. While the rate of the photobleaching DPBF using the Zn-bianthryl based SURMOF was faster than the rate of photobleaching of DPBF using solvated bianthryl. A control experiment was done to exclude the effect of light on the photobleaching of DPBF in acetonitrile, as shown in **figure (4-13c)**. From UV-Vis spectrum of the control experiment, we observed a little light effect on the photobleaching of the DPBF. This effect can be neglected in comparison with the photobleaching of DPBF using the solvated bianthryl or Zn-bianthryl SURMOF as a photosensitizer.

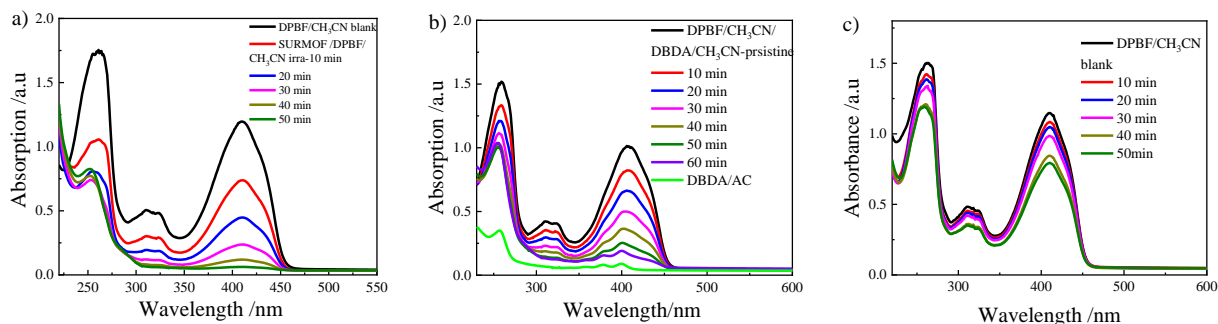


**Figure 4-13:** Photobleaching of DPBF in acetonitrile a) using Zn-bianthryl based SURMOF as a photosensitizer in acetonitrile; b) photobleaching of DPBF using solvated bianthryl / acetonitrile; c) the effect of light on DPBF in acetonitrile.

The results of the experiments discussed above revealed that a photobleaching of DPBF took place using Zn-bianthryl based SURMOF. This is an indication for the production of  $^1\text{O}_2$  via a prolonged irradiation of Zn-bianthryl based SURMOF. The rate of photobleaching of DPBF using Zn-bianthryl based SURMOF was slow in comparison to the reported photosensitizer-based powder MOFs.<sup>239</sup> These results are in agreement with EPR results, which is an indication for further reaction

that took place in the same time of formation the DPBF-endoperoxide. To probe the product of the self-photooxidation of the Zn bianthryl-based SURMOF, further experiments were done using X-ray absorption near edge fine structure (C-K edge NEXAFS) spectroscopy. C-K-edge NEXAFS data were collected for the pristine Zn-bianthryl based SURMOF sample, after prolonged irradiation under ambient conditions for 6 h with an UV-lamp with a wavelength of 365 nm. NEXAFS spectra for the sample after illumination showed a difference in the absorption resonance intensities compared to the pristine sample. These absorptions are characteristic for the excitation of C1s core electrons from occupied orbitals localized at bianthryl molecule (linker) to unoccupied  $\pi^*$  and  $\sigma^*$  orbitals into molecular orbitals of Rydberg character. The pristine sample showed C1s- $\pi^*$  transition, the majority of  $\pi^*$  transition occur between 284 and 288 eV. This excitation also overlaps with the  $\sigma^*$  transitions above 287 eV. The pristine SURMOF sample showed four absorption transition band at 284 eV (aromatic-C associated with aromatic C, (C=C), 285 eV<sup>211</sup> (protonated substituted aromatic-C, C-H), 286 eV C-aromatic associated with Benzoate (phenyl carboxylate ring, C-Ph-COO<sup>-</sup>), and 288.4 eV for carboxylate carbon. The irradiated sample exhibited the same four absorption bands with a dramatic decrease in the absorption intensity of two absorptions at 284eV and 286 eV. This decrease revealed the change in transition of C1s- $\pi^*$  due to the loss of aromaticity and transformed to aliphatic carbon. The reaction between one anthracene moiety in bi-anthracene and <sup>1</sup>O<sub>2</sub> produced endoperoxide. Then, the aromaticity of in the 10,9- position of the bi-anthracene is lost, while the other anthracene moiety kept its aromaticity. The aliphatic carbon has absorption energy higher than 293 eV and exhibited broad absorption, as shown in **figure 4-14**.

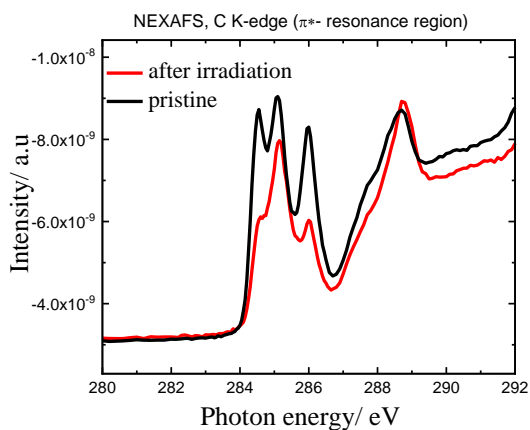


**Figure 4-14:** NEXAFS spectra for Zn-bianthryl SURMOF pristine (black), and Zn-bianthryl

SURMOF after irradiation under ambient conditions.

To prove the formation of the endoperoxide product, which cannot be detected using IRRAS due to the absence of transition dipole moment in O-O vibration. IRRAS affords a weak band for O-O or undetectable. As a result, Raman spectroscopy is a suitable tool to detect the formed new bond O-O which is detected in the range 700-950  $\text{cm}^{-1}$  by Raman spectroscopy.<sup>240</sup> Accordingly, the pristine Zn-bianthryl based SURMOF sample and the irradiated sample were measured using Raman spectroscopy, as shown in **figure 4-15b**. The pristine Zn-bianthryl-based SURMOF sample showed a similar spectrum, which is similar to that reported in the literature.<sup>241</sup> While the irradiated Zn-bianthryl-based SURMOF in the ambient conditions showed three new peaks of 803.5  $\text{cm}^{-1}$  (strong) that peak can be attributed to  $\nu$  (O-O), 870  $\text{cm}^{-1}$  (medium) may result from stretching of  $\nu$  (C-O-C), and peak at 1047  $\text{cm}^{-1}$  may be attributed to  $\nu$  (C-O-C).<sup>242</sup> Raman spectra for the pristine Zn-bianthryl-based SURMOF sample and the irradiated sample showed that there was an endoperoxide bond formed due to producing  $^1\text{O}_2$  by Zn-bianthryl-based SURMOF. That new bond resulted from reaction between  $^1\text{O}_2$  with one anthracene unit of bi-anthracene which afforded endoperoxide. The resulted molecule endoperoxide is shown in **figure 4-15a**.

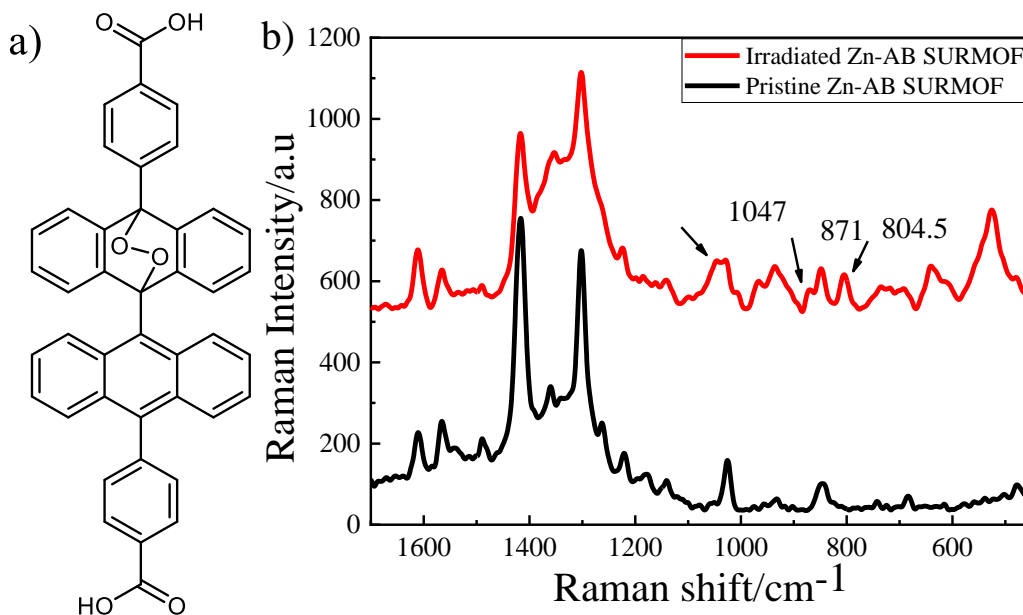


**Figure 4-15:** a) The product of irradiation in ambient condition; b) Raman spectra for Zn-bianthryl SURMOF pristine sample (black) and irradiated sample (red).

Interestingly, Raman spectra recorded for the pristine Zn-ADB based SURMOF sample and the

irradiated Zn-ADB based SURMOF sample did not show any change, as shown in **figure 4-16 b**. These results provide a clear evidence for the new bands formed in Zn-bianthryl SURMOF resulting from endoperoxides. Bianthryl produced  $^1\text{O}_2$  under illumination, followed by reaction of  $^1\text{O}_2$  with anthracene. Because anthracene is a diene compound it reacted with the produced  $^1\text{O}_2$  as a self-photooxidation.

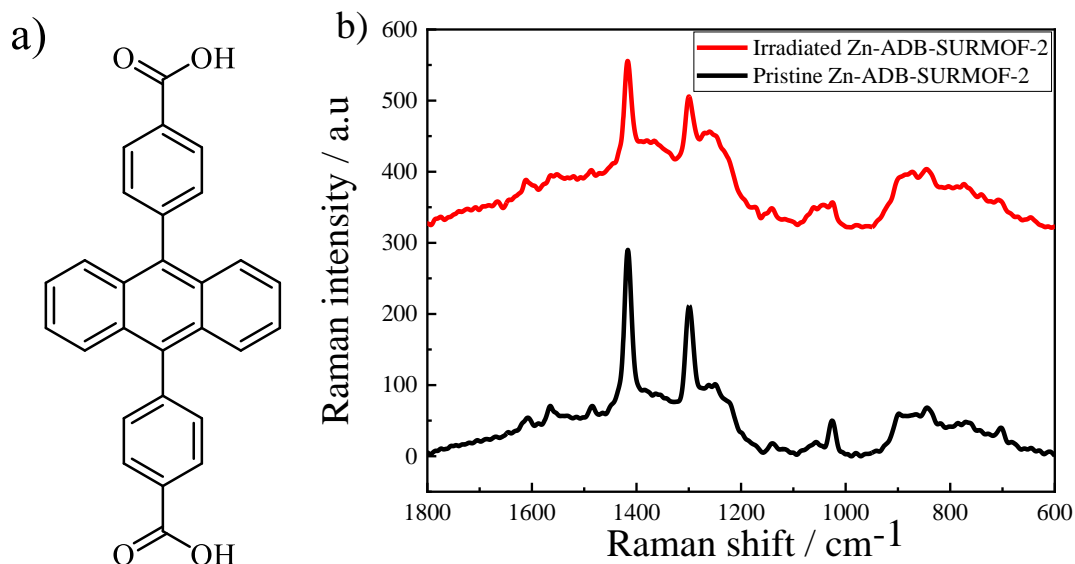


**Figure 4-16:** a) The structure of the 4,4'-(anthracene-9,10-diyl) dibenzoic acid (ADB) linker; b) Raman spectra of Zn-ADB SURMOF as pristine and after irradiation under ambient conditions for 6h.

The morphology of the Zn-bianthryl-based SURMOF sample before and after irradiation showed a compact, pinhole-free, and homogenous film with little roughness. From pictures we concluded that the irradiation of the Zn-bianthryl based SURMOF did not change the morphology of the SURMOF, as shown in **figure 17a, b**.

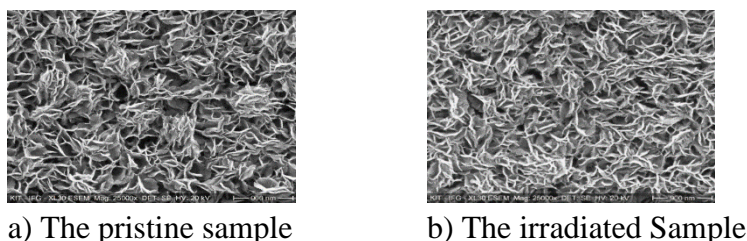


**Figure 4-17:** a) SEM for the pristine Zn-bianthryl based SURMOF sample; b) and the Zn-bianthryl based SURMOF after irradiation under ambient conditions for 6h.

The generation efficiency of the  $^1\text{O}_2$  and the self-quenching (self-photooxidation) efficiency depends on the solvent polarity.<sup>243-245</sup> Accordingly, the irradiation was done for the solvated bianthryl in different solvents, on protic solvents, such as ethanol and aprotic solvents, such as tetrahydrofuran (THF) and acetonitrile. The UV-Vis spectrum of solvated bianthryl in ethanol (0.02mM) irradiated with the same wavelength for 1 day did not show any detectable change. This observation can be explained by the short lifetime of  $^1\text{O}_2$  in ethanol which is around 9,7  $\mu\text{s}$ .<sup>246</sup> UV-Vis spectra recorded for a solution of the solvated bianthryl in acetonitrile (0.02 mM) and bianthryl in THF (0.02 mM) after irradiation in ambient condition for 12 h showed a new band. The change in the UV-Vis spectra of the solvated bianthryl in THF afforded obvious bands around 300 nm, and 450 nm, while UV-Vis spectrum of the solvated bianthryl in acetonitrile did not afford the same obvious change. However, the lifetime of  $^1\text{O}_2$  in acetonitrile is longer than the lifetime of  $^1\text{O}_2$  in THF 81.8  $\mu\text{s}$ , and 20  $\mu\text{s}$  respectively.<sup>238,247</sup> This result suggested that not only solvent polarity has an effect, but also the solubility plays a role in the reaction rate, as shown in **figure 4-18**.

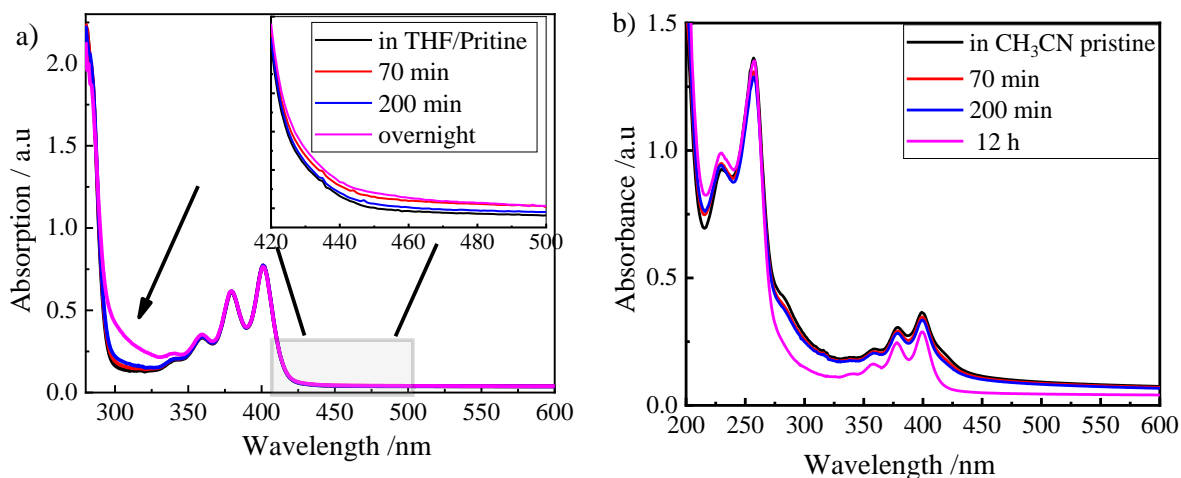


**Figure 4-18:** a) UV-Vis of bianthryl in THF as a pristine solution, and after irradiation under ambient conditions for 70 min, 200 min, and 12 hours.; b) UV-Vis spectra of bianthryl in acetonitrile as pristine solution, and after irradiation in the ambient conditions for 70 min, 200 min, and 12 hours.

Generally, for molecules that have fused phenyl rings, such as bi-anthracene, the energy difference between HOMO and LUMO is small. In addition, introducing more phenyl rings in position 9,9' of bi-anthracene moiety further decreases the energy difference between HOMO and LUMO.<sup>224</sup> As a result, the energy required for the promotion of the electrons from the ground states to the excited states is small. After promotion of the electrons to the highest excited states, intersystem

crossing (ISC) to the excited triplet state can happen in the range  $10^{-11} - 10^{-9}$ s,  $10^{-10} - 10^{-8}$ s respectively. The excited electrons in the triplet state have a long lifetime in the range of ( $\mu$ s). This followed with the relaxation to the ground state transfers the energy to  $O_2$  molecule. The oxygen molecule is excited to the singlet states, as shown in **figure 4-19**.

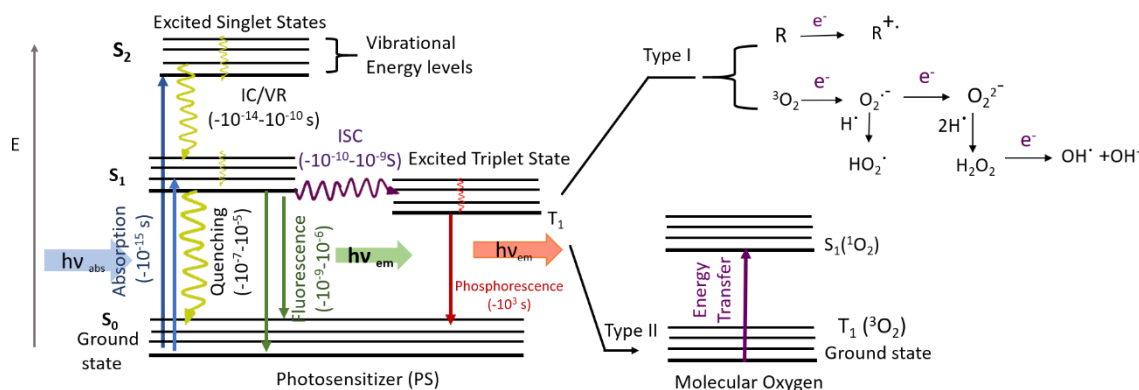


**Figure 4-19:** Jablonski diagram describing the underlying photophysics and photochemistry of excited photosensitizer states and reactive dioxygen species. This figure was reproduced with modification with permission from WILEY ref.<sup>41</sup>

The SURMOFs offer a platform for assembling the photosensitizer and avoid aggregation and solubility issues of the photosensitizer in a suitable solvent for  $^1O_2$ . Furthermore, the SURMOF platform plays an important role for  $O_2$  permeation, which increase the rate of the reaction. These advantages of the SURMOF platform enhanced the photoresponsive properties of Zn-bianthryl-based SURMOF, which has a crystalline structure, open pores, and high accessibility. As a result, the produced  $^1O_2$  reacted with one anthracene moiety of the bianthryl compound because it is a diene compound.<sup>230,245,248,249</sup>

The endoperoxide can be decomposed by two methods, the first method is chemically. The self-photooxidation SURMOF product was soaked in tetrabutylammonium-hexafluorophosphate (TB-APF<sub>6</sub>) 1mg/mL ethanol for 8 h. The UV-Vis spectrum for the aforementioned SURMOF after reaction showed decomposition of the endoperoxide, as shown in **figure 4-20b**. In addition, acid or base medium can be used to decompose the endoperoxide product.<sup>250</sup> The other method is using an elevated temperature to release  $^1O_2$ . Consequently, the irradiated Zn-bianthryl SURMOF sample under the ambient conditions was kept in a flask connected with the Schlenk line, then it was heated under inert conditions to 160 °C overnight. The UV-Vis spectra for the sample Zn-bianthryl-

based SURMOF after heating revealed that  $^1\text{O}_2$  did not lose via heating. From this data, we can conclude that the Zn-bianthryl based SURMOF was stable at elevated temperature, as shown in **figure 4-20a**.

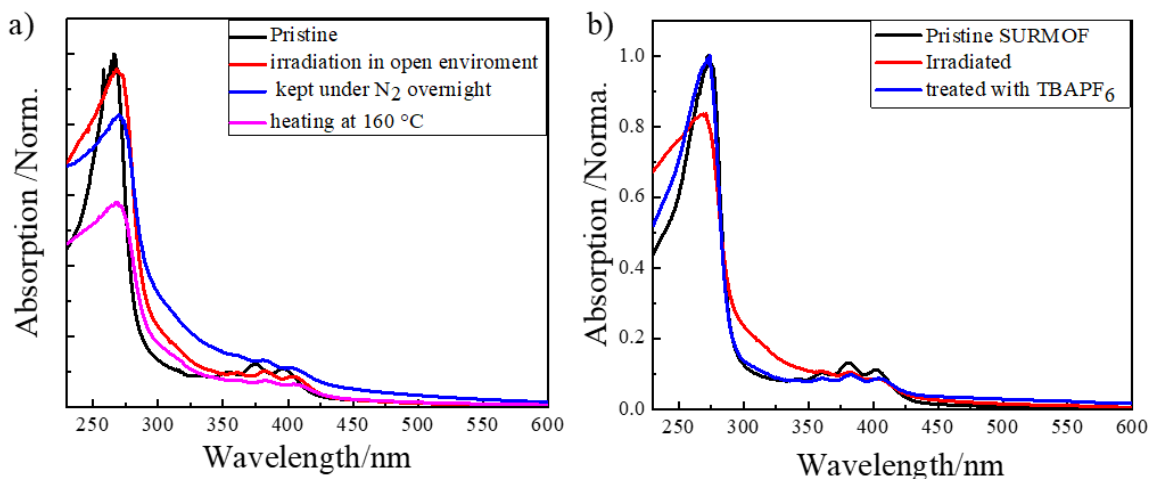


**Figure 4-20:** a) UV-Vis spectra for the effect of heat under N<sub>2</sub> for irradiated Zn-bianthryl-based SURMOF; b) UV-Vis for irradiated sample which was kept in TBAPF<sub>6</sub> for 6 h.

To confirm that no further reaction happened in the linker, acid media have been used to decompose the endoperoxide product.<sup>250</sup> In the case of SURMOF using acid led to decomposition of the SURMOF, which was confirmed by using LC-MS. This experiment was performed by dissolving the irradiated Zn-bianthryl SURMOF in 0.2 ml of acetic acid and 1 ml of ethanol. The solution mixture was used to measure the mass of the linker, as shown in **figure 4-21**. Also, the linker was dissolved in ethanol, while the pristine Zn-bianthryl based SURMOF sample was decomposed using the aforementioned method. Column chromatography was used to detect the mass of the linker for the three mixtures separately. As a result, one compound was detected at retention time 10.6 min. From the mass spectra, the three mixtures showed the same molecular weight, as shown in **figure 4-21b**. This data revealed that the acetic acid used, led to decomposition of the endoperoxide product and the SURMOF. In addition, there was not any further reaction took place in the linker.

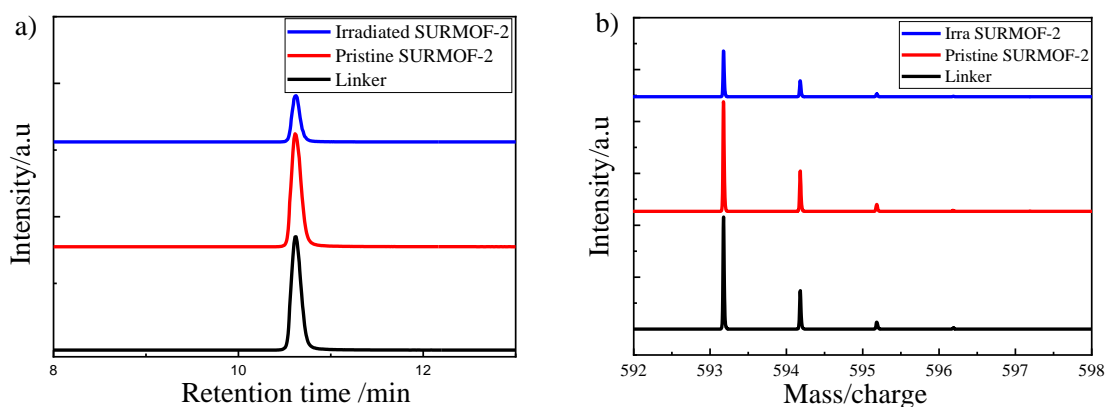


**Figure 4-21:** a) Retention time by liquid chromatography (LC); b) The mass detected for the bianthryl linker; black, the pristine Zn-bianthryl SURMOF sample; blue, and the irradiated Zn-SURMOF sample; red.

#### 4.1.6 Conclusion

The chromophoric linker bianthryl was successfully aligned into the SURMOF platform. The Zn-bianthryl SURMOF showed a highly ordered crystalline structure. The highly orientated Zn-bianthryl based SURMOF-2 showed the luminescence properties upon immediate illumination using an UV-lamp. But, the prolonged illumination of the SURMOF under ambient conditions exhibited a prominent change in the ground and excited state. As a result, the optical properties of the SURMOF changed without losing the crystallinity, which can be concluded that Zn-bianthryl based SURMOF sensitized  $^1\text{O}_2$ . The sensitized  $^1\text{O}_2$  was detected by using an indirect method as a 2,2,6,6-tetramethylpiperidine (TEMP), which produced TEMPO radical that was detected by using EPR. additionally, the produced  $^1\text{O}_2$  was also confirmed by the photo-bleaching of 1,3-diphenyl-isobenzofuran. Furthermore, the Zn-bianthryl based SURMOF underwent self-photooxidation by the produced  $^1\text{O}_2$ . The product of the self-photo-oxidation, endoperoxide, was characterized by using IR, Raman, and NEXAFS spectroscopy. Also, the product of photooxidation has high stability at elevated temperatures.

## 4.2 Viologen-based MOFs Thin Films with Highly Orientation and Photochromic Properties

### 4.2.1 Introduction

Viologen-based SURMOF is required, to avoid the characterization limitations resulting from the bulk viologen-based MOFs. The conventional solvothermal methods afforded bulk viologen-based MOFs with a closed structure.<sup>152,251,252</sup> In addition, several more advanced applications require transparent films like transient optical absorption spectroscopy.<sup>4</sup>

In the present work, viologen linkers have been assembled into-SURMOF-2 to produce a 2D crystalline structure. Exploiting the reported room temperature synthesis methods for SURMOFs to build Zn-viologen-based SURMOF, which helps in suppressing the unwanted interactions with the counter ions and the metal centers.<sup>74</sup> The assembling of viologen into SURMOF-2 afforded SURMOFs with accessible pores reverse to the reported build viologen-based MOFs.<sup>4</sup> As a result, Zn-viologen-based SURMOF is well suited to use to probe the mechanism of the electron transfer. The viologen SURMOFs were characterized with XRD, UV-Vis, IR. In addition, the photophysical properties of the viologen-based SURMOF were studied using UV-Vis, X-ray photoelectron spectroscopy (XPS), and electron paramagnetic resonances (EPR).

### 4.2.2 The structure of the linkers and the SURMOF.

The molecular structure of viologen compound and Zn-viologen based SURMOF-2 is shown in **figure4-22**.

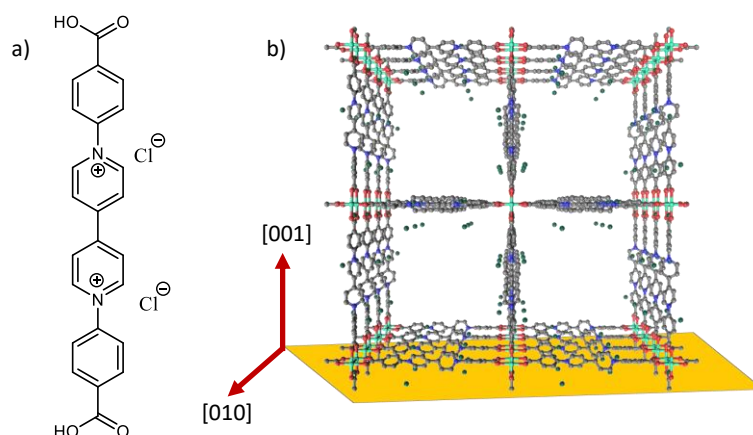


**Figure 4-22:** a) the viologen Structure; 1,1'-bis(4-carboxyphenyl)-[4,4'-bipyridine]-1,1'-dium-dichloride; b) the structure of Zn-viologen based SURMOF, (viologen compound); The red color: O; blue color: N; grey: C; green: Cl; violet color: Zn. H atoms are removed to simplify the

structure.

### 4.2.3 Synthesis and characterization of Zn-viologen based SURMOF.

Zn-viologen based SURMOF-2 samples were prepared by using a layer-by-layer- LPE approach called spray method as described in **chapter 3.10**.

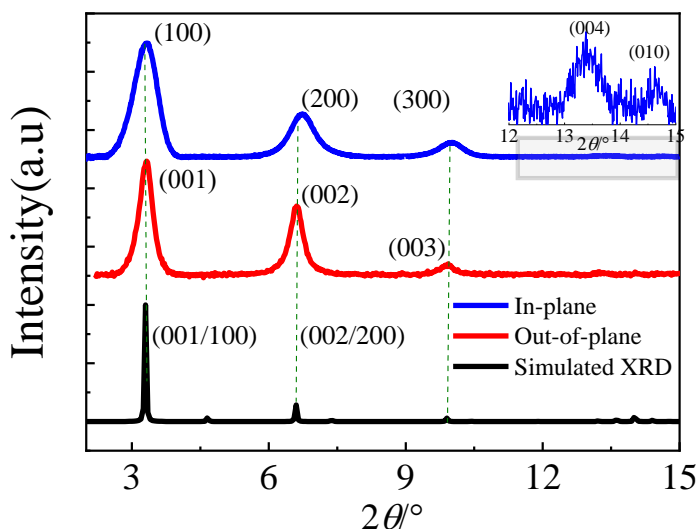


**Figure 4-23:** Simulate XRD of Zn-viologen SURMOF (black), out-of-plane XRD (red) and in-plane XRD (blue).

The structure of Zn-viologen-based SURMOF-2 was confirmed by using out-of-plane and in-plane X-ray diffraction (XRD), as shown in **figure 4-23**. The out-of-plane pattern showed that Zn-viologen-based SURMOF was highly crystalline and orientated with the [001] orientation perpendicular to the substrate. The in-plane diffraction pattern showed that the [100] and [010] orientations are oriental parallel to the substrate.<sup>84</sup> The out-of-plane XRD pattern exhibited reflexes corresponding to (001), (002) and (003) planes at  $2\theta = 3.3$ ,  $6.6$ , and  $9.9^\circ$ , respectively. The in-plane diffraction pattern showed reflexes corresponding to (100), (200), (300), and (010), planes at  $2\theta = 3.3$ ,  $6.72$ ,  $10.0$ , and  $14.54^\circ$ , respectively. The position of the [010] diffraction peak at  $14.54^\circ(2\theta)$  suggested that the interplane distance is  $6 \text{ \AA}$ . For this orientation of the SURMOFs, the 1D channels characteristic for the SURMOF-2 structure run parallel to the substrate plane. The counter-ions ( $\text{Cl}^-$ ) are hosted within these channels. These XRD data revealed that the Zn-viologen based SURMOF-2 exhibits a tetragonal cell.<sup>222</sup>

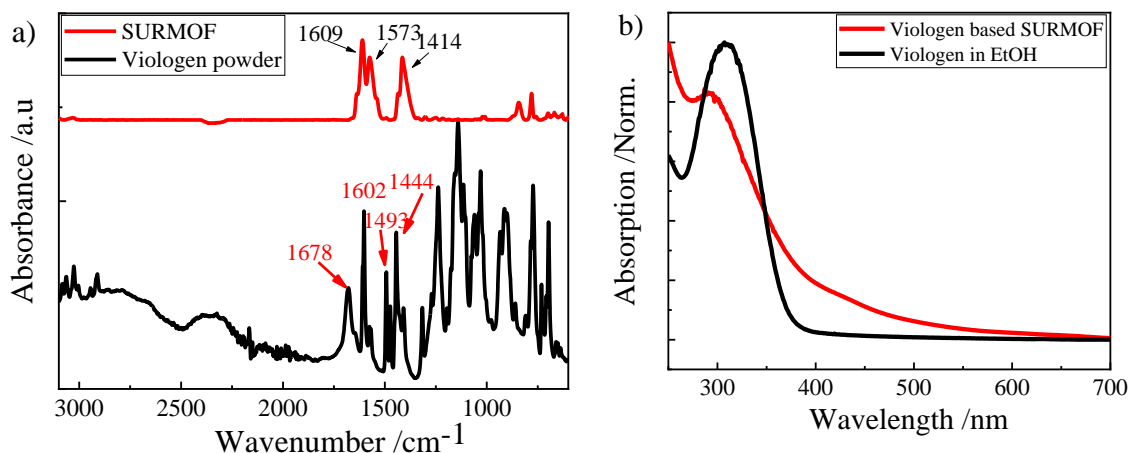


**Figure 4-24:** a) IR spectrum for the viologen linker(black), IRRAS spectrum for Zn-viologen based SURMOF-2 (red); b) UV-Vis for the pristine Zn-viologen based SURMOF-2 sample and ethanol solution of viologen compound(0.02mM).

**Figure 4-24** shows IRRAS data recorded for Zn-viologen-based SURMOF grown on (MUD SAMs) /Au substrate. The spectra revealed two-bands at  $1607\text{ cm}^{-1}$  and  $1416\text{ cm}^{-1}$ , which are attributed to asymmetric and symmetric stretching of  $\text{COO}^-$  group, respectively. The linker (viologen) showed two bands at  $1678\text{ cm}^{-1}$  and  $1602\text{ cm}^{-1}$ , which are attributed to asymmetric and symmetric stretching of the  $\text{COOH}$  group. From this result we concluded that the difference between the coordinate carboxylate and carboxylic acid ( $\Delta\nu\text{ COO}^-$ ) is around  $\sim 186\text{ cm}^{-1}$ , which resulted from the formation of Zn paddle-wheel structure.<sup>223</sup> The UV-Vis absorption spectrum of Zn-viologen based SURMOF showed a fairly sharp absorption peak due to  $n\text{-}\pi^*$  and  $\pi\text{-}\pi^*$  transition at 294 nm, while UV-Vis spectrum of the solvated viologen in ethanol showed an absorption peak at 309 nm. Furthermore, the Zn-viologen-based SURMOF exhibited a broad peak around 420 nm, which resulted from the presences of a small quantity of the radical in the pristine sample. Generally, viologen in the pristine MOFs /SURMOFs exists as a di-cation in the dark. The ( $\text{V}^{+2}$ ) species exhibit a pale-yellow color, while upon irradiation a ( $\text{V}^{+}$ ) species is generated.  $\text{V}^{+}$  is a radical and exhibits a green color or black.<sup>152,253,254</sup> From these results, we concluded that the viologen in the pristine samples exist mainly as a di-cation with a little quantity of radical. In addition, UV-Vis spectrum of Zn-viologen-based SURMOF showed a blue shift around 15 nm relative to viologen, which is attributed to the absences of solvatochromic interactions (negative solvatochromism)<sup>108</sup>, and the presence of inter-linker interactions in the SURMOF, as shown in **figure 4-24b**.

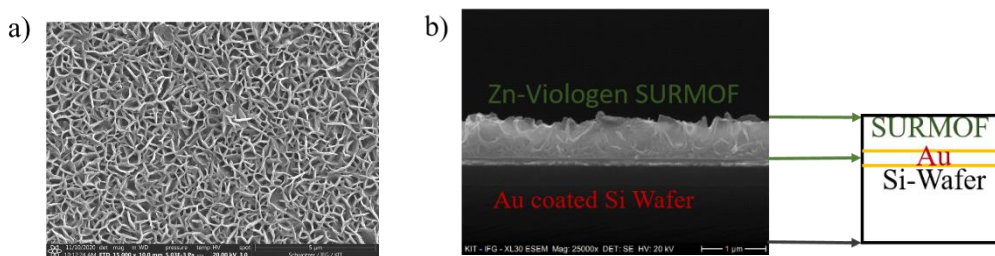


**Figure 4-25:** a) SEM top view for Zn-viologen based SURMOF-2; b) the cross-section of Zn-viologen based SURMOF.

The scanning electron microscope (SEM) shows the top view of Zn-viologen based SURMOF, micrograph reproduced in **figure4-25a**. From SEM, the Zn-viologen-based SURMOF looks like a compact, and homogenous thin-film MOF-2. In addition, the cross-section showed that the pristine Zn-viologen-based SURMOF sample is pinhole and cracks free, and showed a thickness around 400 nm. This sample was prepared using the lbl spray for 30 cycles, as shown in **figure 4-25b**. The energy-dispersive X-ray (EDX) data for Zn-viologen-based SURMOF showed that Cl<sup>-</sup> ions are presented as counterions. The amount of Cl<sup>-</sup> was roughly equal to that of N<sup>+</sup> in the SURMOF, as shown in **figure4-27**. These data showed that the chloride ions did not change to acetate ions that are the anions in the metal sources. On contrast to the reported bulk viologen based MOFs, the ions of the metal sources play a role as counter ions in the obtained bulk viologen-based MOFs.<sup>152,255–257</sup> In our case, the viologen linker is bearing two carboxylic acid group that has a higher electronegativity compared to N, or halides ions. As a result, the carboxylic group has the ability to coordinate with the metal center at the room temperature relative to halides<sup>258</sup>, as shown in **figures 4-26&4-27**.

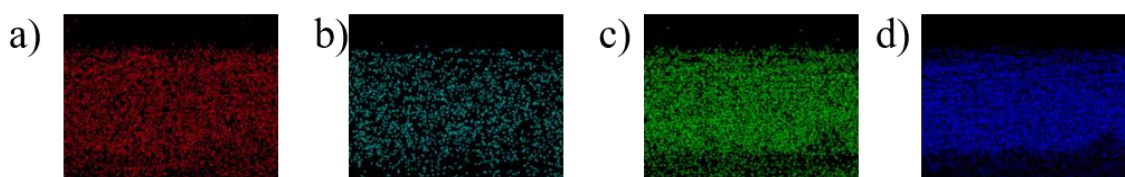


**Figure 4-26:** The map of the Zn-viologen based SURMOF, a) C in the SURMOF, b) Cl (counterion), c) O, and d) Zn element.

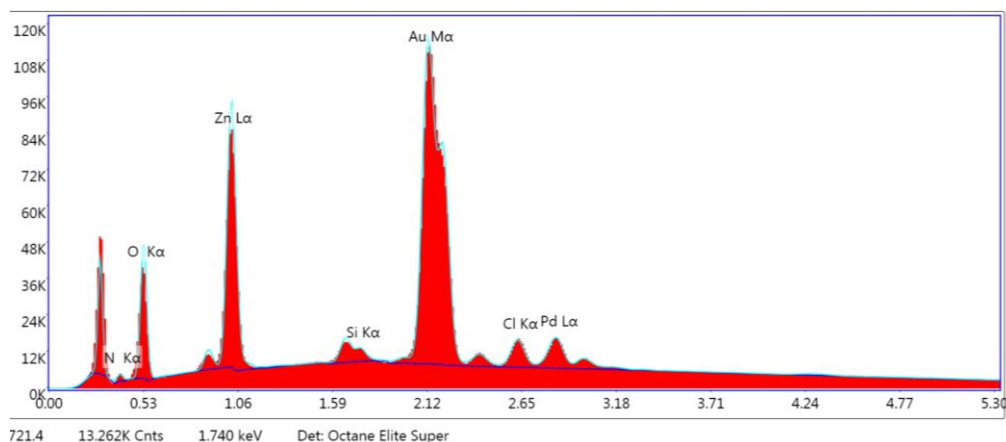


**Figure 4-27:** EDX for Zn-viologen based SURMOF.

The adsorption/desorption kinetics of the Zn-viologen-based SURMOF have been investigated using quartz crystal microbalance (QCM). Interesting, Zn-viologen-based SURMOF showed high porosity, conversely to the majority of bulk viologen-based MOFs. Because of the ionic nature of the viologen linker, the assembly of those linkers into MOFs platform via conventional (solvothermal) methods<sup>153,254,259</sup>, in many cases led to low porosity coordination polymers. The porous nature of the viologen SURMOFs studied here allowed to study the loading of aniline and phenols into the Zn-viologen-based SURMOFs. The results showed the mass uptake over the time at 30°C, after the SURMOF was reached stability via flowing N<sub>2</sub> gas for a long time, was in the range of μg, as shown in **figure 4-28**. From these result, we concluded that the Zn-viologen based SURMOF have high porosity.<sup>101,260</sup> The desorption curve of the aniline /phenols revealed that the SURMOF did not release the whole uptake mass due to the interaction between the aniline /phenols and the SURMOF.

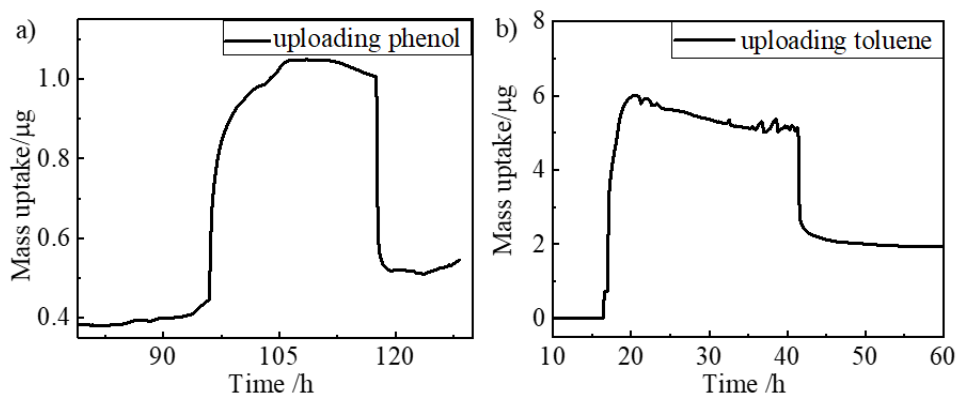


**Figure 4-28 :**Schematic diagram showing a) the mass uptake from the adsorption and desorption of phenol by Zn-viologen based SURMOF(30 cycles thin-film) at 30°C using a QCM; b) the mass



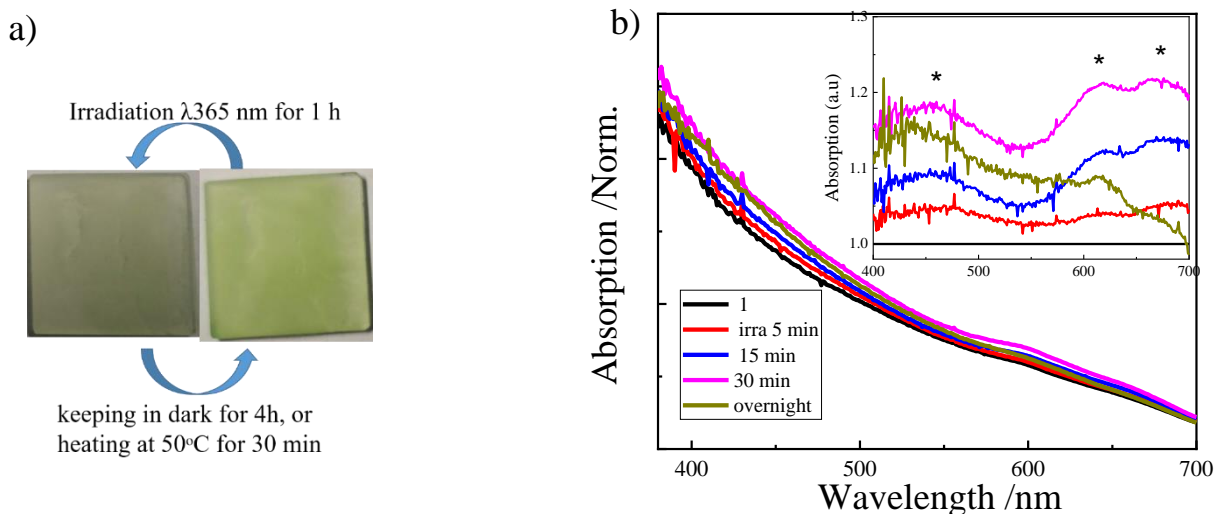


**Figure 4-29:** a) The change in the color of Zn-viologen-based SURMOF induced by irradiation under ambient conditions; b) UV-Vis spectra of Zn-viologen based-SURMOF, 1, when it was irradiated under ambient conditions for 5, 15, 30 mins, and overnight. The differences spectra were obtained by subtraction of UV-Vis of the irradiated sample from the UV-Vis of the pristine sample.

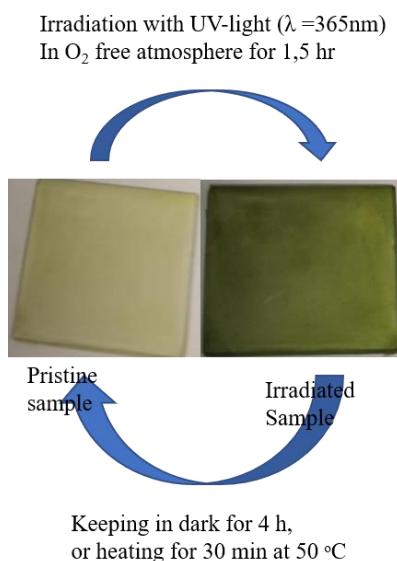


**Figure 4-30:** The picture of the pristine Zn-viologen -based SURMOF sample left, and after irradiation in the inert conditions on the right.

To understand the photochromic effect, we measured the absorption of the pristine Zn-viologen-based SURMOF sample upon irradiation under inert conditions to exclude the role of oxygen, and moisture, as shown in **figure 4-31**. The UV-Vis spectrum for the pristine sample showed only one peak around 296 nm, which is assigned to the  $\pi$ - $\pi^*$ ,  $n$ - $\pi^*$  transition from the conjugation of the

linker. In addition, a small peak was present at 420nm. After the illumination, the sample showed four new peaks at 420, 600, 650, 720 nm. These new peaks are attributed to the viologen radical,  $V^{+•}$ , produced due to the electron transfer from the electron-donor  $Cl^-$  to the electron-deficient group  $V^{2+}$  producing the bipyridinium radicals,  $V^{+•}$ .<sup>262,263</sup> The absorption intensity was observed to increase linearly with illumination time until it reached saturation after 90 mins. After switching off the light, and keeping the sample in the dark, the intensity started to decrease until the green color mostly vanished after 4 hours. The transition to the initial color could be accelerated by heating the thin-film at 50°C for 30 mins. as shown in **figures 4-32a &4-32b**.

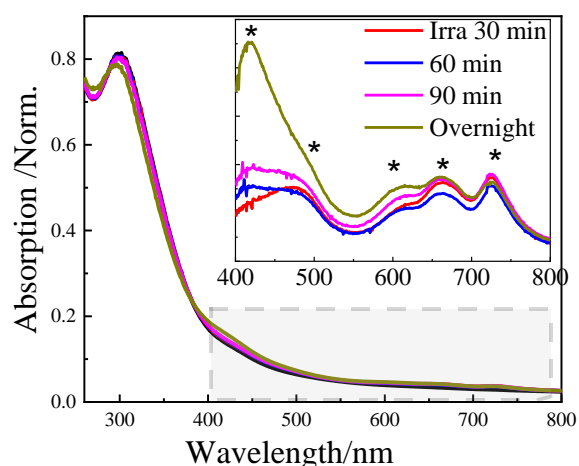


**Figure 4-31:** a) UV-Vis for Zn-viologen-based SURMOF as a pristine sample and after irradiation under inert conditions.

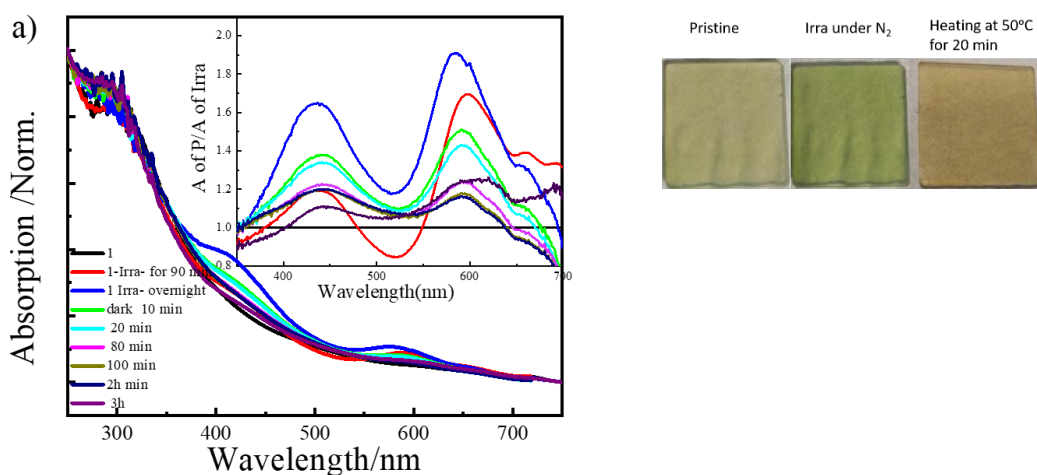


**Figure 4-32:** UV-Vis spectra of the pristine Zn-viologen-based SURMOF sample (1, black); irradiated for 1,5 h (2, red), irradiated sample overnight (1, blue); and the color transition back

within the time.; the difference spectra was obtained from subtraction of UV-Vis of the irradiated sample from the UV-Vis of the pristine sample; b) the pictures of the pristine Zn-viologen based SURMOF sample, irradiated under inert conditions, and the transition back by heating respectively.

The photochromic switching can be repeated for three cycles only, as shown in **figure 4-33**. These changes are fully consistent with the photoinduced electron transfer from  $\text{Cl}^-$  to  $\text{V}^{2+}$  and the corresponding back transfer that have been reported in the literature.<sup>262,264</sup> Interestingly, the XRD and IRRAS of the two samples which were irradiated either in the ambient conditions or in the inert conditions did not show a significant change upon irradiation. These data revealed the absences of photochemistry or photodissociation of the SURMOF which is an indication of the structure stability under illumination, as shown in **figures 4-34 a, 4-34b** for XRD, and IRRAS respectively.

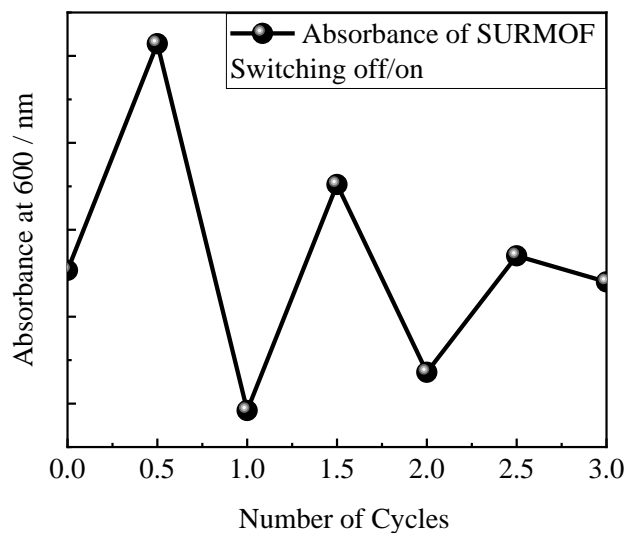


**Figure 4-33:** Change in absorption during a sequence of photoswitching cycles of Zn-viologen based SURMOF.

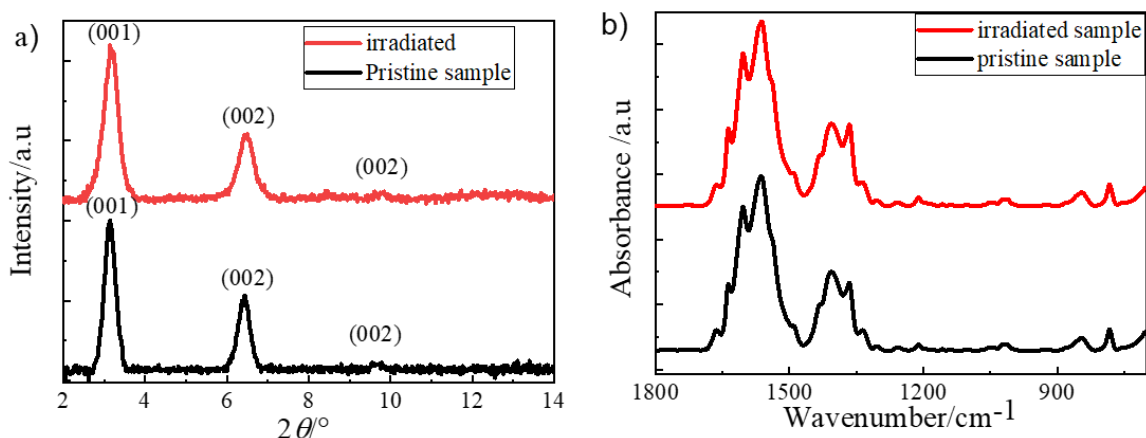


**Figure 4-34:** a) Out-of-plane XRD patterns for the pristine Zn-viologen-based SURMOF sample and after irradiation; b) IRRAS spectra for the pristine Zn-viologen based-SURMOF sample and after irradiation.

To characterize the electron transferred to the bi-pyridine  $V^{2+}$  unit, EPR measurements were recorded to demonstrate the presence of the photoinduced radicals. The pristine Zn-viologen-based SURMOF samples that were grown on Au substrates functionalized with SAMs, were also used to measure the electron magnetic resonances (EPR). EPR signals were collected for the two initial samples ambient conditions and under inert conditions, respectively. EPR has detected a small intensity signal for both samples in the dark prior to exposure. During the irradiation of the samples in situ, the signal intensity of EPR increased linearly with increasing time of the irradiation due to the continued creation of photoinduced radicals. EPR signal for the sample that was irradiated under ambient conditions increased and reduced a maximum 10 min, as shown in **figure 4-35a**. While EPR signal for the sample that was irradiated under inert conditions increased linearly with time and reached a maximum after 4.5 hours of continuous irradiation by light with a wavelength of 600 nm, as shown in **figure4-35b**. These results showed a strong interaction with the ambient conditions, mostly  $O_2$  and moisture.<sup>144,149,151,152</sup> Since the SURMOF has open pores  $O_2$  and moisture penetrate into the SURMOF and interact with radicals.

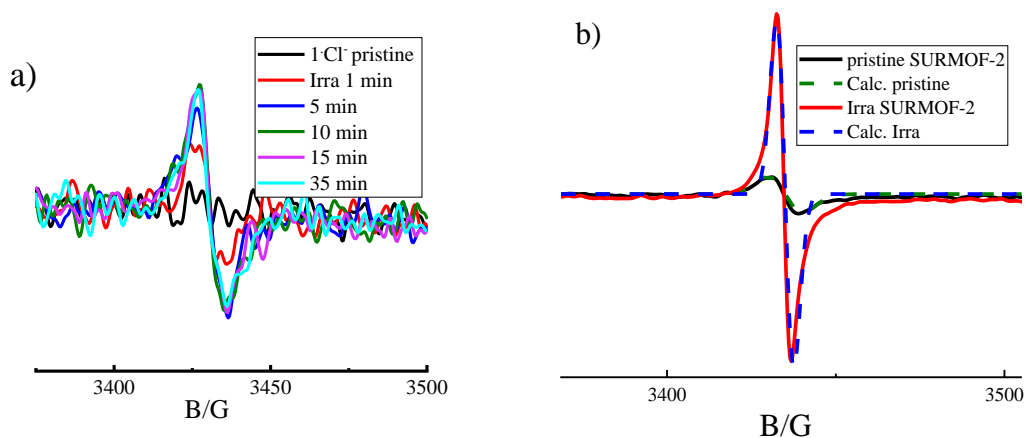


**Figure 4-35:** a) EPR recorded for Zn-viologen-based SURMOF in the pristine state and after irradiation under ambient conditions; b) EPR for Zn-viologen-based SURMOF, and after irradiation within the time in the inert conditions, pristine sample (black), and irradiated sample (red), the irradiation took place with light of a wavelength 600 nm in-situ.

X-ray photoelectron spectroscopy (XPS) was used here to analyze the pristine Zn-viologen-based SURMOF sample. In the XPS data, Zn  $2p_{3/2}$  and Zn LMM peaks were detected in Zn-viologen-based SURMOF at 1022.3 eV binding energy and 987.1 eV kinetic energy, as shown in **figures 4-36a and 4-36b**, respectively. The O1s peak showed two components with binding energy 530.6, 532.1 eV, which are assigned to C-O and C=O, respectively. The C1s signal showed three components with binding energy at 285.0 eV, 286.35 eV, and 288.95, which were assigned to C-H/C-C, C-N, and C=O, respectively, as shown in **figure 4-37**. The N1s signal and the counterions Cl 2p signal showed two and three components, respectively. This observation is attributed to the presence of a small quantity of the radicals in the pristine sample, as shown in **figure4-38**. From these results, we conclude that the viologen was almost perfectly aligned into the SURMOF platform.

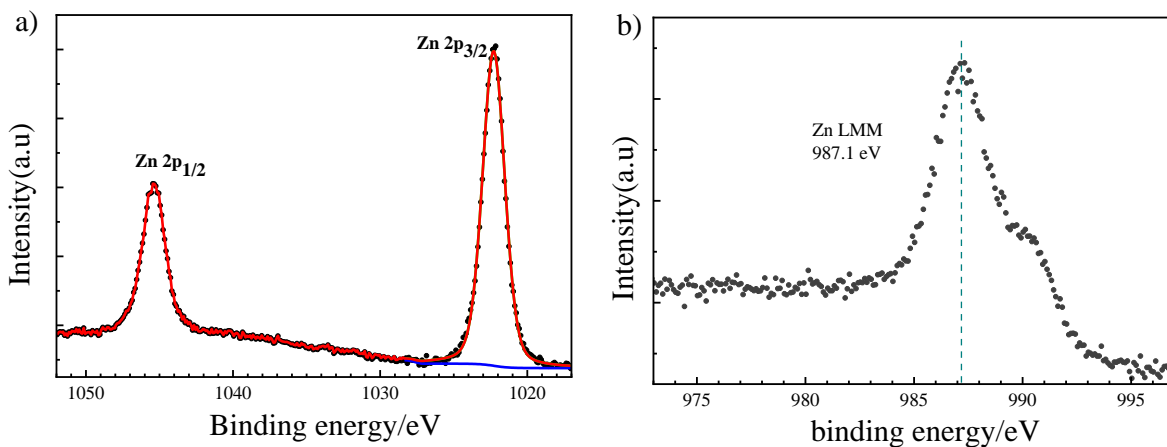


**Figure 4-36:** a) Zn 2p region; b) ZnLMM region

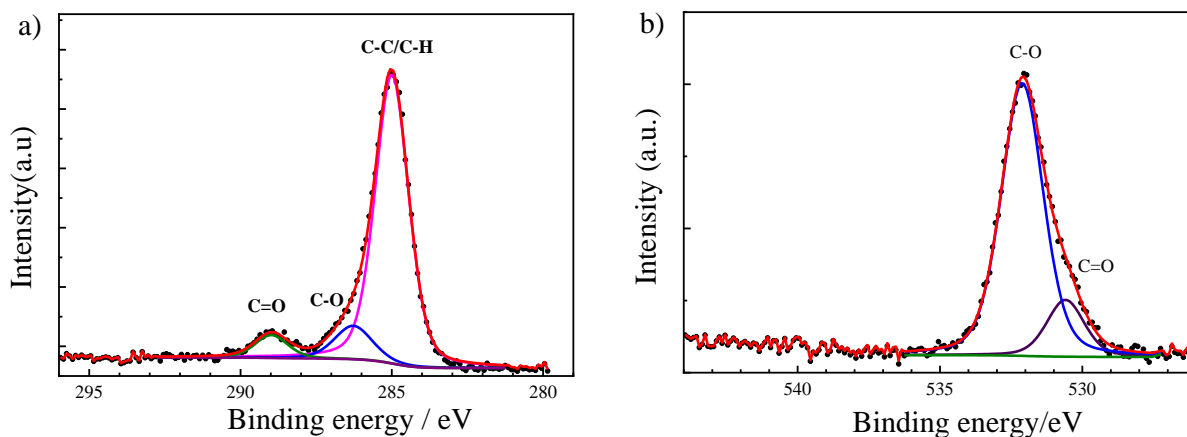


**Figure 4-37:** C1s region in the Zn-viologen-based SURMOF; b) O1s region in the Zn-viologen based SURMOF.

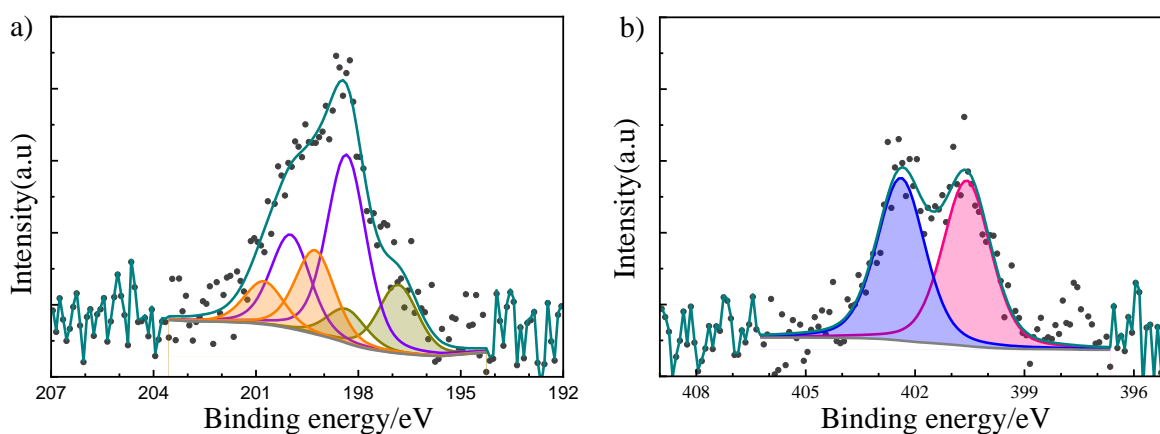


**Figure 4-38:** Cl 2p region in the pristine Zn-Viologen-based SURMOF sample, Cl; b) N 1s region in the pristine Zn-viologen based SURMOF sample.

Furthermore, XPS was used to monitor the electron transfer process. To accomplish these measurements, the XPS were recorded in the pristine Zn-viologen-based SURMOF sample and after the irradiation under in an inert atmosphere in situ. XPS results of the sample after irradiation showed that the binding energies of the Zn 2p and Zn LMM did not show any change, as shown in **figure 4-39**. Also, the O1s and C 1s signals did not show any change after irradiation, as shown in **figure 4-40**. From these results, we concluded that the metal center Zn, O 1s and the C1s were stable and did not participate in the photon-induced electron transfer process. The N 1s signal corresponding to the  $V^{2+}$  species exhibited two peaks at 400.7<sup>153</sup> (indicated in red color in N 1s spectra) and 402.5 eV.<sup>265,266</sup> Upon irradiation, the lower energy peak increased and higher energy peak decreased in intensity. The peak at 402.5 eV can be assigned to the  $V^{2+}$  state of the linker, which reduce to neutral state corresponding to the lower binding energy peak (400.7 eV), as shown in **figure 4-41**. In the case of Cl, we could identify three different states at 196.9, 198.4 and 199.3.eV. The Cl 2p<sub>3/2</sub> peak at 198.4 eV can be attributed to the counter ion Cl<sup>-</sup> and Cl 2p<sub>3/2</sub> at 199.3 eV to the oxidized Cl. In addition, the peak with lowest binding energy at 196.9 eV can be assigned to a weakly interacting state with metal center Zn<sup>2+</sup> or an anion- $\pi$  interaction. Interestingly, upon irradiation ratio of the Cl<sup>-</sup>/Cl changes from 55:25 to 40:55, as shown in **figure4-42**. The lowest binding energy of Cl 2p peak almost disappears after irradiation. These results are supporting the electron transfer from Cl<sup>-</sup> acting as electron donor to the electron deficient  $V^{2+}$ , which is accompanied by a color change.

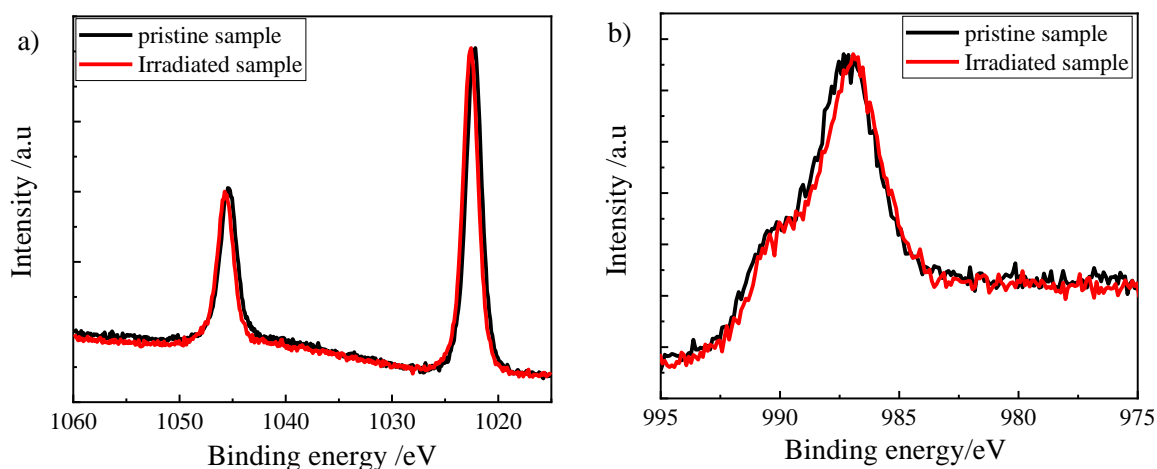


**Figure 4-39:** a) XPS data recorded for Zn in the Zn-viologen based SURMOF before and after irradiation; b) XPS data recorded for ZnLMM in Zn-viologen based SURMOF before and after irradiation.

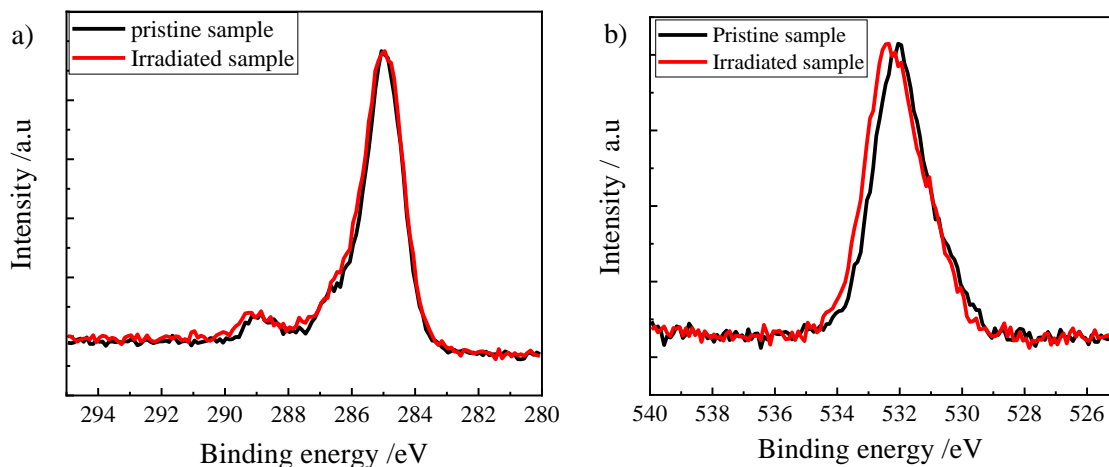


**Figure 4-40:** a) C 1s region in the Zn-viologen based SURMOF recorded before and after irradiation; b) O 1s region in the Zn-viologen based SURMOF before and after irradiation.

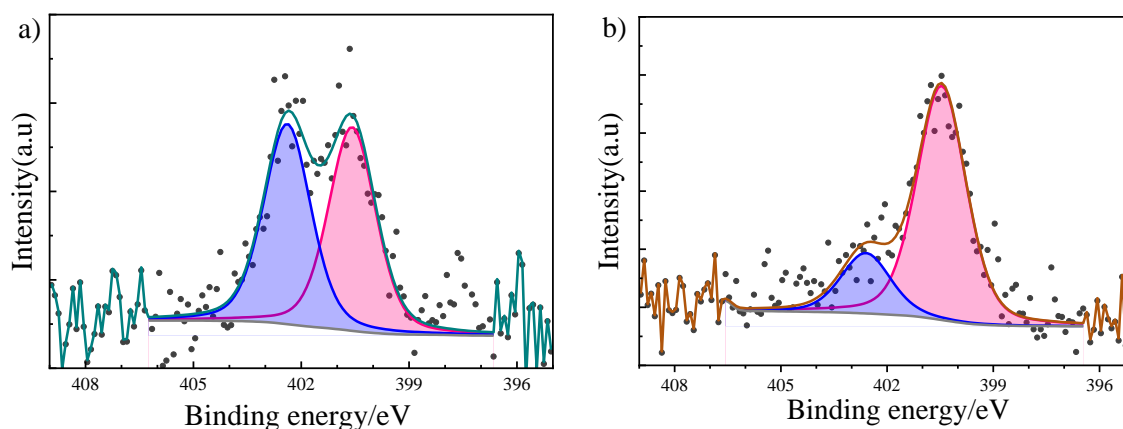


**Figure 4-41:** a) N 1s region in the pristine Zn-viologen-based SURMOF sample; b) N 1s region in the irradiated Zn-viologen-based SURMOF.

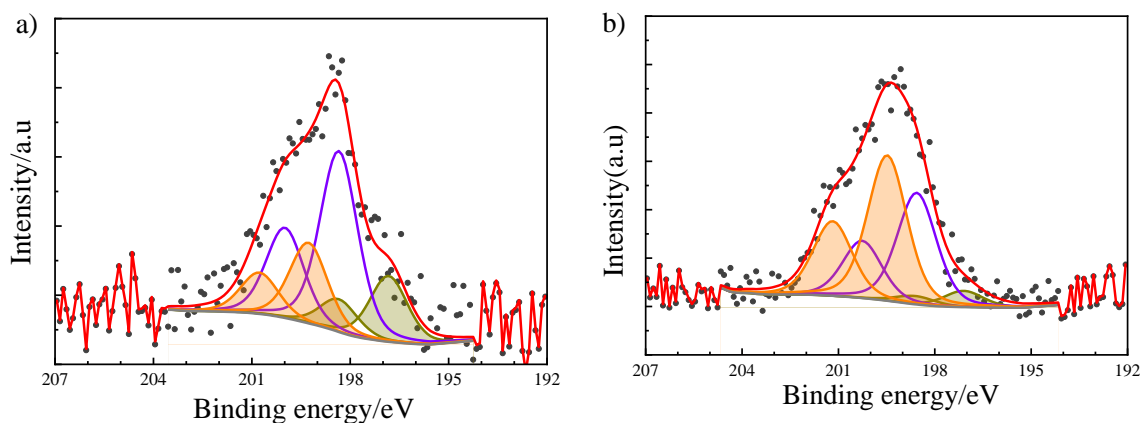


**Figure 4-42:** a) Cl 2p region in the pristine Zn-viologen-based SURMOF sample; b) Cl 2p region in the irradiated Zn-viologen-based SURMOF sample.

In general, photochromism in the bulk viologen-based MOFs takes place through intermolecular electron transfer due to the short distance between electron-deficient  $V^{2+}$  and electron donors, such as O in carboxylate group or the counterions as  $Cl^-$ ,  $N_3^-$ .<sup>149,255</sup> In our case, the photo-induced electron transfer took place between the counter-ions,  $Cl^-$ , and the electron deficient  $V^{2+}$ .

#### 4.2.5 The photoconductivity of the Zn-viologen-based SURMOF

The photoresponse of the electric conduction was explored by DC measurements, as shown in **figure 4-43**. The Zn-viologen-based SURMOF exhibited a current 0.9 pA without irradiation. The conductivity of the thin-film with a thickness of 600 nm of thickness was  $8 \text{ pS m}^{-1}$ . The electrical conductivity of the same sample increased during irradiation with two different wavelengths 455 nm and 365 nm by around two orders of magnitude to  $1 \text{ nS m}^{-1}$  and  $3 \text{ nS m}^{-1}$ , respectively. Importantly, the Zn-viologen-based SURMOF showed a higher on-off ratio than other viologen-based thin-films that have previously been reported in the literature.<sup>267,268</sup>

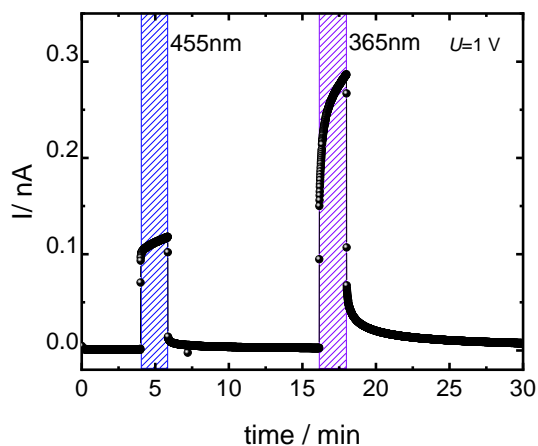


**Figure 4-43:** Current versus time recorded at a DC voltage of 1 V. The dark current is 0.9 pA. The sample is irradiated with blue and UV light for 2 min, as indicated, resulting in a current increase to  $1 \text{ nS m}^{-1}$  and  $3 \text{ nS m}^{-1}$  respectively.

#### 4.2.6 Conclusion

Viologen, as a chromophoric linker was assembled into Zn-SURMOF-2 thin-films, which produced high orientated, crystalline, and a 2D stacked chromphoric arrays. The photochromism of Zn-viologen-based SURMOF-2 showed substantial differences to these revealed for bulk viologen based MOFs. We explained these differences by the fact that the SURMOFs were prepared at room temperature, which suppressed unwanted interactions with the  $Cl^-$  counter ions

and the metal MOFs centers. As a result, the majority of the carboxylate groups coordinated to Zn-metal centers yielding a higher order MOF thin-film. Then, the photoinduced electron transfer took place between chloride ion (a counter ion) and pyridinium dication (deficient group). The photo-induced electron transfer produced,  $V^{+\bullet}$  a radical that was accompanied by a color change for the Zn-viologen-based SURMOF. The change in the color was detected using UV-Vis and the presences of the radicals by EPR. In addition, the experiments showed that the photochromism of Zn-viologen-based SURMOF has a shorter lifetime in comparison with the reported bulk viologen-based MOFs.

## 5 Conclusion

The present thesis shows the alignment of the chromophoric linkers /molecules into the SURMOF-2 platform. Different types of chromophoric SURMOF-2 system were prepared by using the layer-by-layer method via the liquid phase epitaxy approach. This technique produces highly crystalline, monolithic, homogenous thin films with controllable thickness. The alignment of the chromophoric linkers into the SURMOF-2 platform enabled studying the photophysical properties of those chromophoric linkers. The chromophoric compounds have a wide variety of potential applications in different fields.

**In Chapter (4.1)**, the synthesized bianthryl linker has been assembled into the SURMOF-2 platform by using zinc acetate as the source for the metal node, which afforded Zn-bianthryl based MOF thin-films. The assembly of bianthryl in SURMOF-2 yielded a close-packed, highly crystalline, orientated 2D stacked structure. The luminescence of the highly orientated Zn-bianthryl-based SURMOF-2 was studied, which demonstrated the presences of cyano-color upon short time illuminating using ultraviolet (UV) light. In addition, prolonged illumination under ambient conditions switched off the luminescence. The experiments showed that Zn-bianthryl based SURMOF-2 was able to convert triplet oxygen,  $^3\text{O}_2$ , to singlet oxygen,  $^1\text{O}_2$ , which was detected using indirect methods such as photolysis of the DPBF compound and using the EPR technique. The produced  $^1\text{O}_2$  reacted with one anthracene moiety of bi-anthracene, resulting in the formation of endoperoxide. The experiments showed that the formed endoperoxide was stable at elevated temperature. The Zn-endoperoxide-based SURMOF did not lose crystallinity compared to the pristine material.

**Chapter (4.2)** showed the assembly of another chromophoric linker, viologen (1,1'-bis (4-(carboxylic acid) phenyl)-[4,4'-bipyridine]-1,1'-dium dichloride), into MOF thin-films. Zinc acetate was used as a source for the metal center. The experiments showed that the obtained Zn-viologen-based SURMOFs were high crystalline, orientated, and had a 2D stacked structure. The photochromism was studied for Zn-viologen-based SURMOF-2, which exhibited a color change upon irradiation under ambient as well as under inert conditions. The color changed due to photoinduced electron-transfer from a counter ion,  $\text{Cl}^-$  acting as an electron donor, to the electron-deficient group  $\text{V}^{2+}$ . The change in color was detected using UV-Vis spectroscopy, EPR, and XPS. The presences of  $\text{O}_2$  and  $\text{H}_2\text{O}$ , played a role in the initial color transition. In addition, heating the samples, which existed in the radical's states at  $50\text{ }^\circ\text{C}$  for 20 min has been used to accelerated the color transition back to the initial state.

## 6 Abbreviation

2D	two-dimensional
ATR	attenuated total reflection
3D	Three-dimensional
AFM	atomic force microscopy
BTC	1,3,5-benzenetricarboxylic acid
EDX	Energy-dispersive X-ray
FT-IR	Fourier Transform Infrared
HKUST-1	Hong Kong University of Science and Technology-1
MOFs	metal-organic frameworks
SURMOFs	Surface inched metal-organic frameworks
SBU	secondary building units
OBU	organic building unite /linker
sTTA	sensitized triplet-triplet annihilation
IRRAS	infrared reflection absorption spectroscopy
MHDA	16-mercaptohexadecanoic acid
PPP1	(4-(4-pyridyl) phenyl)-methanethiol
MUD	11-mercapto-1-undecanol
UV	ultraviolet
QCM	quartz crystal microbalance
SAM	self-assembled monolayer
SEM	scanning electron microscope
THF	Tetrahydrofuran
UV-Vis	ultraviolet-visible spectroscopy
XPS	X-ray photoelectron spectroscopy
XRD	X-ray diffraction
LbL	The layer-by-layer
LPE	liquid-phase epitaxy
EPR	electron paramagnetic resonance
PCPs	porous coordination polymers

PCNs	porous coordination networks
MOF-5	isoreticular metal organic framework-1 (IRMOF-1)
CVD	chemical vapor deposition
ALD	atomic layer deposition
ECF	electrochemical fabrication
BMA	bottom-up modular assembly
SSH	substrate-seeded heteroepitaxy
TPMTA	4'-carboxyterphenyl-4-methane-thiol
CMMT	9-carboxy-10(mercapto -methyl) triptycene
bdc	benzene-1,4-dicarboxylic acid
ZIF-8	zeolitic imidazolate frameworks
MIL	Matériaux de l'Institut Lavoisier
NDI	naphthalene diimide derivatives
DMF	N, N-dimethylformamide
CD-MOF	Cyclodextrin-metal-organic framework
DSM	(4-p-(dimethylamino) styryl)-1-methylpyridinium iodide
DCM	4-(dicyanomethylene)-2-methyl-6-(p-dimethylaminostyryl)-4H-pyran
ISC	intersystem crossing by electrons
Pd-H <sub>2</sub> DCP	pd-porphyrin derivatives
ADB	4,4'-(anthracene-9,10-diyl)dibenzoic acid
TPPS	5,10,15,20-tetrakis(4-sulfonatophenyl) porphyrin (TPPS)
So-PCN	(singlet oxygen-generating porous coordination network
DTE	dithienylethene
BPDTE	1,2-bis(2-methyl-5-(pyridin-4-yl)thiophen-3-yl) cyclopent-1-ene
TEM	Transmission electron microscopy
SAXS	Small-angle X-ray scattering
NEXAFS	Near-edge X-ray absorption fine structure spectroscopy
(TCSPC),	time-correlated single-photon counting
ADB-COOCH <sub>3</sub>	dimethyl-4,4'-(anthracene-9,10-diyl) dibenzoate
TLC	Thin layer chromatography

NMR	Nuclear magnetic resonance
$\text{CDCl}_3$	Deuterated chloroform
ppm.	Parts per million
$\text{DMSO-d}_6$	Dimethyl sulfoxide-d6
bianthrylCOOCH <sub>3</sub>	Dimethyl 4,4'-([9,9'-bianthracene]-10,10'-diyl) dibenzoate
bianthryl	4,4'-([9,9'-bianthracene]-10,10'-diyl) dibenzoic acid
C-C ADB-CH <sub>3</sub>	Dimethyl-4,4'-(anthracene-9,10-diylbis(ethyne-2,1-diyl)) dibenzoate
C-C ADB	4,4'-(anthracene-9,10-diylbis(ethyne-2,1-diyl)) dibenzoic acid
HOMO	highest occupied molecular orbital
LUMO	unoccupied molecular orbital
TEMP	2,2,6,6-Tetramethylpiperidine
TEMPO	2,2,6,6-Tetramethyl-1-piperidinyloxy
DMPO	(5,5-dimethyl-1-pyrroline-n-oxide)
DPBF	1,3-diphenylisobenzofuran
TBAPF <sub>6</sub>	Tertiarybutylammonium hexafluorophosphate
LC-MS	Liquid chromatography–mass spectrometry
DPBF	1,3-Diphenylisobenzofuran

## 7 References

- (1) Furukawa, H.; Cordova, K. E.; O’Keeffe, M.; Yaghi, O. M. The Chemistry and Applications of Metal-Organic Frameworks. *Science*. American Association for the Advancement of Science August 2013, pp 1230444–1230444. <https://doi.org/10.1126/science.1230444>.
- (2) Eddaoudi, M.; Moler, D. B.; Li, H.; Chen, B.; Reineke, T. M.; O’Keeffe, M.; Yaghi, O. M. Modular Chemistry: Secondary Building Units as a Basis for the Design of Highly Porous and Robust Metal-Organic Carboxylate Frameworks. *Acc. Chem. Res.* **2001**, *34* (4), 319–330. <https://doi.org/10.1021/ar000034b>.
- (3) Heo, D. Y.; Do, H. H.; Ahn, S. H.; Kim, S. Y. Metal-Organic Framework Materials for Perovskite Solar Cells. *Polymers (Basel)*. **2020**, *12* (9), 2061. <https://doi.org/10.3390/POLYM12092061>.
- (4) Haldar, R.; Heinke, L.; Wöll, C. Advanced Photoresponsive Materials Using the Metal–Organic Framework Approach. *Adv. Mater.* **2020**, *32*, 1905227. <https://doi.org/10.1002/adma.201905227>.
- (5) O’Keeffe, M.; Eddaoudi, M.; Li, -Hailian; Reineke, T.; Yaghi, O. M. Frameworks for Extended Solids: Geometrical Design Principles. *J. Solid State Chem.* **2000**, *152* (1), 3–20. <https://doi.org/10.1006/jssc.2000.8723>.
- (6) Han, X.; Yang, S.; Schröder, M. Porous Metal–Organic Frameworks as Emerging Sorbents for Clean Air. *Nature Reviews Chemistry*. Nature Publishing Group February 1, 2019, pp 108–118. <https://doi.org/10.1038/s41570-019-0073-7>.
- (7) Chanut, N.; Ghoufi, A.; Coulet, M. V.; Bourrelly, S.; Kuchta, B.; Maurin, G.; Llewellyn, P. L. Tailoring the Separation Properties of Flexible Metal-Organic Frameworks Using Mechanical Pressure. *Nat. Commun.* **2020**, *11* (1), 1216. <https://doi.org/10.1038/s41467-020-15036-y>.
- (8) Rowsell, J. L. C.; Yaghi, O. M. Metal-Organic Frameworks: A New Class of Porous Materials. *Microporous and Mesoporous Materials*. Elsevier 2004, pp 3–14. <https://doi.org/10.1016/j.micromeso.2004.03.034>.
- (9) Kalmutzki, M. J.; Diercks, C. S.; Yaghi, O. M. Metal–Organic Frameworks for Water Harvesting from Air. *Advanced Materials*. Wiley-VCH Verlag 2018, p 1704304. <https://doi.org/10.1002/adma.201704304>.
- (10) Dhakshinamoorthy, A.; Li, Z.; Garcia, H. Catalysis and Photocatalysis by Metal Organic

- Frameworks. *Chemical Society Reviews*. Royal Society of Chemistry 2018, pp 8134–8172. <https://doi.org/10.1039/c8cs00256h>.
- (11) Emam, H. E.; Abdelhamid, H. N.; Abdelhameed, R. M. Self-Cleaned Photoluminescent Viscose Fabric Incorporated Lanthanide-Organic Framework (Ln-MOF). *Dye. Pigment*. **2018**, *159*, 491–498. <https://doi.org/10.1016/j.dyepig.2018.07.026>.
- (12) Diercks, C. S.; Liu, Y.; Cordova, K. E.; Yaghi, O. M. The Role of Reticular Chemistry in the Design of CO<sub>2</sub> Reduction Catalysts. *Nat. Mater.* **2018**, *17* (4), 301–307. <https://doi.org/10.1038/s41563-018-0033-5>.
- (13) Baumann, A. E.; Burns, D. A.; Liu, B.; Thoi, V. S. Metal-Organic Framework Functionalization and Design Strategies for Advanced Electrochemical Energy Storage Devices. *Communications Chemistry*. Springer Nature 2019, pp 1–14. <https://doi.org/10.1038/s42004-019-0184-6>.
- (14) Chidambaram, A.; Stylianou, K. C. Electronic Metal-Organic Framework Sensors. *Inorganic Chemistry Frontiers*. Royal Society of Chemistry 2018, pp 979–998. <https://doi.org/10.1039/c7qi00815e>.
- (15) Yang, Y.; Shen, K.; Lin, J.; Zhou, Y.; Liu, Q.; Hang, C.; Abdelhamid, H. N.; Zhang, Z.; Chen, H. A Zn-MOF Constructed from Electron-Rich  $\pi$ -Conjugated Ligands with an Interpenetrated Graphene-like Net as an Efficient Nitroaromatic Sensor. *RSC Adv.* **2016**, *6* (51), 45475–45481. <https://doi.org/10.1039/C6RA00524A>.
- (16) Cui, Y.; Zhang, J.; He, H.; Qian, G. Photonic Functional Metal-Organic Frameworks. *Chemical Society Reviews*. Royal Society of Chemistry 2018, pp 5740–5785. <https://doi.org/10.1039/c7cs00879a>.
- (17) Wang, S.; McGuirk, C. M.; d’Aquino, A.; Mason, J. A.; Mirkin, C. A. Metal–Organic Framework Nanoparticles. *Advanced Materials*. Wiley-VCH Verlag September 13, 2018, p 1800202. <https://doi.org/10.1002/adma.201800202>.
- (18) Chen, W.; Wu, C. Synthesis, Functionalization, and Applications of Metal-Organic Frameworks in Biomedicine. *Dalton Transactions*. Royal Society of Chemistry 2018, pp 2114–2133. <https://doi.org/10.1039/c7dt04116k>.
- (19) Abdelhamid, H. N.; Zou, X. Template-Free and Room Temperature Synthesis of Hierarchical Porous Zeolitic Imidazolate Framework Nanoparticles and Their Dye and CO<sub>2</sub> Sorption. *Green Chem.* **2018**, *20* (5), 1074–1084. <https://doi.org/10.1039/c7gc03805d>.

- (20) Abdelhamid, H. N.; Bermejo-Gómez, A.; Martín-Matute, B.; Zou, X. A Water-Stable Lanthanide Metal-Organic Framework for Fluorimetric Detection of Ferric Ions and Tryptophan. *Microchim. Acta* **2017**, *184* (9), 3363–3371. <https://doi.org/10.1007/s00604-017-2306-0>.
- (21) Abdelhamid, H. N.; Huang, Z.; El-Zohry, A. M.; Zheng, H.; Zou, X. A Fast and Scalable Approach for Synthesis of Hierarchical Porous Zeolitic Imidazolate Frameworks and One-Pot Encapsulation of Target Molecules. *Inorg. Chem.* **2017**, *56* (15), 9139–9146. <https://doi.org/10.1021/acs.inorgchem.7b01191>.
- (22) Abdelhamid, H. N. Lanthanide Metal-Organic Frameworks and Hierarchical Porous Zeolitic Imidazolate Frameworks: Synthesis, Properties, and Applications, Stockholm University, Faculty of Science, Stockholm, 2017. <https://doi.org/oai:DiVA.org:su-146398>.
- (23) Lin, R. B.; Xiang, S.; Li, B.; Cui, Y.; Qian, G.; Zhou, W.; Chen, B. Our Journey of Developing Multifunctional Metal-Organic Frameworks. *Coordination Chemistry Reviews*. Elsevier B.V. 2019, pp 21–36. <https://doi.org/10.1016/j.ccr.2019.01.009>.
- (24) Schoedel, A.; Yaghi, O. M. Reticular Chemistry of Metal-Organic Frameworks Composed of Copper and Zinc Metal Oxide Secondary Building Units as Nodes. In *The Chemistry of Metal-Organic Frameworks: Synthesis, Characterization, and Applications*; Wiley-VCH Verlag GmbH & Co. KGaA: Weinheim, Germany, 2016; pp 41–72. <https://doi.org/10.1002/9783527693078.ch3>.
- (25) Ma, S.; Sun, D.; Ambrogio, M.; Fillinger, J. A.; Parkin, S.; Zhou, H. C. Framework-Catenation Isomerism in Metal-Organic Frameworks and Its Impact on Hydrogen Uptake. *J. Am. Chem. Soc.* **2007**, *129* (7), 1858–1859. <https://doi.org/10.1021/ja067435s>.
- (26) Lee, Y. G.; Moon, H. R.; Cheon, Y. E.; Suh, M. P. A Comparison of the H<sub>2</sub> Sorption Capacities of Isostructural Metal-Organic Frameworks with and without Accessible Metal Sites: [ $\text{Zn}_2(\text{Abtc})(\text{Dmf})_2$ ]<sub>3</sub> and [ $\text{Cu}_2(\text{Abtc})(\text{Dmf})_2$ ]<sub>3</sub> versus [ $\text{Cu}_2(\text{Abtc})$ ]<sub>3</sub>. *Angew. Chemie - Int. Ed.* **2008**, *47* (40), 7741–7745. <https://doi.org/10.1002/anie.200801488>.
- (27) Feldblyum, J. I.; Liu, M.; Gidley, D. W.; Matzger, A. J. Reconciling the Discrepancies between Crystallographic Porosity and Guest Access as Exemplified by Zn-HKUST-1. *J. Am. Chem. Soc.* **2011**, *133* (45), 18257–18263. <https://doi.org/10.1021/ja2055935>.
- (28) Loiseau, T.; Férey, G. Crystalline Oxyfluorinated Open-Framework Compounds: Silicates, Metal Phosphates, Metal Fluorides and Metal-Organic Frameworks (MOF). *Journal of*

*Fluorine Chemistry*. Elsevier 2007, pp 413–422.  
<https://doi.org/10.1016/j.jfluchem.2006.09.009>.

- (29) Van Niekerk, J. N.; Schoening, F. R. L. X-Ray Evidence for Metal-to-Metal Bonds in Cupric and Chromous Acetate [5]. *Nature*. Nature Publishing Group 1953, pp 36–37.  
<https://doi.org/10.1038/171036a0>.
- (30) Eddaoudi, M.; Kim, J.; Rosi, N.; Vodak, D.; Wachter, J.; O’Keeffe, M.; Yaghi, O. M. Systematic Design of Pore Size and Functionality in Isorecticular MOFs and Their Application in Methane Storage. *Science* (80-. ). **2002**, 295 (5554), 469–472.  
<https://doi.org/10.1126/science.1067208>.
- (31) Ploetz, E.; Engelke, H.; Lächelt, U.; Wuttke, S. The Chemistry of Reticular Framework Nanoparticles: MOF, ZIF, and COF Materials. *Adv. Funct. Mater.* **2020**, 1909062.  
<https://doi.org/10.1002/adfm.201909062>.
- (32) Lu, W.; Wei, Z.; Gu, Z. Y.; Liu, T. F.; Park, J.; Park, J.; Tian, J.; Zhang, M.; Zhang, Q.; Gentle, T.; Bosch, M.; Zhou, H. C. Tuning the Structure and Function of Metal-Organic Frameworks via Linker Design. *Chemical Society Reviews*. Royal Society of Chemistry 2014, pp 5561–5593. <https://doi.org/10.1039/c4cs00003j>.
- (33) Butova, V. V.; Soldatov, M. A.; Guda, A. A.; Lomachenko, K. A.; Lamberti, C. Metal-Organic Frameworks: Structure, Properties, Methods of Synthesis and Characterization. *Russ. Chem. Rev.* **2016**, 85 (3), 280–307. <https://doi.org/10.1070/RCR4554>.
- (34) Yao, Q.; Bermejo Gómez, A.; Su, J.; Pascanu, V.; Yun, Y.; Zheng, H.; Chen, H.; Liu, L.; Abdelhamid, H. N.; Martín-Matute, B.; Zou, X. Series of Highly Stable Isorecticular Lanthanide Metal–Organic Frameworks with Expanding Pore Size and Tunable Luminescent Properties. *Chem. Mater.* **2015**, 27 (15), 5332–5339. <https://doi.org/10.1021/acs.chemmater.5b01711>.
- (35) Zou, X.; Yao, Q.; Gómez, A. B.; Su, J.; Pascanu, V.; Yun, Y.; Zheng, H.; Chen, H.; Liu, L.; Abdelhamid, H. N.; Martín-Matute, B. A Series of Highly Stable Isorecticular Lanthanide Metal-Organic Frameworks with Tunable Luminescence Properties Solved by Rotation Electron Diffraction and X-Ray Diffraction. *Acta Crystallogr. Sect. A Found. Adv.* **2016**, 72 (a1), s136–s136. <https://doi.org/10.1107/S2053273316097977>.
- (36) Horcajada, P.; Chalati, T.; Serre, C.; Gillet, B.; Sebrie, C.; Baati, T.; Eubank, J. F.; Heurtaux, D.; Clayette, P.; Kreuz, C.; Chang, J. S.; Hwang, Y. K.; Marsaud, V.; Bories, P. N.; Cynober, L.; Gil, S.; Férey, G.; Couvreur, P.; Gref, R. Porous Metal-Organic-Framework Nanoscale

- Carriers as a Potential Platform for Drug Delivery and Imaging. *Nat. Mater.* **2010**, *9* (2), 172–178. <https://doi.org/10.1038/nmat2608>.
- (37) Abdelhamid, H. N.; Wu, H.-F. Nanoparticles Advanced Drug Delivery for Cancer Cells. In *Nanoparticulate Drug Delivery Systems*; Keservani, R. K., Sharma, A. K., Eds.; 2019; pp 121–144.
- (38) Abdelhamid, H. N.; Dowaidar, M.; Langel, Ü. Carbonized Chitosan Encapsulated Hierarchical Porous Zeolitic Imidazolate Frameworks Nanoparticles for Gene Delivery. *Microporous Mesoporous Mater.* **2020**. <https://doi.org/10.1016/j.micromeso.2020.110200>.
- (39) Abdelhamid, H. N.; Dowaidar, M.; Hällbrink, M.; Langel, Ü. Gene Delivery Using Cell Penetrating Peptides-Zeolitic Imidazolate Frameworks. *Microporous Mesoporous Mater.* **2020**, *300*, 110173. <https://doi.org/10.1016/j.micromeso.2020.110173>.
- (40) Abdelhamid, H. N.; Dowaidar, M.; Hällbrink, M.; Langel, Ü. Cell Penetrating Peptides-Hierarchical Porous Zeolitic Imidazolate Frameworks Nanoparticles: An Efficient Gene Delivery Platform. *SSRN Electron. J.* **2019**. <https://doi.org/10.2139/ssrn.3435895>.
- (41) Lismont, M.; Dreesen, L.; Wuttke, S. Metal-Organic Framework Nanoparticles in Photodynamic Therapy: Current Status and Perspectives. *Advanced Functional Materials*. Wiley-VCH Verlag 2017, p 1606314. <https://doi.org/10.1002/adfm.201606314>.
- (42) Zhu, W.; Liu, Y.; Yang, Z.; Zhang, L.; Xiao, L.; Liu, P.; Wang, J.; Yi, C.; Xu, Z.; Ren, J. Albumin/Sulfonamide Stabilized Iron Porphyrin Metal Organic Framework Nanocomposites: Targeting Tumor Hypoxia by Carbonic Anhydrase IX Inhibition and: T<sub>1</sub>-T<sub>2</sub> Dual Mode MRI Guided Photodynamic/Photothermal Therapy. *J. Mater. Chem. B* **2018**, *6* (2), 265–276. <https://doi.org/10.1039/c7tb02818k>.
- (43) Wang, Y.; Liu, H.; Jiang, W.; Wang, Q.; Hang, L.; Wang, Y. ROS-Sensitive Biomimetic Nanocarriers Modulate Tumor Hypoxia for Synergistic Photodynamic Chemotherapy. *Biomater. Sci.* **2019**, *7* (9), 3706–3716. <https://doi.org/10.1039/c9bm00634f>.
- (44) Chen, L.; Duan, B.; Luo, Q.; Gu, Z.; Liu, J.; Duan, C. Facet-Dependent Catalytic Activity of ZIF-8 Nanocubes and Rhombic Dodecahedra Based on Tracing Substrate Diffusion in Pores by SERS: A Case Study for Surface Catalysis of MOFs. *Catal. Sci. Technol.* **2016**, *6* (6), 1616–1620. <https://doi.org/10.1039/c5cy01882j>.
- (45) Dey, C.; Kundu, T.; Biswal, B. P.; Mallick, A.; Banerjee, R. Crystalline Metal-Organic Frameworks (MOFs): Synthesis, Structure and Function. *Acta Crystallogr. Sect. B Struct. Sci.*

- Cryst. Eng. Mater.* **2014**, *70* (1), 3–10. <https://doi.org/10.1107/S2052520613029557>.
- (46) Ma, S.; Zhou, H. C. Gas Storage in Porous Metal-Organic Frameworks for Clean Energy Applications. *Chemical Communications*. The Royal Society of Chemistry 2010, pp 44–53. <https://doi.org/10.1039/b916295j>.
- (47) Abdelhamid, H. N. Zinc Hydroxide Nitrate Nanosheets Conversion into Hierarchical Zeolitic Imidazolate Frameworks Nanocomposite and Their Application for CO<sub>2</sub> Sorption. *Mater. Today Chem.* **2020**, *15*, 100222. <https://doi.org/10.1016/j.mtchem.2019.100222>.
- (48) Abdelhamid, H. N. Salts Induced Formation of Hierarchical Porous ZIF-8 and Their Applications for CO<sub>2</sub> Sorption and Hydrogen Generation via NaBH<sub>4</sub> Hydrolysis. *Macromol. Chem. Phys.* **2020**, *221* (7), 2000031. <https://doi.org/10.1002/macp.202000031>.
- (49) Abdel-Magied, A. F.; Abdelhamid, H. N.; Ashour, R. M.; Zou, X.; Forsberg, K. Hierarchical Porous Zeolitic Imidazolate Frameworks Nanoparticles for Efficient Adsorption of Rare-Earth Elements. *Microporous Mesoporous Mater.* **2019**, *278*, 175–184. <https://doi.org/10.1016/j.micromeso.2018.11.022>.
- (50) He, C.; Wang, Y.; Chen, Y.; Wang, X.; Yang, J.; Li, L.; Li, J. Direct Functionalization of the Open Metal Sites in Rare Earth-Based Metal–Organic Frameworks Used for the Efficient Separation of Ethylene. *Ind. Eng. Chem. Res.* **2020**, *59* (13), 6123–6129. <https://doi.org/10.1021/acs.iecr.9b06765>.
- (51) Goda, M. N.; Abdelhamid, H. N.; Said, A. E. A. A. Zirconium Oxide Sulfate-Carbon (ZrOSO<sub>4</sub>@C) Derived from Carbonized UiO-66 for Selective Production of Dimethyl Ether. *ACS Appl. Mater. Interfaces* **2020**, *12* (1), 646–653. <https://doi.org/10.1021/acsami.9b17520>.
- (52) Abdelhamid, H. N. Hierarchical Porous ZIF-8 for Hydrogen Production via the Hydrolysis of Sodium Borohydride. *Dalt. Trans.* **2020**, *49* (14), 4416–4424. <https://doi.org/10.1039/d0dt00145g>.
- (53) Abdelhamid, H. N.; El-Zohry, A. M.; Cong, J.; Thersleff, T.; Karlsson, M.; Kloo, L.; Zou, X. Towards Implementing Hierarchical Porous Zeolitic Imidazolate Frameworks in Dye-Sensitized Solar Cells. *R. Soc. Open Sci.* **2019**, *6* (7), 190723. <https://doi.org/10.1098/rsos.190723>.
- (54) Kassem, A. A.; Abdelhamid, H. N.; Fouad, D. M.; Ibrahim, S. A. Metal-Organic Frameworks (MOFs) and MOFs-Derived CuO@C for Hydrogen Generation from Sodium Borohydride. *Int. J. Hydrogen Energy* **2019**, *44* (59), 31230–31238.

<https://doi.org/10.1016/j.ijhydene.2019.10.047>.

- (55) Abdelhamid, H. N.; Wilk-Kozubek, M.; El-Zohry, A. M.; Bermejo Gómez, A.; Valiente, A.; Martín-Matute, B.; Mudring, A. V.; Zou, X. Luminescence Properties of a Family of Lanthanide Metal-Organic Frameworks. *Microporous Mesoporous Mater.* **2019**, *279*, 400–406. <https://doi.org/10.1016/j.micromeso.2019.01.024>.
- (56) Abdelhamid, H. N. Nanoparticles Assisted Laser Desorption/Ionization Mass Spectrometry. In *Handbook of Smart Materials in Analytical Chemistry*; John Wiley & Sons, Ltd: Chichester, UK, 2019; pp 729–755. <https://doi.org/10.1002/9781119422587.ch23>.
- (57) Suslick, K. S.; Bhyrappa, P.; Chou, J. H.; Kosal, M. E.; Nakagaki, S.; Smithenry, D. W.; Wilson, S. R. Microporous Porphyrin Solids. *Acc. Chem. Res.* **2005**, *38* (4), 283–291. <https://doi.org/10.1021/ar040173j>.
- (58) Alkhatib, I. I.; Garlisi, C.; Pagliaro, M.; Al-Ali, K.; Palmisano, G. Metal-Organic Frameworks for Photocatalytic CO<sub>2</sub> Reduction under Visible Radiation: A Review of Strategies and Applications. *Catalysis Today*. Elsevier B.V. 2020, pp 209–224. <https://doi.org/10.1016/j.cattod.2018.09.032>.
- (59) Ethiraj, J.; Albanese, E.; Civalleri, B.; Vitillo, J. G.; Bonino, F.; Chavan, S.; Shearer, G. C.; Lillerud, K. P.; Bordiga, S. Carbon Dioxide Adsorption in Amine-Functionalized Mixed-Ligand Metal-Organic Frameworks of UiO-66 Topology. *ChemSusChem* **2014**, *7* (12), 3382–3388. <https://doi.org/10.1002/cssc.201402694>.
- (60) Sumida, K.; Rogow, D. L.; Mason, J. A.; McDonald, T. M.; Bloch, E. D.; Herm, Z. R.; Bae, T.-H.; Long, J. R. Carbon Dioxide Capture in Metal–Organic Frameworks. *Chem. Rev.* **2012**, *112* (2), 724–781. <https://doi.org/10.1021/cr2003272>.
- (61) Abdelhamid, H. N. Surfactant Assisted Synthesis of Hierarchical Porous Metal-Organic Frameworks Nanosheets. *Nanotechnology* **2019**, *30* (43), 435601. <https://doi.org/10.1088/1361-6528/ab30f6>.
- (62) Liu, J.; Wöll, C. Surface-Supported Metal-Organic Framework Thin Films: Fabrication Methods, Applications, and Challenges. *Chemical Society Reviews*. 2017, pp 5730–5770. <https://doi.org/10.1039/c7cs00315c>.
- (63) Meng, J.; Liu, X.; Niu, C.; Pang, Q.; Li, J.; Liu, F.; Liu, Z.; Mai, L. Advances in Metal–Organic Framework Coatings: Versatile Synthesis and Broad Applications. *Chem. Soc. Rev.* **2020**. <https://doi.org/10.1039/C9CS00806C>.

- (64) Stassen, I.; Styles, M.; Greci, G.; Van Gorp, H.; Vanderlinden, W.; De Feyter, S.; Falcaro, P.; De Vos, D.; Vereecken, P.; Ameloot, R. Chemical Vapour Deposition of Zeolitic Imidazolate Framework Thin Films. *Nat. Mater.* **2016**, *15* (3), 304–310. <https://doi.org/10.1038/nmat4509>.
- (65) George, S. M. Atomic Layer Deposition: An Overview. *Chem. Rev.* **2010**, *110* (1), 111–131. <https://doi.org/10.1021/cr900056b>.
- (66) Zhao, Y.; Kornienko, N.; Liu, Z.; Zhu, C.; Asahina, S.; Kuo, T. R.; Bao, W.; Xie, C.; Hexemer, A.; Terasaki, O.; Yang, P.; Yaghi, O. M. Mesoscopic Constructs of Ordered and Oriented Metal-Organic Frameworks on Plasmonic Silver Nanocrystals. *J. Am. Chem. Soc.* **2015**, *137* (6), 2199–2202. <https://doi.org/10.1021/ja512951e>.
- (67) Haraguchi, T.; Otsubo, K.; Sakata, O.; Kawaguchi, S.; Fujiwara, A.; Kitagawa, H. A Three-Dimensional Accordion-like Metal-Organic Framework: Synthesis and Unconventional Oriented Growth on a Surface. *Chem. Commun.* **2016**, *52* (35), 6017–6020. <https://doi.org/10.1039/c6cc00056h>.
- (68) Hod, I.; Bury, W.; Karlin, D. M.; Deria, P.; Kung, C. W.; Katz, M. J.; So, M.; Klahr, B.; Jin, D.; Chung, Y. W.; Odom, T. W.; Farha, O. K.; Hupp, J. T. Directed Growth of Electroactive Metal-Organic Framework Thin Films Using Electrophoretic Deposition. *Adv. Mater.* **2014**, *26* (36), 6295–6300. <https://doi.org/10.1002/adma.201401940>.
- (69) Mauk, M. G. Liquid-Phase Epitaxy. In *Handbook of Crystal Growth: Thin Films and Epitaxy: Second Edition*; 2015. <https://doi.org/10.1016/B978-0-444-63304-0.00006-8>.
- (70) Li, J. R.; Kuppler, R. J.; Zhou, H. C. Selective Gas Adsorption and Separation in Metal-Organic Frameworks. *Chem. Soc. Rev.* **2009**, *38* (5), 1477–1504. <https://doi.org/10.1039/b802426j>.
- (71) Kreno, L. E.; Leong, K.; Farha, O. K.; Allendorf, M.; Van Duyne, R. P.; Hupp, J. T. Metal-Organic Framework Materials as Chemical Sensors. *Chemical Reviews*. American Chemical Society 2012, pp 1105–1125. <https://doi.org/10.1021/cr200324t>.
- (72) Allendorf, M. D.; Schwartzberg, A.; Stavila, V.; Talin, A. A. A Roadmap to Implementing Metal-Organic Frameworks in Electronic Devices: Challenges and Critical Directions. *Chem. - A Eur. J.* **2011**, *17* (41), 11372–11388. <https://doi.org/10.1002/chem.201101595>.
- (73) Liu, J.; Zhou, W.; Liu, J.; Fujimori, Y.; Higashino, T.; Imahori, H.; Jiang, X.; Zhao, J.; Sakurai, T.; Hattori, Y.; Matsuda, W.; Seki, S.; Garlapati, S. K.; Dasgupta, S.; Redel, E.; Sun, L.; Wöll, C. A New Class of Epitaxial Porphyrin Metal-Organic Framework Thin Films with Extremely High Photocarrier Generation Efficiency: Promising Materials for All-Solid-State Solar Cells.

- J. Mater. Chem. A* **2016**, *4* (33), 12739–12747. <https://doi.org/10.1039/c6ta04898f>.
- (74) Gliemann, H.; Wöll, C. Epitaxially Grown Metal-Organic Frameworks. *Materials Today*. March 2012, pp 110–116. [https://doi.org/10.1016/S1369-7021\(12\)70046-9](https://doi.org/10.1016/S1369-7021(12)70046-9).
- (75) Gu, Z. G.; Zhang, J. Epitaxial Growth and Applications of Oriented Metal–Organic Framework Thin Films. *Coordination Chemistry Reviews*. Elsevier B.V. 2019, pp 513–532. <https://doi.org/10.1016/j.ccr.2017.09.028>.
- (76) Shekhah, O.; Wang, H.; Zacher, D.; Fischer, R. A.; Wöll, C. Growth Mechanism of Metal-Organic Frameworks: Insights into the Nucleation by Employing a Step-by-Step Route. *Angew. Chemie - Int. Ed.* **2009**, *48* (27), 5038–5041. <https://doi.org/10.1002/anie.200900378>.
- (77) Shekhah, O.; Wang, H.; Kowarik, S.; Schreiber, F.; Paulus, M.; Tolan, M.; Sternemann, C.; Evers, F.; Zacher, D.; Fischer, R. A.; Wöll, C. Step-by-Step Route for the Synthesis of Metal-Organic Frameworks. *J. Am. Chem. Soc.* **2007**, *129* (49), 15118–15119. <https://doi.org/10.1021/ja076210u>.
- (78) Munuera, C.; Shekhah, O.; Wang, H.; Wöll, C.; Ocal, C. The Controlled Growth of Oriented Metal-Organic Frameworks on Functionalized Surfaces as Followed by Scanning Force Microscopy. *Phys. Chem. Chem. Phys.* **2008**, *10* (48), 7257–7261. <https://doi.org/10.1039/b811010g>.
- (79) St. Petkov, P.; Vayssilov, G. N.; Liu, J.; Shekhah, O.; Wang, Y.; Wöll, C.; Heine, T. Defects in MOFs: A Thorough Characterization. *ChemPhysChem* **2012**, *13* (8), 2025–2029. <https://doi.org/10.1002/cphc.201200222>.
- (80) Arslan, H. K.; Shekhah, O.; Wohlgemuth, J.; Franzreb, M.; Fischer, R. A.; Wöll, C. High-Throughput Fabrication of Uniform and Homogenous MOF Coatings. *Adv. Funct. Mater.* **2011**, *21* (22), 4228–4231. <https://doi.org/10.1002/adfm.201101592>.
- (81) Chernikova, V.; Shekhah, O.; Eddaoudi, M. Advanced Fabrication Method for the Preparation of MOF Thin Films: Liquid-Phase Epitaxy Approach Meets Spin Coating Method. *ACS Appl. Mater. Interfaces* **2016**, *8* (31), 20459–20464. <https://doi.org/10.1021/acsami.6b04701>.
- (82) Gu, Z. G.; Pfriem, A.; Hamsch, S.; Breitwieser, H.; Wohlgemuth, J.; Heinke, L.; Gliemann, H.; Wöll, C. Transparent Films of Metal-Organic Frameworks for Optical Applications. *Microporous Mesoporous Mater.* **2015**, *211*, 82–87. <https://doi.org/10.1016/j.micromeso.2015.02.048>.
- (83) Stavila, V.; Volponi, J.; Katzenmeyer, A. M.; Dixon, M. C.; Allendorf, M. D. Kinetics and

- Mechanism of Metal-Organic Framework Thin Film Growth: Systematic Investigation of HKUST-1 Deposition on QCM Electrodes. *Chem. Sci.* **2012**, *3* (5), 1531–1540. <https://doi.org/10.1039/c2sc20065a>.
- (84) Arslan, H. K.; Shekhah, O.; Wieland, D. C. F.; Paulus, M.; Sternemann, C.; Schroer, M. A.; Tiemeyer, S.; Tolan, M.; Fischer, R. A.; Wöll, C. Intercalation in Layered Metal-Organic Frameworks: Reversible Inclusion of an Extended  $\pi$ -System. *J. Am. Chem. Soc.* **2011**, *133* (21), 8158–8161. <https://doi.org/10.1021/ja2037996>.
- (85) Maya, F.; Palomino Cabello, C.; Clavijo, S.; Estela, J. M.; Cerdà, V.; Turnes Palomino, G. Automated Growth of Metal-Organic Framework Coatings on Flow-through Functional Supports. *Chem. Commun.* **2015**, *51* (38), 8169–8172. <https://doi.org/10.1039/c5cc01186h>.
- (86) Heinke, L.; Tu, M.; Wannapaiboon, S.; Fischer, R. A.; Wöll, C. Surface-Mounted Metal-Organic Frameworks for Applications in Sensing and Separation. *Microporous Mesoporous Mater.* **2014**, *216*, 200–215. <https://doi.org/10.1016/j.micromeso.2015.03.018>.
- (87) Kung, C. W.; Mondloch, J. E.; Wang, T. C.; Bury, W.; Hoffeditz, W.; Klahr, B. M.; Klet, R. C.; Pellin, M. J.; Farha, O. K.; Hupp, J. T. Metal-Organic Framework Thin Films as Platforms for Atomic Layer Deposition of Cobalt Ions to Enable Electrocatalytic Water Oxidation. *ACS Appl. Mater. Interfaces* **2015**, *7* (51), 28223–28230. <https://doi.org/10.1021/acsami.5b06901>.
- (88) Denny, M. S.; Cohen, S. M. In Situ Modification of Metal-Organic Frameworks in Mixed-Matrix Membranes. *Angew. Chemie - Int. Ed.* **2015**, *54* (31), 9029–9032. <https://doi.org/10.1002/anie.201504077>.
- (89) Campbell, J.; Székely, G.; Davies, R. P.; Braddock, D. C.; Livingston, A. G. Fabrication of Hybrid Polymer/Metal Organic Framework Membranes: Mixed Matrix Membranes versus in Situ Growth. *J. Mater. Chem. A* **2014**, *2* (24), 9260–9271. <https://doi.org/10.1039/c4ta00628c>.
- (90) Shekhah, O.; Wang, H.; Strunskus, T.; Cyganik, P.; Zacher, D.; Fischer, R.; Wöll, C. Layer-by-Layer Growth of Oriented Metal Organic Polymers on a Functionalized Organic Surface. *Langmuir* **2007**, *23* (14), 7440–7442. <https://doi.org/10.1021/la701148z>.
- (91) Wasson, M. C.; Buru, C. T.; Kirlikovali, K. O.; Farha, O. K. Illuminating a Practical Solution to Clothing Protection from Mustard Gas. *Matter* **2020**, *2* (2), 286–287. <https://doi.org/10.1016/j.matt.2020.01.009>.
- (92) Silvestre, M. E.; Franzreb, M.; Weidler, P. G.; Shekhah, O.; Wöll, C. Magnetic Cores with Porous Coatings: Growth of Metal-Organic Frameworks on Particles Using Liquid Phase

- Epitaxy. *Adv. Funct. Mater.* **2013**, *23* (9), 1210–1213. <https://doi.org/10.1002/adfm.201202078>.
- (93) Kind, M.; Wöll, C. Organic Surfaces Exposed by Self-Assembled Organothiols Monolayers: Preparation, Characterization, and Application. *Progress in Surface Science*. 2009, pp 230–278. <https://doi.org/10.1016/j.progsurf.2009.06.001>.
- (94) Lessel, M.; Bäumchen, O.; Klos, M.; Hähl, H.; Fetzer, R.; Paulus, M.; Seemann, R.; Jacobs, K. Self-Assembled Silane Monolayers: An Efficient Step-by-Step Recipe for High-Quality, Low Energy Surfaces. *Surf. Interface Anal.* **2015**, *47* (5), 557–564. <https://doi.org/10.1002/sia.5729>.
- (95) Wang, M.; Liechti, K. M.; Wang, Q.; White, J. M. Self-Assembled Silane Monolayers: Fabrication with Nanoscale Uniformity. *Langmuir* **2005**, *21* (5), 1848–1857. <https://doi.org/10.1021/la048483y>.
- (96) Liu, J.; Shekhah, O.; Stammer, X.; Arslan, H. K.; Liu, B.; Schüpbach, B.; Terfort, A.; Wöll, C. Deposition of Metal-Organic Frameworks by Liquid-Phase Epitaxy: The Influence of Substrate Functional Group Density on Film Orientation. *Materials (Basel)*. **2012**, *5* (9), 1581–1592. <https://doi.org/10.3390/ma5091581>.
- (97) Sauerbrey, G. Verwendung von Schwingquarzen Zur Wägung Dünner Schichten Und Zur Mikrowägung. *Zeitschrift für Phys.* **1959**, *155* (2), 206–222. <https://doi.org/10.1007/BF01337937>.
- (98) Biemmi, E.; Darga, A.; Stock, N.; Bein, T. Direct Growth of  $\text{Cu}_3(\text{BTC})_2(\text{H}_2\text{O})_3 \cdot \text{XH}_2\text{O}$  Thin Films on Modified QCM-Gold Electrodes - Water Sorption Isotherms. *Microporous Mesoporous Mater.* **2008**, *114* (1–3), 380–386. <https://doi.org/10.1016/j.micromeso.2008.01.024>.
- (99) Huang, C. Y.; Song, M.; Gu, Z. Y.; Wang, H. F.; Yan, X. P. Probing the Adsorption Characteristic of Metal-Organic Framework MIL-101 for Volatile Organic Compounds by Quartz Crystal Microbalance. *Environ. Sci. Technol.* **2011**, *45* (10), 4490–4496. <https://doi.org/10.1021/es200256q>.
- (100) Song, L. F.; Jiang, C. H.; Jiao, C. L.; Zhang, J.; Sun, L. X.; Xu, F.; You, W. S.; Wang, Z. G.; Zhao, J. J. Two New Metal-Organic Frameworks with Mixed Ligands of Carboxylate and Bipyridine: Synthesis, Crystal Structure, and Sensing for Methanol. *Cryst. Growth Des.* **2010**, *10* (12), 5020–5023. <https://doi.org/10.1021/cg100599z>.
- (101) Zybalyo, O.; Shekhah, O.; Wang, H.; Tafipolsky, M.; Schmid, R.; Johannsmann, D.; Wöll, C.

- A Novel Method to Measure Diffusion Coefficients in Porous Metal-Organic Frameworks. *Phys. Chem. Chem. Phys.* **2010**, *12* (28), 8092–8097. <https://doi.org/10.1039/b927601g>.
- (102) Shekhah, O. Layer-by-Layer Method for the Synthesis and Growth of Surface Mounted Metal-Organic Frameworks (SURMOFs). *Materials (Basel)*. **2010**, *3* (2), 1302–1315. <https://doi.org/10.3390/ma3021302>.
- (103) Yaghi, O. M.; Li, G.; Li, H. Selective Binding and Removal of Guests in a Microporous Metal-Organic Framework. *Nature* **1995**. <https://doi.org/10.1038/378703a0>.
- (104) Shevchenko, A. P.; Alexandrov, E. V.; Golov, A. A.; Blatova, O. A.; Duyunova, A. S.; Blatov, V. A. Topology: Versus Porosity: What Can Reticular Chemistry Tell Us about Free Space in Metal-Organic Frameworks? *Chem. Commun.* **2020**. <https://doi.org/10.1039/d0cc04004e>.
- (105) Danowski, W.; Van Leeuwen, T.; Browne, W. R.; Feringa, B. L. Photoresponsive Porous Materials. *Nanoscale Advances*. 2021. <https://doi.org/10.1039/d0na00647e>.
- (106) Rice, A. M.; Martin, C. R.; Galitskiy, V. A.; Berseneva, A. A.; Leith, G. A.; Shustova, N. B. Photophysics Modulation in Photoswitchable Metal-Organic Frameworks. *Chemical Reviews*. American Chemical Society 2020, pp 8790–8813. <https://doi.org/10.1021/acs.chemrev.9b00350>.
- (107) Martin, C. R.; Kittikhunnatham, P.; Leith, G. A.; Berseneva, A. A.; Park, K. C.; Greytak, A. B.; Shustova, N. B. Let the Light Be a Guide: Chromophore Communication in Metal-Organic Frameworks. **2019**. <https://doi.org/10.1007/s12274-020-3017-0>.
- (108) Schwartz, H. A.; Ruschewitz, U. Photoactive Molecules within MOFs; Springer, Berlin, Heidelberg, 2020; pp 1–49. [https://doi.org/10.1007/430\\_2020\\_56](https://doi.org/10.1007/430_2020_56).
- (109) Feringa, B. L. The Art of Building Small: From Molecular Switches to Molecular Motors. *Journal of Organic Chemistry*. American Chemical Society 2007, pp 6635–6652. <https://doi.org/10.1021/jo070394d>.
- (110) Orgiu, E.; Samorì, P. 25th Anniversary Article: Organic Electronics Marries Photochromism: Generation of Multifunctional Interfaces, Materials, and Devices. *Advanced Materials*. Wiley-VCH Verlag 2014, pp 1827–1845. <https://doi.org/10.1002/adma.201304695>.
- (111) Tomatsu, I.; Peng, K.; Kros, A. Photoresponsive Hydrogels for Biomedical Applications. *Advanced Drug Delivery Reviews*. Elsevier 2011, pp 1257–1266. <https://doi.org/10.1016/j.addr.2011.06.009>.
- (112) Irie, M.; Fukaminato, T.; Matsuda, K.; Kobatake, S. Photochromism of Diarylethene Molecules

- and Crystals: Memories, Switches, and Actuators. *Chemical Reviews*. American Chemical Society 2014, pp 12174–12277. <https://doi.org/10.1021/cr500249p>.
- (113) Kawata, S.; Kawata, Y. Three-Dimensional Optical Data Storage Using Photochromic Materials. *Chem. Rev.* **2000**, *100* (5), 1777–1788. <https://doi.org/10.1021/cr980073p>.
- (114) Qin, M.; Huang, Y.; Li, F.; Song, Y. Photochromic Sensors: A Versatile Approach for Recognition and Discrimination. *J. Mater. Chem. C* **2015**, *3* (36), 9265–9275. <https://doi.org/10.1039/c5tc01939g>.
- (115) Grosjean, S.; Hodapp, P.; Hassan, Z.; Wöll, C.; Nieger, M.; Bräse, S. Synthesis of Functionalized Azobiphenyl- and Azoterphenyl- Ditopic Linkers: Modular Building Blocks for Photoresponsive Smart Materials. *ChemistryOpen* **2019**. <https://doi.org/10.1002/open.201900031>.
- (116) Yang, X.; Lin, X.; Zhao, Y. S.; Yan, D. Recent Advances in Micro-/Nanostructured Metal-Organic Frameworks towards Photonic and Electronic Applications. *Chem. - A Eur. J.* **2018**, *24* (25), 6484–6493. <https://doi.org/10.1002/chem.201704650>.
- (117) Castellanos, S.; Kapteijn, F.; Gascon, J. Photoswitchable Metal Organic Frameworks: Turn on the Lights and Close the Windows. *CrystEngComm* **2016**, *18* (22), 4006–4012. <https://doi.org/10.1039/c5ce02543e>.
- (118) Liu, X.; Kozłowska, M.; Okkali, T.; Wagner, D.; Higashino, T.; Brenner-Weiß, G.; Marschner, S. M.; Fu, Z.; Zhang, Q.; Imahori, H.; Bräse, S.; Wenzel, W.; Wöll, C.; Heinke, L. Photoconductivity in Metal–Organic Framework (MOF) Thin Films. *Angew. Chemie Int. Ed.* **2019**, *58* (28), 9590–9595. <https://doi.org/10.1002/anie.201904475>.
- (119) Dolgoplova, E. A.; Rice, A. M.; Martin, C. R.; Shustova, N. B. Photochemistry and Photophysics of MOFs: Steps towards MOF-Based Sensing Enhancements. *Chemical Society Reviews*. 2018. <https://doi.org/10.1039/c7cs00861a>.
- (120) Nguyen, T. N.; Ebrahim, F. M.; Stylianou, K. C. Photoluminescent, Upconversion Luminescent and Nonlinear Optical Metal-Organic Frameworks: From Fundamental Photophysics to Potential Applications. *Coordination Chemistry Reviews*. Elsevier B.V. 2018, pp 259–306. <https://doi.org/10.1016/j.ccr.2018.08.024>.
- (121) Zhuang, Z.; Liu, D. Conductive MOFs with Photophysical Properties: Applications and Thin-Film Fabrication. *Nano-Micro Letters*. Springer 2020, pp 1–32. <https://doi.org/10.1007/s40820-020-00470-w>.

- (122) Gong, Y.; Wu, T.; Lin, J. Metal-Organic Frameworks Based on Naphthalene-1,5-Diylldioxy-Di-Acetate: Structures, Topologies, Photoluminescence and Photocatalytic Properties. *CrystEngComm* **2012**, *14* (10), 3727–3736. <https://doi.org/10.1039/c2ce06529k>.
- (123) Scheurle, P. I.; Mähringer, A.; Jakowetz, A. C.; Hosseini, P.; Richter, A. F.; Wittstock, G.; Medina, D. D.; Bein, T. A Highly Crystalline Anthracene-Based MOF-74 Series Featuring Electrical Conductivity and Luminescence †. **2019**. <https://doi.org/10.1039/c9nr05431f>.
- (124) Firmino, A. D. G.; Mendes, R. F.; Ananias, D.; Figueira, F.; Tomé, J. P. C.; Rocha, J.; Almeida Paz, F. A. Pyrene Tetrakisphosphonate-Based Metal-Organic Framework: Structure and Photoluminescence. *Eur. J. Inorg. Chem.* **2020**, *2020* (37), 3565–3572. <https://doi.org/10.1002/ejic.202000726>.
- (125) Son, H. J.; Jin, S.; Patwardhan, S.; Wezenberg, S. J.; Jeong, N. C.; So, M.; Wilmer, C. E.; Sarjeant, A. A.; Schatz, G. C.; Snurr, R. Q.; Farha, O. K.; Wiederrecht, G. P.; Hupp, J. T. Light-Harvesting and Ultrafast Energy Migration in Porphyrin-Based Metal-Organic Frameworks. *J. Am. Chem. Soc.* **2013**. <https://doi.org/10.1021/ja310596a>.
- (126) Heinke, L. Diffusion and Photoswitching in Nanoporous Thin Films of Metal-Organic Frameworks. *Journal of Physics D: Applied Physics*. Institute of Physics Publishing April 19, 2017, p 193004. <https://doi.org/10.1088/1361-6463/aa65f8>.
- (127) Tu, M.; Reinsch, H.; Rodríguez-Hermida, S.; Verbeke, R.; Stassin, T.; Egger, W.; Dickmann, M.; Dieu, B.; Hofkens, J.; Vankelecom, I.; Stock, N.; Ameloot, R. Reversible Optical Writing and Data Storage in an Anthracene-Loaded Metal-Organic Framework. *Angew. Chemie* **2018**, 2445–2449. <https://doi.org/10.1002/ange.201813996>.
- (128) Ye, J. W.; Zhou, H. L.; Liu, S. Y.; Cheng, X. N.; Lin, R. B.; Qi, X. L.; Zhang, J. P.; Chen, X. M. Encapsulating Pyrene in a Metal-Organic Zeolite for Optical Sensing of Molecular Oxygen. *Chem. Mater.* **2015**, *27* (24), 8255–8260. <https://doi.org/10.1021/acs.chemmater.5b03955>.
- (129) Maity, K.; Mukherjee, D.; Sen, M.; Biradha, K. Fluorescent Dye-Based Metal-Organic Framework Piezochromic and Multicolor-Emitting Two-Dimensional Materials for Light-Emitting Devices. *ACS Appl. Nano Mater.* **2019**, *2* (3), 1614–1620. <https://doi.org/10.1021/acsanm.9b00055>.
- (130) Rowe, J. M.; Soderstrom, E. M.; Zhu, J.; Usov, P. M.; Morris, A. J. Synthesis, Characterization, and Luminescent Properties of Two New Zr(IV) Metal-Organic Frameworks Based on Anthracene Derivatives. *Can. J. Chem.* **2018**, *96* (9), 875–880. <https://doi.org/10.1139/cjc->

2017-0445.

- (131) Lustig, W. P.; Mukherjee, S.; Rudd, N. D.; Desai, A. V.; Li, J.; Ghosh, S. K. Metal-Organic Frameworks: Functional Luminescent and Photonic Materials for Sensing Applications. *Chemical Society Reviews*. Royal Society of Chemistry 2017, pp 3242–3285. <https://doi.org/10.1039/c6cs00930a>.
- (132) Wu, X. X.; Fu, H. R.; Han, M. Le; Zhou, Z.; Ma, L. F. Tetraphenylethylene Immobilized Metal-Organic Frameworks: Highly Sensitive Fluorescent Sensor for the Detection of Cr<sup>2O7</sup><sup>2-</sup> and Nitroaromatic Explosives. *Cryst. Growth Des.* **2017**. <https://doi.org/10.1021/acs.cgd.7b01155>.
- (133) Guan, Q. L.; Han, C.; Bai, F. Y.; Liu, J.; Xing, Y. H.; Shi, Z.; Sun, L. X. Bismuth-MOF Based on Tetraphenylethylene Derivative as a Luminescent Sensor with Turn-off/on for Application of Fe<sup>3+</sup> Detection in Serum and Bioimaging, as Well as Emissive Spectra Analysis by TRES. *Sensors Actuators, B Chem.* **2020**, 325, 128767. <https://doi.org/10.1016/j.snb.2020.128767>.
- (134) Xia, Y. P.; Wang, C. X.; An, L. C.; Zhang, D. S.; Hu, T. L.; Xu, J.; Chang, Z.; Bu, X. H. Utilizing an Effective Framework to Dye Energy Transfer in a Carbazole-Based Metal-Organic Framework for High Performance White Light Emission Tuning. *Inorg. Chem. Front.* **2018**, 5 (11), 2868–2874. <https://doi.org/10.1039/c8qi00747k>.
- (135) Chen, Y.; Yu, B.; Cui, Y.; Xu, S.; Gong, J. Core-Shell Structured Cyclodextrin Metal-Organic Frameworks with Hierarchical Dye Encapsulation for Tunable Light Emission. *Chem. Mater.* **2019**, 31 (4), 1289–1295. <https://doi.org/10.1021/acs.chemmater.8b04126>.
- (136) Liu, X. Y.; Xing, K.; Li, Y.; Tsung, C. K.; Li, J. Three Models to Encapsulate Multicomponent Dyes into Nanocrystal Pores: A New Strategy for Generating High-Quality White Light. *J. Am. Chem. Soc.* **2019**, 141 (37), 14807–14813. <https://doi.org/10.1021/jacs.9b07236>.
- (137) Demel, J.; Kubát, P.; Millange, F.; Marrot, J.; Císařová, I.; Lang, K. Lanthanide-Porphyrin Hybrids: From Layered Structures to Metal-Organic Frameworks with Photophysical Properties. *Inorg. Chem.* **2013**. <https://doi.org/10.1021/ic400182u>.
- (138) Ding, Y.; Chen, Y. P.; Zhang, X.; Chen, L.; Dong, Z.; Jiang, H. L.; Xu, H.; Zhou, H. C. Controlled Intercalation and Chemical Exfoliation of Layered Metal-Organic Frameworks Using a Chemically Labile Intercalating Agent. *J. Am. Chem. Soc.* **2017**. <https://doi.org/10.1021/jacs.7b04829>.
- (139) Nie, X.; Wu, S.; Mensah, A.; Wang, Q.; Huang, F.; Wei, Q. FRET as a Novel Strategy to Enhance the Singlet Oxygen Generation of Porphyrinic MOF Decorated Self-Disinfecting

- Fabrics. *Chem. Eng. J.* **2020**. <https://doi.org/10.1016/j.cej.2020.125012>.
- (140) Meng, A. N.; Chaihu, L. X.; Chen, H. H.; Gu, Z. Y. Ultrahigh Adsorption and Singlet-Oxygen Mediated Degradation for Efficient Synergetic Removal of Bisphenol A by a Stable Zirconium-Porphyrin Metal-Organic Framework. *Sci. Rep.* **2017**. <https://doi.org/10.1038/s41598-017-06194-z>.
- (141) Zhou, W.; Begum, S.; Wang, Z.; Krolla, P.; Wagner, D.; Brä, S.; Wö, C.; Tsotsalas, M. High Antimicrobial Activity of Metal–Organic Framework-Templated Porphyrin Polymer Thin Films. **2017**. <https://doi.org/10.1021/acsami.7b14866>.
- (142) Buru, C. T.; Majewski, M. B.; Howarth, A. J.; Lavroff, R. H.; Kung, C. W.; Peters, A. W.; Goswami, S.; Farha, O. K. Improving the Efficiency of Mustard Gas Simulant Detoxification by Tuning the Singlet Oxygen Quantum Yield in Metal-Organic Frameworks and Their Corresponding Thin Films. *ACS Appl. Mater. Interfaces* **2018**. <https://doi.org/10.1021/acsami.8b05792>.
- (143) Zhang, R.; Liu, Y.; Wang, Z.; Wang, P.; Zheng, Z.; Qin, X.; Zhang, X.; Dai, Y.; Whangbo, M. H.; Huang, B. Selective Photocatalytic Conversion of Alcohol to Aldehydes by Singlet Oxygen over Bi-Based Metal-Organic Frameworks under UV–Vis Light Irradiation. *Appl. Catal. B Environ.* **2019**. <https://doi.org/10.1016/j.apcatb.2019.05.024>.
- (144) Gong, T.; Sui, Q.; Li, P.; Meng, X. F.; Zhou, L. J.; Chen, J.; Xu, J.; Wang, L.; Gao, E. Q. Versatile and Switchable Responsive Properties of a Lanthanide-Viologen Metal–Organic Framework. *Small* **2019**, *15* (5). <https://doi.org/10.1002/sml.201803468>.
- (145) Cadman, L. K.; Mahon, M. F.; Burrows, A. D. Inclusion of Viologen Cations Leads to Switchable Metal-Organic Frameworks. *Faraday Discuss.* **2020**. <https://doi.org/10.1039/c9fd00137a>.
- (146) Li, P.; Yin, X. M.; Gao, L. L.; Yang, S. L.; Sui, Q.; Gong, T.; Gao, E. Q. Modulating Excitation Energy of Luminescent Metal-Organic Frameworks for Detection of Cr(VI) in Water. *ACS Appl. Nano Mater.* **2019**. <https://doi.org/10.1021/acsanm.9b01088>.
- (147) Cui, S.; Zou, Y.; Yu, J.; Yin, Q.; Zhang, W.; Xing, L. A Novel Photochromic Metal Organic Framework Based on Viologen Exhibiting Benzene Detection and Photocontrolled Luminescence Properties in Solid State. *Inorg. Chem. Commun.* **2019**. <https://doi.org/10.1016/j.inoche.2019.107610>.
- (148) Dong, Z. P.; Zhang, L.; Liu, Z. L.; Wang, Y. Q. Two New Coordination Polymers Constructed

- by Two Viologen-Derived Ligands: Structure and Photochromism. *J. Mol. Struct.* **2020**, *1221*, 128782. <https://doi.org/10.1016/j.molstruc.2020.128782>.
- (149) Wan, F.; Qiu, L. X.; Zhou, L. L.; Sun, Y. Q.; You, Y. A Fluorescent, Photochromic and Thermochromic Trifunctional Material Based on a Layered Metal-Viologen Complex. *Dalt. Trans.* **2015**, *44* (42), 18320–18323. <https://doi.org/10.1039/c5dt03405a>.
- (150) Lv, X. Y.; Wang, M. S.; Yang, C.; Wang, G. E.; Wang, S. H.; Lin, R. G.; Guo, G. C. Photochromic Metal Complexes of N-Methyl-4,4'-Bipyridinium: Mechanism and Influence of Halogen Atoms. *Inorg. Chem.* **2012**, *51* (7), 4015–4019. <https://doi.org/10.1021/ic2020868>.
- (151) Gong, T.; Yang, X.; Fang, J. J.; Sui, Q.; Xi, F. G.; Gao, E. Q. Distinct Chromic and Magnetic Properties of Metal-Organic Frameworks with a Redox Ligand. *ACS Appl. Mater. Interfaces* **2017**, *9* (6), 5503–5512. <https://doi.org/10.1021/acsami.6b15540>.
- (152) Li, S. L.; Han, M.; Wu, B.; Wang, J.; Zhang, X. M. Photochromic Porous and Nonporous Viologen-Based Metal-Organic Frameworks for Visually Detecting Oxygen. *Cryst. Growth Des.* **2018**, *18* (7), 3883–3889. <https://doi.org/10.1021/acs.cgd.8b00189>.
- (153) Kan, W. Q.; Wen, S. Z.; He, Y. C.; Xu, C. Y. Viologen-Based Photochromic Coordination Polymers for Inkless and Erasable Prints. *Inorg. Chem.* **2017**, *56* (24), 14926–14935. <https://doi.org/10.1021/acs.inorgchem.7b02206>.
- (154) Li, Z.; Guo, J.; Xiang, F.; Lin, Q.; Ye, Y.; Zhang, J.; Chen, S.; Zhang, Z.; Xiang, S. Photochromic Naphthalene Diimide Cd-MOFs Based on Different Second Dicarboxylic Acid Ligands. *CrystEngComm* **2018**, *20* (46), 7567–7573. <https://doi.org/10.1039/c8ce01667d>.
- (155) AlKaabi, K.; Wade, C. R.; Dincă, M. Transparent-to-Dark Electrochromic Behavior in Naphthalene-Diimide-Based Mesoporous MOF-74 Analogs. *Chem* **2016**, *1* (2), 264–272. <https://doi.org/10.1016/j.chempr.2016.06.013>.
- (156) Fu, C.; Wang, H. Y.; Zhang, G. S.; Li, L.; Sun, Y. N.; Fu, J. W.; Zhang, H. The Influence of the Secondary Building Linker Geometry on the Photochromism of Naphthalenediimide-Based Metal-Organic Frameworks. *CrystEngComm* **2018**, *20* (33), 4849–4856. <https://doi.org/10.1039/c8ce00892b>.
- (157) Xu, H. L.; Zeng, X. S.; Li, J.; Xu, Y. C.; Qiu, H. J.; Xiao, D. R. The Impact of Metal Ions on Photoinduced Electron-Transfer Properties: Four Photochromic Metal-Organic Frameworks Based on a Naphthalenediimide Chromophore. *CrystEngComm* **2018**, *20* (17), 2430–2439. <https://doi.org/10.1039/c8ce00213d>.

- (158) Garai, B.; Mallick, A.; Banerjee, R. Photochromic Metal-Organic Frameworks for Inkless and Erasable Printing. *Chem. Sci.* **2016**, 7 (3), 2195–2200. <https://doi.org/10.1039/c5sc04450b>.
- (159) Liu, J. J.; Shan, Y. Bin; Fan, C. R.; Lin, M. J.; Huang, C. C.; Dai, W. X. Encapsulating Naphthalene in an Electron-Deficient MOF to Enhance Fluorescence for Organic Amines Sensing. *Inorg. Chem.* **2016**, 55 (7), 3680–3684. <https://doi.org/10.1021/acs.inorgchem.6b00252>.
- (160) Murugavel, K. Benzylic Viologen Dendrimers: A Review of Their Synthesis, Properties and Applications. *Polymer Chemistry*. 2014. <https://doi.org/10.1039/c4py00718b>.
- (161) Zhang, J.; Tian, H. The Endeavor of Diarylethenes: New Structures, High Performance, and Bright Future. *Advanced Optical Materials*. Wiley-VCH Verlag March 19, 2018, p 1701278. <https://doi.org/10.1002/adom.201701278>.
- (162) Schwartz, H. A.; Olthof, S.; Schaniel, D.; Meerholz, K.; Ruschewitz, U. Solution-Like Behavior of Photoswitchable Spiroyrans Embedded in Metal-Organic Frameworks. *Inorg. Chem.* **2017**, 56 (21), 13100–13110. <https://doi.org/10.1021/acs.inorgchem.7b01908>.
- (163) Bigdeli, F.; Lollar, C. T.; Morsali, A.; Zhou, H. C. Switching in Metal–Organic Frameworks. *Angewandte Chemie - International Edition*. 2020. <https://doi.org/10.1002/anie.201900666>.
- (164) Garg, S.; Schwartz, H.; Kozłowska, M.; Kanj, A. B.; Müller, K.; Wenzel, W.; Ruschewitz, U.; Heinke, L. Conductance Photoswitching of Metal–Organic Frameworks with Embedded Spiropyran. *Angew. Chemie Int. Ed.* **2019**, 58 (4), 1193–1197. <https://doi.org/10.1002/anie.201811458>.
- (165) Park, J.; Feng, D.; Yuan, S.; Zhou, H. C. Photochromic Metal-Organic Frameworks: Reversible Control of Singlet Oxygen Generation. *Angew. Chemie - Int. Ed.* **2015**, 54 (2), 430–435. <https://doi.org/10.1002/anie.201408862>.
- (166) Walton, I. M.; Cox, J. M.; Coppin, J. A.; Linderman, C. M.; Patel, D. G.; Benedict, J. B. Photo-Responsive MOFs: Light-Induced Switching of Porous Single Crystals Containing a Photochromic Diarylethene. *Chem. Commun.* **2013**. <https://doi.org/10.1039/c3cc44119a>.
- (167) Hermann, D.; Schwartz, H. A.; Werker, M.; Schaniel, D.; Ruschewitz, U. Metal-Organic Frameworks as Hosts for Fluorinated Azobenzenes: A Path towards Quantitative Photoswitching with Visible Light. *Chem. - A Eur. J.* **2019**, 25 (14), 3606–3616. <https://doi.org/10.1002/chem.201805391>.
- (168) He, J.; Aggarwal, K.; Katyal, N.; He, S.; Chiang, E.; Dunning, S. G.; Reynolds, J. E.; Steiner,

- A.; Henkelman, G.; Que, E. L.; Humphrey, S. M. Reversible Solid-State Isomerism of Azobenzene-Loaded Large-Pore Isoreticular Mg-CUK-1. *J. Am. Chem. Soc.* **2020**, *142* (14), 6467–6471. <https://doi.org/10.1021/jacs.9b13793>.
- (169) Hermann, D.; Schwartz, H. A.; Werker, M.; Schaniel, D.; Ruschewitz, U. Metal-Organic Frameworks as Hosts for Fluorinated Azobenzenes: A Path towards Quantitative Photoswitching with Visible Light. *Chem. - A Eur. J.* **2019**, *25* (14), 3606–3616. <https://doi.org/10.1002/chem.201805391>.
- (170) Müller, K.; Wadhwa, J.; Singh Malhi, J.; Schöttner, L.; Welle, A.; Schwartz, H.; Hermann, D.; Ruschewitz, U.; Heinke, L. Photoswitchable Nanoporous Films by Loading Azobenzene in Metal-Organic Frameworks of Type HKUST-1. *Chem. Commun.* **2017**, *53* (57), 8070–8073. <https://doi.org/10.1039/c7cc00961e>.
- (171) Hermann, D.; Emerich, H.; Lepski, R.; Schaniel, D.; Ruschewitz, U. Metal-Organic Frameworks as Hosts for Photochromic Guest Molecules. *Inorg. Chem.* **2013**, *52* (5), 2744–2749. <https://doi.org/10.1021/ic302856b>.
- (172) Yanai, N.; Uemura, T.; Inoue, M.; Matsuda, R.; Fukushima, T.; Tsujimoto, M.; Isoda, S.; Kitagawa, S. Guest-to-Host Transmission of Structural Changes for Stimuli-Responsive Adsorption Property. *J. Am. Chem. Soc.* **2012**, *134* (10), 4501–4504. <https://doi.org/10.1021/ja2115713>.
- (173) Zhang, Z.; Müller, K.; Heidrich, S.; Koenig, M.; Hashem, T.; Schlöder, T.; Bléger, D.; Wenzel, W.; Heinke, L. Light-Switchable One-Dimensional Photonic Crystals Based on MOFs with Photomodulatable Refractive Index. *J. Phys. Chem. Lett.* **2019**, *10* (21), 6626–6633. <https://doi.org/10.1021/acs.jpcclett.9b02614>.
- (174) Prasetya, N.; Ladewig, B. P. An Insight into the Effect of Azobenzene Functionalities Studied in UiO-66 Frameworks for Low Energy CO<sub>2</sub> Capture and CO<sub>2</sub>/N<sub>2</sub> Membrane Separation. *J. Mater. Chem. A* **2019**, *7* (25), 15164–15172. <https://doi.org/10.1039/c9ta02096a>.
- (175) Brown, J. W.; Henderson, B. L.; Kiesz, M. D.; Whalley, A. C.; Morris, W.; Grunder, S.; Deng, H.; Furukawa, H.; Zink, J. I.; Stoddart, J. F.; Yaghi, O. M. Photophysical Pore Control in an Azobenzene-Containing Metal-Organic Framework. *Chem. Sci.* **2013**, *4* (7), 2858–2864. <https://doi.org/10.1039/c3sc21659d>.
- (176) Wang, Z.; Müller, K.; Valášek, M.; Grosjean, S.; Bräse, S.; Wöll, C.; Mayor, M.; Heinke, L. Series of Photoswitchable Azobenzene-Containing Metal-Organic Frameworks with Variable

- Adsorption Switching Effect. *J. Phys. Chem. C* **2018**, *122* (33), 19044–19050. <https://doi.org/10.1021/acs.jpcc.8b05843>.
- (177) Wang, Z.; Heinke, L.; Jelic, J.; Cakici, M.; Dommaschk, M.; Maurer, R. J.; Oberhofer, H.; Grosjean, S.; Herges, R.; Bräse, S.; Reuter, K.; Wöll, C. Photoswitching in Nanoporous, Crystalline Solids: An Experimental and Theoretical Study for Azobenzene Linkers Incorporated in MOFs. *Phys. Chem. Chem. Phys.* **2015**, *17* (22), 14582–14587. <https://doi.org/10.1039/c5cp01372k>.
- (178) Meng, X.; Gui, B.; Yuan, D.; Zeller, M.; Wang, C. Mechanized Azobenzene-Functionalized Zirconium Metal-Organic Framework for on-Command Cargo Release. *Sci. Adv.* **2016**, *2* (8), e1600480. <https://doi.org/10.1126/sciadv.1600480>.
- (179) Modrow, A.; Zargarani, D.; Herges, R.; Stock, N. Introducing a Photo-Switchable Azo-Functionality inside Cr-MIL-101-NH 2 by Covalent Post-Synthetic Modification. *Dalton Transactions*. 2012. <https://doi.org/10.1039/c2dt30672g>.
- (180) Heinke, L.; Cakici, M.; Dommaschk, M.; Grosjean, S.; Herges, R.; Bräse, S.; Wöll, C. Photoswitching in Two-Component Surface-Mounted Metal-Organic Frameworks: Optically Triggered Release from a Molecular Container. *ACS Nano* **2014**, *8* (2), 1463–1467. <https://doi.org/10.1021/nn405469g>.
- (181) Saura-Sanmartin, A.; Martinez-Cuevza, A.; Bautista, D.; Marzari, M. R. B.; Martins, M. A. P.; Alajarin, M.; Berna, J. Copper-Linked Rotaxanes for the Building of Photoresponsive Metal Organic Frameworks with Controlled Cargo Delivery. *J. Am. Chem. Soc.* **2020**, *142* (31), 13442–13449. <https://doi.org/10.1021/jacs.0c04477>.
- (182) Müller, K.; Helfferich, J.; Zhao, F.; Verma, R.; Kanj, A. B.; Meded, V.; Bléger, D.; Wenzel, W.; Heinke, L. Switching the Proton Conduction in Nanoporous, Crystalline Materials by Light. *Adv. Mater.* **2018**, *30* (8), 1706551. <https://doi.org/10.1002/adma.201706551>.
- (183) Meng, H.; Zhao, C.; Nie, M.; Wang, C.; Wang, T. Optically Controlled Molecular Metallofullerene Magnetism via an Azobenzene-Functionalized Metal-Organic Framework. *ACS Appl. Mater. Interfaces* **2018**, *10* (38), 32607–32612. <https://doi.org/10.1021/acsami.8b11098>.
- (184) Lin, P. C.; Lin, S.; Wang, P. C.; Sridhar, R. Techniques for Physicochemical Characterization of Nanomaterials. *Biotechnology Advances*. Elsevier Inc. 2014, pp 711–726. <https://doi.org/10.1016/j.biotechadv.2013.11.006>.

- (185) Brown, P. D. Structural Characterization. In *Springer Handbooks*; Springer, 2017; p 1. [https://doi.org/10.1007/978-3-319-48933-9\\_17](https://doi.org/10.1007/978-3-319-48933-9_17).
- (186) Klute, A.; Whittig, L. D.; Allardice, W. R. X-Ray Diffraction Techniques; John Wiley & Sons, Ltd, 1986; pp 331–362. <https://doi.org/10.2136/sssabookser5.1.2ed.c12>.
- (187) Inaba, K.; Kobayashi, S.; Uehara, K.; Okada, A.; Reddy, S. L.; Endo, T. High Resolution X-Ray Diffraction Analyses of (La,Sr)MnO<sub>3</sub>/ZnO/Sapphire(0001) Double Heteroepitaxial Films. *Adv. Mater. Phys. Chem.* **2013**, *03* (01), 72–89. <https://doi.org/10.4236/ampc.2013.31a010>.
- (188) Mitsunaga, T. X-Ray Thin-Film Measurement Techniques II. *Rigaku J.* **2009**, *25*, 1.
- (189) K Inaba. X-Ray Thin-Film Measurement Techniques. *The Rigaku Journal*, **2008**, *1* (24).
- (190) Theophanides, T. Introduction to Infrared Spectroscopy. *Infrared Spectrosc. - Mater. Sci. Eng. Technol.* **2012**. <https://doi.org/10.5772/49106>.
- (191) Nielsen, H. H. Infrared Spectroscopy. *Science*. Macmillan Education UK: London 1951, p 3. <https://doi.org/10.1126/science.113.2940.3>.
- (192) El-Azazy, M. Introductory Chapter: Infrared Spectroscopy - A Synopsis of the Fundamentals and Applications. In *Infrared Spectroscopy - Principles, Advances, and Applications*; IntechOpen, 2019. <https://doi.org/10.5772/intechopen.82210>.
- (193) David L Andrews. *Molecular Photophysics and Spectroscopy*; Morgan & Claypool Publishers, 2014.
- (194) Berthomieu, C.; Hienerwadel, R. Fourier Transform Infrared (FTIR) Spectroscopy. *Photosynthesis Research*. Springer September 10, 2009, pp 157–170. <https://doi.org/10.1007/s11120-009-9439-x>.
- (195) Aroui, H.; Orphal, J.; Kwabia, F. Fourier Transform Infrared Spectroscopy for the Measurement of Spectral Line Profiles. *Fourier Transform - Mater. Anal.* **2012**. <https://doi.org/10.5772/36120>.
- (196) Peak, D. Fourier Transform Infrared Spectroscopy. In *Encyclopedia of Soils in the Environment*; 2004; Vol. 4, pp 80–85. <https://doi.org/10.1016/B0-12-348530-4/00174-0>.
- (197) Perkins, W. D. Fourier Transform Infrared Spectroscopy. Part III. Applications. *J. Chem. Educ.* **1987**, *64* (12), A296. <https://doi.org/10.1021/ed064pa296>.
- (198) Wang, H.; Wang, Y.; Chen, D.; Chen, W.; Oriana, A.; Manzoni, C.; Hauri, C. P.; Helbing, J.; Cerullo, G. Introductory Fourier Transform Spectroscopy (Academic, 1972). 3. V. Saptari, Fourier-Transform Spectroscopy. **1970**, 3–17. <https://doi.org/10.6084/m9.figshare.5235841>.

- (199) Hollins, P. Reflection – Absorption Spectroscopy 1 INTRODUCTION AND HISTORICAL. **2006**, 1–17. <https://doi.org/10.1002/9780470027318.a5605>.
- (200) Buffeteau, T.; Desbat, B.; Turlet, J. M. Polarization Modulation FT-IR Spectroscopy of Surfaces and Ultra-Thin Films: Experimental Procedure and Quantitative Analysis. *Appl. Spectrosc.* **1991**, *45* (3), 380–389. <https://doi.org/10.1366/0003702914337308>.
- (201) Ausili, A.; Sánchez, M.; Gómez-Fernández, J. C. Attenuated Total Reflectance Infrared Spectroscopy: A Powerful Method for the Simultaneous Study of Structure and Spatial Orientation of Lipids and Membrane Proteins. *Biomed. Spectrosc. Imaging* **2015**, *4* (2), 159–170. <https://doi.org/10.3233/bsi-150104>.
- (202) Shai, Y. ATR-FTIR Studies in Pore Forming and Membrane Induced Fusion Peptides. *Biochimica et Biophysica Acta - Biomembranes*. Elsevier 2013, pp 2306–2313. <https://doi.org/10.1016/j.bbamem.2012.11.027>.
- (203) Akash, M. S. H.; Rehman, K.; Akash, M. S. H.; Rehman, K. Ultraviolet-Visible (UV-VIS) Spectroscopy. In *Essentials of Pharmaceutical Analysis*; Springer Singapore, 2020; pp 29–56. [https://doi.org/10.1007/978-981-15-1547-7\\_3](https://doi.org/10.1007/978-981-15-1547-7_3).
- (204) Braeuer, A. Interaction of Matter and Electromagnetic Radiation. In *Supercritical Fluid Science and Technology*; Elsevier, 2015; Vol. 7, pp 41–192. <https://doi.org/10.1016/B978-0-444-63422-1.00002-X>.
- (205) Salman Ali, A. Application of Nanomaterials in Environmental Improvement. In *Nanotechnology and the Environment*; IntechOpen, 2020. <https://doi.org/10.5772/intechopen.91438>.
- (206) Zhou, W.; Wang, Z. L. *Scanning Microscopy for Nanotechnology: Techniques and Applications*; 2007. <https://doi.org/10.1007/978-0-387-39620-0>.
- (207) Henini, M. Scanning Electron Microscopy: An Introduction. *III-Vs Rev.* **2000**, *13* (4), 40–44. [https://doi.org/10.1016/S0961-1290\(00\)80006-X](https://doi.org/10.1016/S0961-1290(00)80006-X).
- (208) Rades, S.; Hodoroaba, V. D.; Salge, T.; Wirth, T.; Lobera, M. P.; Labrador, R. H.; Natte, K.; Behnke, T.; Gross, T.; Unger, W. E. S. High-Resolution Imaging with SEM/T-SEM, EDX and SAM as a Combined Methodical Approach for Morphological and Elemental Analyses of Single Engineered Nanoparticles. *RSC Adv.* **2014**, *4* (91), 49577–49587. <https://doi.org/10.1039/c4ra05092d>.
- (209) Norman, D. *X-Ray Absorption Spectroscopy (EXAFS and XANES) at Surfaces Related Content*

*X-Ray Absorption Spectroscopy (EXAFS and XANES) at Surfaces*; 1986; Vol. 19.

- (210) Alp, E. E.; Mini, S. M.; Ramanathan, M. X-Ray Absorption Spectroscopy: EXAFS and XANES-A Versatile Tool to Study the Atomic and Electronic Structure of Materials. *Synchrotron x-ray sources new Oppor. soil Environ. Sci.* **1990**, 25–36.
- (211) Solomon, D.; Lehmann, J.; Kinyangi, J.; Liang, B.; Schäfer, T. Carbon K-Edge NEXAFS and FTIR-ATR Spectroscopic Investigation of Organic Carbon Speciation in Soils. *Soil Sci. Soc. Am. J.* **2005**, 69 (1), 107. <https://doi.org/10.2136/sssaj2005.0107dup>.
- (212) Park, T. J.; Sambasivan, S.; Fischer, D. A.; Yoon, W. S.; Misewich, J. A.; Wong, S. S. Electronic Structure and Chemistry of Iron-Based Metal Oxide Nanostructured Materials: A NEXAFS Investigation of BiFeO<sub>3</sub>, Bi<sub>2</sub>Fe<sub>4</sub>O<sub>9</sub>,  $\alpha$ -Fe<sub>2</sub>O<sub>3</sub>,  $\gamma$ -Fe<sub>2</sub>O<sub>3</sub>, and Fe/Fe<sub>3</sub>O<sub>4</sub>. *J. Phys. Chem. C* **2008**, 112 (28), 10359–10369. <https://doi.org/10.1021/jp801449p>.
- (213) Liu, J.; Schüpbach, B.; Bashir, A.; Shekhah, O.; Nefedov, A.; Kind, M.; Terfort, A.; Wöll, C. Structural Characterization of Self-Assembled Monolayers of Pyridine-Terminated Thiolates on Gold. *Phys. Chem. Chem. Phys.* **2010**, 12 (17), 4459–4472. <https://doi.org/10.1039/b92424246p>.
- (214) Zhang, W.; Nefedov, A.; Naboka, M.; Cao, L.; Wöll, C. Molecular Orientation of Terephthalic Acid Assembly on Epitaxial Graphene: NEXAFS and XPS Study. *Phys. Chem. Chem. Phys.* **2012**, 14 (29), 10125–10131. <https://doi.org/10.1039/c2cp23748b>.
- (215) Nefedov, A.; Wöll, C. Advanced Applications of NEXAFS Spectroscopy for Functionalized Surfaces. *Springer Ser. Surf. Sci.* **2013**, 51 (1), 277–303. [https://doi.org/10.1007/978-3-642-34243-1\\_10](https://doi.org/10.1007/978-3-642-34243-1_10).
- (216) Schöll, A.; Zou, Y.; Schmidt, T.; Fink, R.; Umbach, E. Energy Calibration and Intensity Normalization in High-Resolution NEXAFS Spectroscopy. *J. Electron Spectros. Relat. Phenomena* **2003**, 129 (1), 1–8. [https://doi.org/10.1016/S0368-2048\(03\)00016-1](https://doi.org/10.1016/S0368-2048(03)00016-1).
- (217) Arnold, R.; Azzam, W.; Terfort, A.; Wöll, C. Preparation, Modification, and Crystallinity of Aliphatic and Aromatic Carboxylic Acid Terminated Self-Assembled Monolayers. **2002**. <https://doi.org/10.1021/la0117000>.
- (218) Boca, S.; Leordean, C.; Astilean, S.; Farcau, C. Chemiresistive/SERS Dual Sensor Based on Densely Packed Gold Nanoparticles. *Beilstein J. Nanotechnol.* **2015**, 6 (1), 2498–2503. <https://doi.org/10.3762/bjnano.6.259>.
- (219) Shi, D.; Ren, Y.; Jiang, H.; Lu, J.; Cheng, X. A New Three-Dimensional Metal-Organic

Framework Constructed from 9,10-Anthracene Dibenzoate and Cd(II) as a Highly Active Heterogeneous Catalyst for Oxidation of Alkylbenzenes. *Dalt. Trans.* **2013**, *42* (2), 484–491. <https://doi.org/10.1039/c2dt31844j>.

- (220) Seth, S.; Savitha, G.; Jhulki, S.; Moorthy, J. N. Diverse Metal-Organic Materials (MOMs) Based on 9,9'-Bianthryl-Dicarboxylic Acid Linker: Luminescence Properties and CO<sub>2</sub> Capture. *Cryst. Growth Des.* **2016**, *16* (4), 2024–2032. <https://doi.org/10.1021/acs.cgd.5b01617>.
- (221) Yu, F.; Zhang, Y. M.; Guo, Y. H.; Li, A. H.; Yu, G. X.; Li, B. Various Crystal Structures Based on 4,4'-(Diethynylantracene-9,10- Diyl) Dibenzoic Acid: From 0D Dimer to 3D Net Framework. *CrystEngComm* **2013**, *15* (41), 8273–8279. <https://doi.org/10.1039/c3ce41000e>.
- (222) Liu, J.; Lukose, B.; Shekhah, O.; Arslan, H. K.; Weidler, P.; Gliemann, H.; Bräse, S.; Grosjean, S.; Godt, A.; Feng, X.; Müllen, K.; Magdau, I. B.; Heine, T.; Wöll, C. A Novel Series of Isorecticular Metal Organic Frameworks: Realizing Metastable Structures by Liquid Phase Epitaxy. *Sci. Rep.* **2012**, *2* (1), 1–5. <https://doi.org/10.1038/srep00921>.
- (223) Costas, M.; Cady, C. W.; Kryatov, S. V.; Ray, M.; Ryan, M. J.; Rybak-Akimova, E. V.; Que, L. Role of Carboxylate Bridges in Modulating Nonheme Diiron(II)/O<sub>2</sub> Reactivity. **2003**. <https://doi.org/10.1021/ic034359a>.
- (224) Arabei, S. M.; Pavich, T. a. Photoinduced Oxidation of Diphenylbisanthene and Its Spectral Manifestations. **2004**, *71* (2), 173–178.
- (225) Halder, R.; Jakoby, M.; Mazel, A.; Zhang, Q.; Welle, A.; Mohamed, T.; Krolla, P.; Wenzel, W.; Diring, S.; Odobel, F.; Richards, B. S.; Howard, I. A.; Wöll, C. Anisotropic Energy Transfer in Crystalline Chromophore Assemblies. *Nat. Commun.* **2018**, *9* (1), 1–8. <https://doi.org/10.1038/s41467-018-06829-3>.
- (226) Liang, X.; Guo, Z.; Wei, H.; Liu, X.; Lv, H.; Xing, H. Selective Photooxidation of Sulfides Mediated by Singlet Oxygen Using Visible-Light-Responsive Coordination Polymers. *Chem. Commun.* **2018**, *54* (92), 13002–13005. <https://doi.org/10.1039/C8CC07585A>.
- (227) Fudickar, W.; Linker, T. Reversible Photooxygenation of Alkynylantracenes: Chemical Generation of Singlet Oxygen under Very Mild Conditions. *Chem. - A Eur. J.* **2011**, *17* (49), 13661–13664. <https://doi.org/10.1002/chem.201102230>.
- (228) Scheffer, J. R.; Amer, J.; Moureu, ; C; Dufraisse, C.; Dean ; Gollnick, P. M.; Schenck, G. O.; Bergmann, ; W; Mclean, M. J.; Dufraisse, ; C; Enderlin ; C. Dufraisse, L.; Lebras, J. ) (A)

*National Institutes of Health Postdoctoral Fellow, 1966-1967. (b) National Institutes of Health Predoctoral Fellow; Academic Press, 1967; Vol. 89.*

- (229) Aubry, J. M.; Pierlot, C.; Rigaudy, J.; Schmidt, R. Reversible Binding of Oxygen to Aromatic Compounds. *Acc. Chem. Res.* **2003**, *36* (9), 668–675. <https://doi.org/10.1021/ar010086g>.
- (230) Reddy, A. R.; Bendikov, M. Diels-Alder Reaction of Acenes with Singlet and Triplet Oxygen - Theoretical Study of Two-State Reactivity. *Chem. Commun.* **2006**, No. 11, 1179–1181. <https://doi.org/10.1039/b513597d>.
- (231) Bauch, M.; Klaper, M.; Linker, T.; Fudickar, W.; Linker, T. Reversible Photooxygenation of Alkynylanthracenes: Chemical Generation of Singlet Oxygen under Very Mild Conditions. *Chem. - A Eur. J.* **2011**, *30* (4), 13661–13664. <https://doi.org/10.1002/poc.3607>.
- (232) Aubry, J. M.; Pierlot, C.; Rigaudy, J.; Schmidt, R. Reversible Binding of Oxygen to Aromatic Compounds. *Acc. Chem. Res.* **2003**, *36* (9), 668–675. <https://doi.org/10.1021/ar010086g>.
- (233) Kwak, W. J.; Kim, H.; Petit, Y. K.; Leypold, C.; Nguyen, T. T.; Mahne, N.; Redfern, P.; Curtiss, L. A.; Jung, H. G.; Borisov, S. M.; Freunberger, S. A.; Sun, Y. K. Deactivation of Redox Mediators in Lithium-Oxygen Batteries by Singlet Oxygen. *Nat. Commun.* **2019**. <https://doi.org/10.1038/s41467-019-09399-0>.
- (234) Villamena, F. A.; Merle, J. K.; Hadad, C. M.; Zweier, J. L. Superoxide Radical Anion Adduct of 5,5-Dimethyl-1-Pyrroline W-Oxide (DMPO). 1. the Thermodynamics of Formation and Its Acidity. *J. Phys. Chem. A* **2005**. <https://doi.org/10.1021/jp052431f>.
- (235) Zhang, X. F.; Li, X. The Photostability and Fluorescence Properties of Diphenylisobenzofuran. *J. Lumin.* **2011**, *131* (11), 2263–2266. <https://doi.org/10.1016/j.jlumin.2011.05.048>.
- (236) Entradas, T.; Waldron, S.; Volk, M. The Detection Sensitivity of Commonly Used Singlet Oxygen Probes in Aqueous Environments. *J. Photochem. Photobiol. B Biol.* **2020**. <https://doi.org/10.1016/j.jphotobiol.2020.111787>.
- (237) Salokhiddinov, K. I.; Byteva, I. M.; Gurinovich, G. P. Lifetime of Singlet Oxygen in Various Solvents. *J. Appl. Spectrosc.* **1981**. <https://doi.org/10.1007/BF00613067>.
- (238) Jensen, R. L.; Arnbjerg, J.; Ogilby, P. R. Temperature Effects on the Solvent-Dependent Deactivation of Singlet Oxygen. *J. Am. Chem. Soc.* **2010**. <https://doi.org/10.1021/ja101753n>.
- (239) Park, J.; Jiang, Q.; Feng, D.; Zhou, H. C. Controlled Generation of Singlet Oxygen in Living Cells with Tunable Ratios of the Photochromic Switch in Metal–Organic Frameworks. *Angew. Chemie - Int. Ed.* **2016**, *55* (25), 7188–7193. <https://doi.org/10.1002/anie.201602417>.

- (240) Vacque, V.; Sombret, B.; Huvenne, J. P.; Legrand, P.; Suc, S. Characterisation of the O-O Peroxide Bond by Vibrational Spectroscopy. *Spectrochim. Acta - Part A Mol. Spectrosc.* **1997**, *53* (1), 55–66. [https://doi.org/10.1016/s1386-1425\(97\)83009-0](https://doi.org/10.1016/s1386-1425(97)83009-0).
- (241) Scholes, G. D.; Fournier, T.; Phillips, D.; Parker, A. W. *Solvent-Dependent Resonance Raman Excitation Profiles of 9,9'-Bianthryl*; 1999; Vol. 19.
- (242) Ferrari, A. C.; Robertson, J. Raman Spectroscopy of Amorphous, Nanostructured, Diamond-like Carbon, and Nanodiamond. *Philosophical Transactions of the Royal Society A: Mathematical, Physical and Engineering Sciences*. Royal Society 2004, pp 2477–2512. <https://doi.org/10.1098/rsta.2004.1452>.
- (243) McGarvey, D. J.; Szekeres, P. G.; Wilkinson, F. The Efficiency of Singlet Oxygen Generation by Substituted Naphthalenes in Benzene. Evidence for the Participation of Charge-Transfer Interactions. *Chem. Phys. Lett.* **1992**, *199* (3–4), 314–319. [https://doi.org/10.1016/0009-2614\(92\)80124-T](https://doi.org/10.1016/0009-2614(92)80124-T).
- (244) Wilkinson, F.; Abdel-Shafi, A. A. Mechanism of Quenching of Triplet States by Molecular Oxygen: Biphenyl Derivatives in Different Solvents. *J. Phys. Chem. A* **1999**, *103* (28), 5425–5435. <https://doi.org/10.1021/jp9907995>.
- (245) Grewer, C.; Brauer, H. D. Mechanism of the Triplet-State Quenching by Molecular Oxygen in Solution. *J. Phys. Chem.* **1994**, *98* (16), 4230–4235. <https://doi.org/10.1021/j100067a006>.
- (246) Salokhiddinov, K. I.; Byteva, I. M.; Gurinovich, G. P. Lifetime of Singlet Oxygen in Various Solvents. *J. Appl. Spectrosc.* **1981**, *34* (5), 561–564. <https://doi.org/10.1007/BF00613067>.
- (247) Sagadevan, A.; Hwang, K. C.; Su, M. Der. Singlet Oxygen-Mediated Selective C-H Bond Hydroperoxidation of Ethereal Hydrocarbons. *Nat. Commun.* **2017**. <https://doi.org/10.1038/s41467017-01906-5>.
- (248) Castro-Olivares, R.; Günther, G.; Zanocco, A. L.; Lemp, E. Linear Free Energy Relationship Analysis of Solvent Effect on Singlet Oxygen Reactions with Mono and Disubstituted Anthracene Derivatives. *J. Photochem. Photobiol. A Chem.* **2009**, *207* (2–3), 160–166. <https://doi.org/10.1016/j.jphotochem.2009.05.012>.
- (249) Olea, A. F.; Wilkinson, F. Singlet Oxygen Production from Excited Singlet and Triplet States of Anthracene Derivatives in Acetonitrile. *J. Phys. Chem.* **1995**, *99* (13), 4518–4524. <https://doi.org/10.1021/j100013a022>.
- (250) Bauch, M.; Klaper, M.; Linker, T. Intermediates in the Cleavage of Endoperoxides. *J. Phys.*

- Org. Chem.* **2017**, *30* (4), 2–7. <https://doi.org/10.1002/poc.3607>.
- (251) Liu, J. J.; Guan, Y. F.; Lin, M. J.; Huang, C. C.; Dai, W. X. Anion-Mediated Architecture and Photochromism of Rigid Bipyridinium-Based Coordination Polymers. *Cryst. Growth Des.* **2016**, *16* (5), 2826–2842. <https://doi.org/10.1021/acs.cgd.6b00163>.
- (252) Li, P.; Guo, M. Y.; Yin, X. M.; Gao, L. L.; Yang, S. L.; Bu, R.; Gong, T.; Gao, E. Q. Interpenetration-Enabled Photochromism and Fluorescence Photomodulation in a Metal-Organic Framework with the Thiazolothiazole Extended Viologen Fluorophore. *Inorg. Chem.* **2019**, *58* (20), 14167–14174. <https://doi.org/10.1021/acs.inorgchem.9b02220>.
- (253) Fu, T.; Wei, Y. L.; Zhang, C.; Li, L. K.; Liu, X. F.; Li, H. Y.; Zang, S. Q. A Viologen-Based Multifunctional Eu-MOF: Photo/Electro-Modulated Chromism and Luminescence. *Chem. Commun.* **2020**, *56* (86), 13093–13096. <https://doi.org/10.1039/d0cc06096h>.
- (254) Li, P.; Zhou, L. J.; Yang, N. N.; Sui, Q.; Gong, T.; Gao, E. Q. Metal-Organic Frameworks with Extended Viologen Units: Metal-Dependent Photochromism, Photomodulable Fluorescence, and Sensing Properties. *Cryst. Growth Des.* **2018**, *18* (11), 7191–7198. <https://doi.org/10.1021/acs.cgd.8b01383>.
- (255) Lv, X. Y.; Wang, M. S.; Yang, C.; Wang, G. E.; Wang, S. H.; Lin, R. G.; Guo, G. C. Photochromic Metal Complexes of N-Methyl-4,4'-Bipyridinium: Mechanism and Influence of Halogen Atoms. *Inorg. Chem.* **2012**, *51* (7), 4015–4019. <https://doi.org/10.1021/ic2020868>.
- (256) Sun, J. K.; Wang, P.; Chen, C.; Zhou, X. J.; Wu, L. M.; Zhang, Y. F.; Zhang, J. Charge-Distribution-Related Regioisomerism of Photoresponsive Metal-Organic Polymeric Chains. *Dalt. Trans.* **2012**, *41* (43), 13441–13446. <https://doi.org/10.1039/c2dt31552a>.
- (257) Sun, J. K.; Wang, P.; Yao, Q. X.; Chen, Y. J.; Li, Z. H.; Zhang, Y. F.; Wu, L. M.; Zhang, J. Solvent- and Anion-Controlled Photochromism of Viologen-Based Metal-Organic Hybrid Materials. *J. Mater. Chem.* **2012**, *22* (24), 12212–12219. <https://doi.org/10.1039/c2jm30558e>.
- (258) Bala, T.; Prasad, B. L. V.; Sastry, M.; Kahaly, M. U.; Waghmare, U. V. Interaction of Different Metal Ions with Carboxylic Acid Group: A Quantitative Study. *J. Phys. Chem. A* **2007**. <https://doi.org/10.1021/jp067906x>.
- (259) Shi, Q.; Wu, S. Y.; Qiu, X. T.; Sun, Y. Q.; Zheng, S. T. Three Viologen-Derived Zn-Organic Materials: Photochromism, Photomodulated Fluorescence, and Inkless and Erasable Prints. *Dalt. Trans.* **2019**. <https://doi.org/10.1039/C8DT04393K>.
- (260) Heinke, L.; Gu, Z.; Wöll, C. The Surface Barrier Phenomenon at the Loading of Metal-Organic

- Frameworks. *Nat. Commun.* **2014**. <https://doi.org/10.1038/ncomms5562>.
- (261) Mortimer, R. J.; Dyer, A. L.; Reynolds, J. R. Electrochromic Organic and Polymeric Materials for Display Applications. *Displays*. Elsevier 2006, pp 2–18. <https://doi.org/10.1016/j.displa.2005.03.003>.
- (262) Tan, Y.; Chen, H.; Zhang, J.; Liao, S.; Dai, J.; Fu, Z. Synthesis of a 3D Photochromic Coordination Polymer with an Interpenetrating Arrangement: Crystal Engineering for Electron Transfer between Donor and Acceptor Units. *CrystEngComm* **2012**, *14* (16), 5137–5139. <https://doi.org/10.1039/c2ce25618e>.
- (263) Zhang, Z. J.; Xiang, S. C.; Guo, G. C.; Xu, G.; Wang, M. S.; Zou, J. P.; Guo, S. P.; Huang, J. S. Wavelength-Dependent Photochromic Inorganic-Organic Hybrid Based on a 3D Iodoplumbate Open-Framework Material. *Angew. Chemie - Int. Ed.* **2008**, *47* (22), 4149–4152. <https://doi.org/10.1002/anie.200800603>.
- (264) Tan, Y.; Fu, Z.; Zeng, Y.; Chen, H.; Liao, S.; Zhang, J.; Dai, J. Highly Stable Photochromic Crystalline Material Based on a Close-Packed Layered Metal-Viologen Coordination Polymer. *J. Mater. Chem.* **2012**, *22* (34), 17452–17455. <https://doi.org/10.1039/c2jm34341j>.
- (265) Kan, W. Q.; He, Y. C.; Wen, S. Z.; Zhao, P. S. A Series of Host-Guest Coordination Polymers Containing Viologens: Syntheses, Crystal Structures, Thermo/Photochromism and Factors Influencing Their Thermo/Photochromic Behaviors. *Dalt. Trans.* **2019**. <https://doi.org/10.1039/c9dt03929e>.
- (266) Gong, T.; Yang, X.; Sui, Q.; Qi, Y.; Xi, F. G.; Gao, E. Q. Magnetic and Photochromic Properties of a Manganese(II) Metal-Zwitterionic Coordination Polymer. *Inorg. Chem.* **2016**, *55* (1), 96–103. <https://doi.org/10.1021/acs.inorgchem.5b01888>.
- (267) Yu, X. Q.; Sun, C.; Liu, B. W.; Wang, M. S.; Guo, G. C. Directed Self-Assembly of Viologen-Based 2D Semiconductors with Intrinsic UV–SWIR Photoresponse after Photo/Thermo Activation. *Nat. Commun.* **2020**, *11* (1), 1–7. <https://doi.org/10.1038/s41467-020-14986-7>.
- (268) He, Y.; Huang, Y. R.; Li, Y. L.; Li, H. H.; Chen, Z. R.; Jiang, R. Encapsulating Halometallates into 3-D Lanthanide-Viologen Frameworks: Controllable Emissions, Reversible Thermochromism, Photocurrent Responses, and Electrical Bistability Behaviors. *Inorg. Chem.* **2019**. <https://doi.org/10.1021/acs.inorgchem.9b01740>.

## 8 Publication

- 1- H. Babaei, M.E. DeCoster, M. Jeong, **Z.M. Hassan**, T. Islamoglu, H. Baumgart, A.J.H. McGaughey, E. Redel, O.K. Farha, P.E. Hopkins, J.A. Malen, C.E. Wilmer, Observation of reduced thermal conductivity in a metal-organic framework due to the presence of adsorbates, *Nat. Commun.* (2020).
- 2- V. Linseis, **Z.M. Hassan**, H. Reith, J. Garcia, K. Nielsch, H. Baumgart, E. Redel, P. Woias, Complete Thermoelectric Characterization of PEDOT:PSS Thin Films with a Novel ZT Test Chip Platform, *Phys. Status Solidi Appl. Mater. Sci.* 215 (2018).
- 3- X. Chen, Z. Wang, **Z.M. Hassan**, P. Lin, K. Zhang, H. Baumgart, E. Redel, Seebeck Coefficient Measurements of Polycrystalline and Highly Ordered Metal-Organic Framework Thin Films, *ECS J. Solid State Sci. Technol.* 6 (2017).
- 4- W. Guo, **Z.M. Hassan**, C. Kübel, R. Haldar, P.G. Weidler, S. Heissler, K. Peikert, M. Fröba, E. Redel, C. Wöll, MOF-Templated Synthesis of 3D Bi<sub>2</sub>O<sub>3</sub> Supracrystals with Bcc Packing, *Nanoscale* 10 (2018) 17099–17104.
- 5- Xin Chen, Kai Zhang, **Zeinab Mohamed Hassan**, Engelbert Redel and Helmut Baumgart, Charge Transport, Conductivity and Seebeck Coefficient in Pristine and TCNQ Loaded Preferentially Grown Metal-Organic Framework Films, *Journal of Physics: Condensed Matter*, 2021, **accepted**.
- 6- **Zeinab Hasan**, Alexei Nefedov, Peter Weidler, Stefan Heissler, Ritesh Haldar, Christof Wöll, Self-photosensitized oxidation of a Bianthryl-based metal-organic framework thin film, **under publication**
- 7- Mallory E. DeCoster, Hasan Babaei, Sangeun S. Jung, **Zeinab Hassan**, Yousuf Mohammed, Abdelmageed Elmustafa, Helmut Baumgart, John T. Gaskins, Ashutosh Giri, Emma Tiernan, John A. Tomko, Pamela M. Norris, Alan J. McGaughey, Chris Wilmer, Engelbert Redel, Gaurav Giri, and Patrick E. Hopkins, Resonant Vibrational Modes from Guest-Host Interactions Reduce the Thermal Conductivity of Metal Organic Frameworks (MOFs), **under publication**
- 8- **Zeinab Hassan**, Benedikt Sapotta, Ritesh halder , Frank Biedermann , Alexei Nefedov, Raheleh Azmi ,Manuel Tsotsalas, Salma Begum, Christof Wöll, Viologen-based Photochromic Metal-Organic Framework Thin Films: Low-Temperature Layer-by-Layer Synthesis Yield Highly High Porosity, **under publication**.

- 9- Wei Guo, **Zeinab Mohammed Hassan**, Kai Müller, Tim Seifert, Alexander Welle, Stefan Heissler, Xiaojuan Yu, Ritesh Haldar, Peter G. Weidler, Lars Heinke, Yuemin Wang, W. Klopper, P. W. Roesky, Christof Wöll, Engelbert Redel, Loading and formation of an unusual supramolecular HKUST-1@Au complex, **under publication**.
- 10- Papa K. Amoah, **Zeinab Mohamed Hassan**, Engelbert Redel, Helmut Baumgart and Yaw Obeng, Analysis of Pristine and TCNQ-Loaded MOF FILMS by Contactless Microwave Dielectric Spectroscopy Technique, **under publication**.

## **Conferences: -**

- 1- The AiMES 2018 Meeting in Cancun, Mexico, Seebeck Coefficient measurements of pristine and TCNQ loaded HKUST-1 SURMOF thin films, Zeinab M. Hassan, Xin Chen, Kai Zhang, Engelbert Redel, Helmut Baumgart (poster).

## ACKNOWLEDGEMENTS

First of all, I would like to thank my supervisor, Prof. Dr. Christof Wöll, for giving me the opportunity to work in IFG and supervising my thesis. Thanks a lot.

Also, I would like to thank prof. Dr. Stefan Bräse for accepting to be the co-referee of my thesis and appreciate the time he contributed to reviewing my thesis. Moreover, I would like to thank Dr. Hartmut Gliemann and Dr. Peter Weidler for offering me their help during my study in IFG. I would like to thank Dr. Manuel Tsotsalas, Dr. Ritesh Halder, Dr. Engelbert Redel, and Dr. Frank Biedermann for their help during my Ph.D. study.

I would like to thank Dr. Peter Weidler, Stefan Heissler, Prof. Dr. Zhengbang wang, and Shahimerdan Abbas for offering me characterization methods the training.

Additionally, I would like to thank Dr. Alexander Welle, Dr. Alexei Nefedov, and Dr. Raheleh Azmi for their help in measuring my samples and discussing the results.

I would like to thank my colleagues in IFG who helped me in my experiments.

Extra special thanks to Dr. Walid Sharmoukh for his help and support in addition to encouraging me the whole time. Dr. Walid your guidance throughout my research helped me to define my direction and interest in my life.

Importantly, I would like to thank my friends and colleagues at my home university, Fayoum University, for supporting, encouraging, and listening to me when I needed someone to listen.

Last but not least, I am grateful to the Ministry of Higher Education of the Arab Republic of Egypt “MoHE” for financing my Ph.D. research at KIT.

Finally, I would like to express my deep gratitude to my family, especially to my mother, my brothers, and my sister for giving me lots of love and support all the time.

